DESIGN OF A SMART GRID COMPATIBLE, BIDIRECTIONAL MODULAR BATTERY CHARGER FOR PLUG-IN ELECTRIC VEHICLES

ELEKTRİKLİ ARAÇLAR İÇİN AKILLI ŞEBEKE İLE UYUMLU, ÇİFT-YÖNLÜ ÇALIŞABİLEN, MODÜLER BİR ŞARJ ÜNİTESİ TASARIMI

FAİK ELVAN

PROF. DR. UĞUR BAYSAL
Supervisor

Submitted to Graduate School of Science and Engineering of Hacettepe University as a Partial Fulfillment to the Requirements for the Award of Master of Science in Electrical and Electronics Engineering

2017

This work named **"Design of a Smart Grid Compatible, Bidirectional Modular Battery Charger for Plug-in Electric Vehicles"** by **FAİK ELVAN** has been approved as a thesis for the Degree of **MASTER OF SCIENCE IN ELECTRICAL and ELECTRONICS ENGINEERING** by the below mentioned Examining Committee Members.

Prof. Dr. Timur AYDEMİR
Head

Prof. Dr. Uğur BAYSAL
Supervisor

Prof. Dr. Işık ÇADIRCI
Member

Assoc. Prof. Dr. Umut SEZEN
Member

Assist. Prof. Dr. Yakup ÖZKAZANÇ
Member

This thesis has been approved as a thesis for the Degree of **MASTER OF SCIENCE IN ELECTRICAL and ELECTRONICS ENGINEERING** by Board of Directors of the Institute for Graduate School of Science and Engineering.

Prof. Dr. Menemşe GÜMÜŞDERELİOĞLU
Director of the Institute of
Graduate School of Science and Engineering

YAYINLAMA VE FİKRİ MÜLKİYET HAKLARI BEYANI

Enstitü tarafından onaylanan lisansüstü tezimin/raporumun tamamını veya herhangi bir kısmını, basılı (kağıt) ve elektronik formatta arşivleme ve aşağıda verilen koşullarla kullanıma açma iznini Hacettepe üniversitesine verdiğimi bildiririm. Bu izinle Üniversiteye verilen kullanım hakları dışındaki tüm fikri mülkiyet haklarım bende kalacak, tezimin tamamının ya da bir bölümünün gelecekteki çalışmalarda (makale, kitap, lisans ve patent vb.) kullanım hakları bana ait olacaktır.

Tezin kendi orijinal çalışmam olduğunu, başkalarının haklarını ihlal etmediğimi ve tezimin tek yetkili sahibi olduğumu beyan ve taahhüt ederim. Tezimde yer alan telif hakkı bulunan ve sahiplerinden yazılı izin alınarak kullanması zorunlu metinlerin yazılı izin alarak kullandığımı ve istenildiğinde suretlerini Üniversiteye teslim etmeyi taahhüt ederim.

☐ **Tezimin/Raporumun tamamı dünya çapında erişime açılabilir ve bir kısmı veya tamamının fotokopisi alınabilir.**
(Bu seçenekle teziniz arama motorlarında indekslenebilecek, daha sonra tezinizin erişim statüsünün değiştirilmesini talep etseniz ve kütüphane bu talebinizi yerine getirse bile, tezinin arama motorlarının önbelleklerinde kalmaya devam edebilecektir.)

☑ **Tezimin/Raporumun** 11/07/2018 **tarihine kadar erişime açılmasını ve fotokopi alınmasını (İç Kapak, Özet, İçindekiler ve Kaynakça hariç) istemiyorum.**
(Bu sürenin sonunda uzatma için başvuruda bulunmadığım taktirde, tezimin/raporumun tamamı her yerden erişime açılabilir, kaynak gösterilmek şartıyla bir kısmı ve ya tamamının fotokopisi alınabilir)

☐ **Tezimin/Raporumun ..... tarihine kadar erişime açılmasını istemiyorum, ancak kaynak gösterilmek şartıyla bir kısmı veya tamamının fotokopisinin alınmasını onaylıyorum.**

☐ **Serbest Seçenek/Yazarın Seçimi**

11 / 07 / 2017

(İmza)

Öğrencinin Adı Soyadı

Faik Elvan

To Deniz, Toprak and Seçil…

ETHICS

In this thesis study prepared in accordance with the spelling rules of Institute of Graduate Studies in Science of Hacettepe University,

I declare that,

- all the information and documents have been obtained in the base of academic rules
- all audio-visual and written information and results have been prepared according to the rules of scientific ethics
- in case of using others' works, related studies have been cited in accordance with the scientific standards
- all cited studies have been fully referenced
- I did not do any distortion in the data set
- and any part of this thesis has not been presented as another thesis study at this or any other university.

11/07/2017

Faik ELVAN

ABSTRACT

DESIGN OF A SMART GRID COMPATIBLE, BIDIRECTIONAL MODULAR BATTERY CHARGER FOR PLUG-IN ELECTRIC VEHICLES

Faik ELVAN

Master of Science, Department of Electrical Electronics Engineering

Supervisor: Prof. Dr. Uğur BAYSAL

June 2017, 95 pages

Wide electrification of the vehicles puts the electric vehicle and grid interaction to a crucial point in terms of research and development for both academics and industry. Moreover, electric vehicles can act as distributed energy sources for the smart grid when necessary. This flexibility makes the electric vehicles an important player among its internal combustion engine counterparts. However, since electric vehicles store and use significant amount of power, their impacts on the utility grid should be well researched and studied to make a smoother transition from classical fuel burning vehicles to electric vehicles. Any efficiency improvement that will be gained in the charging or discharging of electric vehicles' batteries will have profound impact in the long term.

This thesis proposes a bidirectional modular battery charger design that will utilize an optimization control algorithm to determine the operating points of the individual modules in the system to achieve efficiency increase especially at light to middle loads. As power electronic basis for the modules, an isolated single-stage bidirectional topology is selected, analyzed and simulated in the computer medium. An isolated topology is more advantageous in terms of safety that is of the utmost importance for a vehicle. Modular design and optimization algorithm are also verified through computer simulations. Then, two hardware prototype modules are designed and built for 220 V grid voltage; however, tests are

conducted at 120 V grid voltage so as not to put the limited number of modules at risk. Experimental study for the modular operation of the two modules is conducted and efficiency improvement compared to conventional modular design is shown in both G2V and V2G modes.

Keywords: electric vehicle, V2G, G2V, optimization, bidirectional, modular design, charging, smart grid.

ÖZET

ELEKTRİKLİ ARAÇLAR İÇİN AKILLI ŞEBEKE İLE UYUMLU, ÇİFT-YÖNLÜ ÇALIŞABİLEN, MODÜLER BİR ŞARJ ÜNİTESİ TASARIMI

Faik ELVAN

Yüksek Lisans, Elektrik Elektronik Mühendisliği Bölümü

Danışman: Prof. Dr. Uğur BAYSAL

Haziran 2017, 95 sayfa

Şebekeye bağlanabilen elektrikli araçların (EA) son yıllarda yaygınlaştığı ve içten yanmalı motorlu araçlara uygun bir alternatif olabileceği görülmüştür. Ayrıca EA'ların enerji depolama unitelerinin de akıllı şebeke uygulamalarında kullanılabileceği öngörülmektedir. EA'ların şebeke ile uygun bir şekilde entegre edilmesi bu araçların yaygınlaşması için çok önemlidir. Araç şarj üniteleri (AŞÜ) ise bu entegrasyonda büyük bir rol oynamaktadır. AŞÜ'lerin verimlilik, hacim ve ağırlık gibi özellikleri de EA'ların üretim ve işletim maliyetleri üzerinde etkili olacaktır. AŞÜ'ler temelde elektriksel güç dönüşümü yapan cihazlardır. Güç dönüşümü yapan cihazların özelliklerinden birisi de genellikle düşük yüklerde verimliliklerinin düşmesi ve tepe verimliliklerine de tam yüke yakın yerlerde ulaşmalarıdır.

Bu tez kapsamında özgün eniyileme yöntemiyle, özellikle düşük yük seviyelerinden tam yüke kadar yüksek verimlilikte çalışan çift-yönlü modüler bir araç şarj ünitesi tasarımı ve uygulaması yapılmıştır. Belirli bir ortalama güç seviyesi ve bu seviyeye uygun, iki yönlü ve tek aşamada güç çevrimi yapabilen izole bir topoloji seçilmiştir. Tasarımda kullanılan modüllerin tek tek ve birlikte çalışmaları bilgisayar ortamında benzetimler aracılığıyla doğrulanmıştır. ayrıca iki adet modül paralel çalıştırılarak düşük yükten tam yüke kadar mümkün olan en iyi verimde çalışmaları için geliştirilen akıllı akım paylaşım algoritmasının çalışırlığı doğrulanmıştır. Daha sonra, iki adet deneysel prototip 220 V şebeke voltajı için

tasarlanmış, inşa edilmiş, fakat testler inşa edilen sınırlı sayıdaki modülü riske atmamak adına 120 V şebeke voltajında gerçekleştirilmiştir. İki modülün paralel kipte, geliştirilen eniyileme algoritmasını kullanarak çalıştırılmasıyla geleneksel modüler tasarımlara göre elde edilen verim artışı gösterilmiştir.

Anahtar Kelimeler: elektrikli araçlar, eniyileme, akıllı akım paylaşımı, modüler tasarım, araç şarj ünitesi, akıllı şebeke.

ACKNOWLEDGMENTS

This thesis would not have been possible without the guidance and help of several people who in one way or another contributed to the completion of this study. I would like to take this opportunity to thank all those people.

First, I would like to express my appreciation and thanks to my supervisor Prof. Dr. Uğur Baysal for his guidance, patience and his valuable ideas throughout my thesis writing.

I owe a lot to my supervisor at work, Dr. Recep Görür for his much appreciated help, his brilliant ideas and his everlasting patience to guide me in the domain of electronics and particularly during the design and testing phase of this work. I also thank my employer, ELSİS AŞ, for supporting this work by providing me a place to carry out my experiments and allowing me to use company resources.

Finally, I am who I am today thanks to the love of my life, my companion, my wife Seçil Öztoprakçı Elvan. I could not accomplish half the things I have today without you. Our family is now enriched by our twin boys, Deniz and Toprak Elvan and you will have much harder time dealing with us. However, I believe I can speak on behalf of them when I am saying this, we will always love you and try to make you happy for the rest of your life. We need your strength, your wisdom, your patience and your guidance in our life.

TABLE OF CONTENTS

ABSTRACT i

ÖZET iii

ACKNOWLEDGMENTS v

TABLE OF CONTENTS vi

LIST OF TABLES ix

LIST OF FIGURES x

ACRONYMS xiv

1. INTRODUCTION 1

1.1 History of EVs and Definitions 1

1.2 Battery Technologies Used in Vehicular Applications 2

1.3 Charging of Batteries 3

1.3.1 Definitions 3

1.3.2 State of Charge Determination Methods 4

1.3.3 Charging Profiles and Their Effects on Li-ion Batteries 5

1.3.4 Battery Management Systems and Battery Chargers 7

1.4 Impacts of EV Charging on Utility Grid and V2G Operation 9

1.5 Proposed Study 13

2. LITERATURE SURVEY 17

2.1 Double Stage Topologies 17

2.1.1 Power Factor Corrector Topologies 18

2.1.2 DC/DC Converters 20

2.2 Single-Stage Topologies 21

2.3 Modular Electrical Applications 22

3. SYSTEM DESIGN 24

3.1 Modular System Design 24

3.2 Optimization 26
3.2.1 Statement of the Optimization Problem 27
3.2.2 Solution Methods of the Optimization Problem 29
3.3 Power Electronic Basis of the System 31
3.3.1 Selection of Converter Topology 31
3.3.2 Mathematical Analysis of the Topology 32
3.3.2.1 Modulation Scheme 33
3.3.2.2 Current and Power Transfer Relationships 37
3.3.2.3 Soft Switching for DC Side Switches 39
4. SIMULATION RESULTS 42
4.1 Single Module Conceptual Simulation 42
4.1.1 Open Loop Simulation 42
4.1.2 Closed Loop Simulation 44
4.2 Modular System Simulation 46
4.2.1 Simulation Setup and Optimization Algorithm 46
4.2.2 Optimized Sharing Simulation Results 50
5. HARDWARE DESIGN AND EXPERIMENTAL RESULTS 54
5.1 Specifications of the Hardware Prototype 54
5.2 Implementation of Hardware Prototype 55
5.2.1 Magnetic Elements 55
5.2.2 Digital Controller Unit 59
5.2.3 Auxiliary Supplies 62
5.2.4 Semiconductor Switches 63
5.2.5 Battery Pack 65
5.2.6 Final Configuration 65
5.3 Experimental Results 67

5.3.1 Results of the Steady-State Operation of Chargers 67
5.3.2 Experimental Results for the Optimized Sharing 71
6. CONCLUSION and DISCUSSION 78
REFERENCES 82
APPENDICES 87
APPENDIX - 1: FUTURE WORK 87
CURRICULUM VITAE 94

LIST OF TABLES

Table 1.1. Current battery technologies [8] 3

Table 1.2. Charging power levels [21] 9

Table 2.1. Classification of battery charger topologies 17

Table 4.1. Parameters for open loop simulation 42

Table 4.2. Simulation scenarios 43

Table 4.3. Modular system simulation references 50

Table 5.1. Specifications of hardware prototype 55

Table 5.2. Specifications of digital controller unit 60

Table 5.3. Specifications of the first selected MOSFET 64

Table 5.4. Specifications of the second MOSFET 64

Table 5.5. Specifications of the MOSFET used in DC side of Module 2 65

Table 5.6. Specifications of the battery pack 65

Table 5.7. Results of the Module 1in G2V and V2G modes 69

Table 5.8. Results of the Module 2 in G2V and V2G modes 69

Table 5.9. Experiment scenarios 75

Table 6.1. Modular system simulation references 90

LIST OF FIGURES

Figure 1.1. CC-CV charging profile for $LiCoO_2$ [9] 6

Figure 1.2. Li-ion battery simplified AC impedance model [13] 6

Figure 1.3. Hourly electrical energy usage of Turkey for 2nd and 3rd weeks of 2016 [28].. 11

Figure 1.4. Hourly electrical energy usage of Turkey for 2nd and 3rd weeks of 2017 [28].. 11

Figure 1.5. Increase in electrical energy consumption of Turkey from 2016 to 2017 12

Figure 1.6. Effect of uncoordinated charging of PEVs to the grid load [30] 13

Figure 1.7. PEV share in global vehicle sales from 2010 and 10-year projection 14

Figure 1.8. Number of vehicles in use in Turkey from 2010 and 10-year projection 14

Figure 1.9. Estimated number of PEVs that would be in use in Turkey between years 2010-2026 if the world averages could have been achieved 15

Figure 1.10. Number of EVs for the last 5 years and 10-year forecast in Turkey..... 15

Figure 2.1. Block diagram of double stage topologies 18

Figure 2.2. Conventional Boost PFC 18

Figure 2.3. Interleaved Boost PFC 19

Figure 2.4. Efficiency comparison of unidirectional PFC topologies [45] 19

Figure 2.5. CLLC resonant bidirectional DC/DC converter [55] 21

Figure 2.6. Single-phase single-stage DAB AC/DC converter [27] 22

Figure 3.1. Modular system configuration with separate master controller 25

Figure 3.2. Modular system configuration with one module as master controller 25

Figure 3.3. Single/Three-phase configuration of modular system 26

Figure 3.4. Single-phase single-stage DAB AC/DC converter with a separate synchronous rectifier 32

Figure 3.5. Modulation scheme for one switching cycle [27] 34

Figure 3.6. Gate Signals of HF switches 36

Figure 3.7. Gate signals for Zero Voltage Switching 40

Figure 3.8. DC side MOSFETs' switching instants. (a) $t=t_1$. (b) $t=t_2$. (c) $t=t_3$. (d) $t=t_4$..... 41

Figure 4.1. Simulation setup 42
Figure 4.2. Open loop simulation result for case 1, δ=0.25. 43
Figure 4.3. Open loop simulation result for case 2, δ=-0.25. 43
Figure 4.4. Controller for charging operation 44
Figure 4.5. Controller for V2G operation 44
Figure 4.6. Closed-loop system controller. 45
Figure 4.7. Closed-loop simulation reference signals. 45
Figure 4.8. System closed-loop response to reference signals. 46
Figure 4.9. Modular system simulation setup 47
Figure 4.10. Charging current vs efficiency curves of simulation models 47
Figure 4.11. Grid power vs efficiency curves of simulation models 48
Figure 4.12. Surface plot representing the overall efficiency in G2V mode 48
Figure 4.13. Flowchart of optimization algorithm 49
Figure 4.14. G2V mode optimized current sharing 51
Figure 4.15. Efficiency comparison of equal and optimized current sharing methods in G2V mode 52
Figure 4.16. V2G mode optimized current sharing 52
Figure 4.17. Efficiency comparison of equal and optimized current sharing methods in V2G mode 53
Figure 5.1. Block diagram of the hardware prototype 54
Figure 5.2. DC side C-L-C filter 56
Figure 5.3. Winding scheme of the isolation transformer 58
Figure 5.4. Constructed isolation transformer 58
Figure 5.5. Leakage inductor 59
Figure 5.6. Digital controller unit 60
Figure 5.7. EPWM scheme utilized in the DCU 62
Figure 5.8 First hardware prototype 66

Figure 5.9. Modular system with two individual modules 66
Figure 5.10. Experimental setup 67
Figure 5.11. Voltage and current waveforms of a working hardware prototype in G2V mode 68
Figure 5.12. Voltage and current waveforms of a working hardware prototype in V2G mode 68
Figure 5.13. Harmonic spectrum of grid current of Module 1 in G2V Mode 70
Figure 5.14. Harmonic spectrum of grid current of Module 1 in V2G Mode 70
Figure 5.15. Harmonic spectrum of grid current of Module 2 in G2V Mode 71
Figure 5.16. Harmonic spectrum of grid current of Module 2 in V2G Mode 71
Figure 5.17. Closed loop controller block diagram of the built system 73
Figure 5.18. Charge current vs efficiency curves of the modules in G2V mode 73
Figure 5.19. Grid power vs efficiency curves of the modules in V2G mode 74
Figure 5.20. Surface function of the modular hardware system in G2V mode 74
Figure 5.21. Surface function of the modular hardware system in V2G mode 75
Figure 5.22. Comparison of equal sharing and optimized sharing in G2V mode 76
Figure 5.23.Comparison of equal sharing and optimized sharing in V2G mode 77
Figure 6.1. Modular system simulation setup 87
Figure 6.2. Charging current vs efficiency curves of simulation models 88
Figure 6.3. Grid power vs efficiency curves of simulation models 88
Figure 6.4. Flowchart of optimization algorithm 89
Figure 6.5. G2V mode optimized current sharing 91
Figure 6.6. Efficiency comparison of equal and optimized current sharing methods in G2V mode 91
Figure 6.7. V2G mode optimized current sharing 92
Figure 6.8. Efficiency comparison of equal and optimized current sharing methods in V2G mode 92

Figure 6.9. Three-phase equal current sharing G2V mode results 93

Figure 6.10. Grid power waveform when system is in three-phase V2G mode..... 93

ACRONYMS

Acronyms

ABC	Artificial Bee Colony
AC	Alternating Current
ADC	Analog-to-Digital Converter
BEV	Battery Electric Vehicle
BMS	Battery Management System
CC-CV	Constant Current – Constant Voltage
CPU	Central Processing Unit
DAB	Dual Active Bridge
DC	Direct Current
DCU	Digital Controller Unit
EMI	Electromagnetic Interference
EPWM	Enhanced Pulse Width Modulation
ESR	Equivalent Series Resistance
EV	Electric Vehicle
EVSE	Electric Vehicle Supply Equipment
G2V	Grid to Vehicle
GPIO	General Purpose Input/Output
HEV	Hybrid Electric Vehicle
HF	High Frequency
ICEV	Internal Combustion Engine Vehicle
IGBT	Insulated Gate Bipolar Transistor
LCD	Liquid Crystal Display
MCU	Microcontroller Unit
MOSFET	Metal Oxide Semiconductor Field Effect Transistor
PCB	Printed Circuit Board
PFC	Power Factor Correction
PHEV	Plug-in Hybrid Electric Vehicle
PSFB	Phase Shifted Full Bridge
PSO	Particle Swarm Optimization
PV	Photovoltaic
PWM	Pulse Width Modulation

SoC	State of Charge
THD	Total Harmonic Distortion
V2G	Vehicle to Grid
V2H	Vehicle to Home

1. INTRODUCTION

This section will give information on the history of the use of electrical energy in vehicles, battery technologies and charging methods.

1.1 History of EVs and Definitions

During the first years of vehicle technology, internal combustion engine vehicles (ICEV) were not as common as they are today. Electric vehicles (EV) were the main means of private transportation with 40% of the total newly sold 4200 vehicles in US in 1900s [1]. However, development of internal combustion engine and the vast availability of gas compared to the electrical energy made the ICEVs a more promising candidate for transportation. Hence, EVs started to disappear from the market and ICEVs took place instead of them. In 1970s, EVs started to emerge as an alternative approach for transportation once again due to the concerns regarding petroleum based fuel consumption. For instance, gas and diesel are limited sources in the long term and cause environmental pollution. On the other hand, EVs have the main advantages of being environmental friendly, having sustainable energy via renewable sources and being able to operate with significant noise and maintenance reduction compared to ICEVs.

Electric vehicles can be categorized mainly in three: hybrid electric vehicles (HEVs), plug-in hybrid electric vehicles (PHEVs) and battery electric vehicles (BEVs). Throughout this document PHEVs and BEVs will be grouped under a common name where applicable, which is plug-in electric vehicles (PEV). HEVs have an electric motor coupled mechanically to the vehicle and a small battery to supply power for this motor. Their battery capacity is relatively small and they have no means of charging their battery from outside. Their electric motor is designed to assist a main operating internal combustion engine. PHEVs are different from HEVs in the sense that they have a bigger battery pack and are able to connect to external power sources to charge their batteries. Other than that, their operation is identical to that of HEVs. BEVs are powered by only electrical energy and as a result they need to charge their batteries from outside sources to replenish their energy. Capacity of their battery pack is considerably bigger than that of PHEVs. Their drivetrain is composed of electric motor(s), drive inverter(s), mechanical coupler and optional transmission gears.

Although internal combustion engine technology is advanced and millions of automobiles are manufactured and sold each year, EV technology started to draw serious attention in recent years. Major automobile manufacturers have been selling HEVs since the early 2000s

and they started to add PHEVs and BEVs to their existing products. One of the major barriers that is hindering widespread adaptation of BEVs is the range anxiety. Range anxiety means the fear of using up all electrical energy in the vehicle before reaching the destination [2]. This is also true for ICEVs, but BEVs do not have fast charging network as wide as gas stations and charging a BEV takes comparably longer time than filling up a gas tank. Manufacturers and researchers are trying to address this problem by improving energy storage technologies, trying to find efficient and safe way to swap batteries in BEVs, or providing a wider fast charging network. A major all electric automobile manufacturer recently started building the world's biggest Li-ion battery manufacturing plant that will double the battery manufacturing capacity of the world. Researchers from all over the world are trying to find better chemical methods and materials to increase energy and power density of the batteries.

1.2 Battery Technologies Used in Vehicular Applications

There are several chemical ways of storing electrical energy and the most common ones used in vehicular applications are lead-acid, Ni-MH and Li-ion. Fuel cells can also be used in EVs as an energy storage unit, but they cannot be charged using battery chargers, thus they are not in the scope of this study. Use of lead-acid batteries in electric vehicles dates back to 1881 [3]. However, modern applications of EVs mostly use Ni-MH and Li-ion batteries, latter becoming more and more popular each year with its superior performance factors compared to the others. There are four key performance parameters for batteries: specific energy, specific power, cycle life and calendar life. Specific energy (Wh/kg) is the amount energy stored in one kg of mass. Higher specific energy translates to higher energy capacity with the same weight of batteries. Battery energy sets the limit on the vehicle range; hence higher specific energy leads to increase in the range of the vehicle. Battery power determines the acceleration time and dynamic performance of the vehicle. Thus, specific power (W/kg) plays key role in dynamic response of the vehicle. Cycle life and calendar life are mostly manufacturer dependent properties as each manufacturer uses its own method to determine the cycle life and calendar life. However, these numbers can give an opinion on the useful lifetime of a battery. Cycle life is the number of times that a battery can be discharged to a depleted state and charged back to its full state until its rated capacity drops down to a predetermined threshold. This threshold is in the range of 70% to 80% [4]-[7]; however, there is little to no analysis to support the selection of this threshold [7]. Also, depth of discharge, which is defined as the percentage usage of battery capacity, greatly influences

the cycle life of a battery [5], [6]. As depth of discharge increases, cycle life of a battery decreases. And calendar life is the amount of time a battery can be used until its rated capacity drops down to a predetermined threshold. Again this threshold is in the range of 70% to 80%. Table 1.1 depicts key performance specifications for the three most popular battery technologies. As can be seen from the table, Li-ion batteries have superior characteristics in all four performance parameters and they are also more reliable.

Type	Lead-Acid	Ni-Mh	Li-ion
Specific Energy (Wh/kg)	30~45	60~120	90~160
Specific Power (W/kg)	200~300	150~400	250~450
Cycle Life	400~600	600~1200	1200~2000
Battery Reliability (%)	85.55	77.9	91.69

Table 1.1. Current battery technologies [8]

In addition, lead-acid batteries have the "memory effect" [8] and Ni-MH have high self-discharge rates [9] while Li-ion batteries present neither. Li-ion batteries have their use in various models of PEVs from different manufacturers. Li-ion technology is still young compared to lead-acid and Ni-MH, and researchers are trying to improve the current performance of the Li-ion batteries. Hence, they will be seen in most modern PEV applications in coming years.

1.3 Charging of Batteries

This section will focus on definitions of battery charging terminologies, charging profiles and effects of charging on batteries.

1.3.1 Definitions

Capacity: The capacity of a battery can be shown using two ways; watt-hour (Wh) and ampere-hour (A-h). Watt-hour is a unit of energy equivalent to one Watt of power dissipated or used in one hour. One ampere-hour is a measurement of electric charge that can be discharged from a source at constant one ampere of current in one hour. Watt-hour is more commonly used when referring PEV battery packs. Since, energy requirement is rather high in PEVs, kilowatt-hour (kWh) is preferred unit for energy stored in battery pack.

State of Charge (SoC): State of Charge can be defined as the current capacity of the battery divided by its rated capacity at a given instant. SoC information determines the remaining range of the vehicle which is a critical information for the driver.

Charging Rate: Charging rate is often denoted with C which can be defined as the charging/discharging current in one hour for a given battery. Ampere-hour rating of a battery can be taken as C-rate. For example, 2 A-h battery has a C-rate of 2 A. Fraction or multiples of C can be used to indicate charging or discharging current. When a 2 A-h battery is charged with 0.5 C, it means that charging current is 1 A. Peak current demand from batteries which is an important parameter for acceleration of vehicles, also denoted with using C-rate convention. For instance, $LiCoO_2$ batteries can supply 1 C, $LiFePO_4$ batteries can supply 5 C continuous and 10 C pulsed current, LiNiMnCo batteries can supply 1 C continuous and 5 C pulsed current [10].

1.3.2 State of Charge Determination Methods

State of charge is a critical information and estimation of it accurately and reliably poses an important challenge for the vehicle manufacturers. SoC of a battery can be estimated using various methods. These methods can be categorized as direct measurement, book-keeping estimation, adaptive systems and hybrid methods [11].

Direct measurement methods include voltage estimation and impedance spectroscopy methods. Voltage estimation relies on the change in open circuit battery voltage with different SoC values. Normally batteries exhibit higher open circuit voltage when they are full and it will decrease with decreasing battery capacity. This information can be used to estimate the SoC of a battery at a given instant. However, li-ion batteries exhibit nearly constant open circuit voltage for a wide range of SoC. That is why this method is not reliable to be used with li-ion batteries. The impedance spectroscopy method measures battery impedances over a wide range of ac frequencies at different charge and discharge currents. The values of the model impedances are found by least-squares fitting to measured impedance values. SoC may be indirectly inferred by measuring present battery impedances and correlating them with known impedances at various SoC levels [11].

Book-keeping method is also named as Coulomb counting method. A battery has a certain Ah capacity and one can estimate the SoC of a battery by directly counting the Coulombs going in and out of the battery and integrating this over time. This method can reliably be used for li-ion batteries whose charge/discharge efficiency is high and self-discharge rate is low. These effects can also be taken into account to improve the accuracy of the method.

Adaptive systems include newer advanced methods like neural networks and fuzzy logic systems. Neural networks learn the behavior of a battery over time gathering voltage, current

and ambient temperature information and use this to predict the current SoC of a battery. Fuzzy logic method makes use of models to analyze data obtained by impedance spectroscopy and/or Coulomb counting methods [11]. These methods can be improved with further research on the optimization of the data gathering and processing methods and development of more advanced algorithms.

As the name suggests, hybrid methods involve the combination of different methods. As the battery will lose capacity with each charge cycle, its ability to hold charge will also decrease. It is important to take this into consideration while estimating SoC. A method comprised of Coulomb counting and voltage measurement combination is proposed in [12] and it is shown that it improves the accuracy of SoC estimation in the long term as it takes the aging into consideration during estimation.

It can be concluded that adaptive and hybrid systems show promise in further increasing the accuracy and reliability of SoC estimation. Adaptive methods are inherently good in their ability to be applied for different types of batteries and ambient conditions. Also different types of combinations for hybrid systems bring the best of different methods to create a much advanced method.

1.3.3 Charging Profiles and Their Effects on Li-ion Batteries

Battery chargers can employ several methods to charge batteries. This section focuses on charging profiles and their effects on battery life, performance and charging time.

CC-CV Charging: Constant current, constant voltage charging, also known as CC-CV charging, is the most commonly used charging profile for Li-ion and lead-acid batteries. Typical Li-ion cells with LiCoO2 cathode have 4.2V rated voltage and when cell voltage reaches to that level it is accepted as fully charged. Other Li-ion cells with different cathode chemistries may have different charge voltage. CC-CV battery charging has two sections; first, battery is supplied with constant current rate up to charge voltage, then it is charged slowly with constant voltage until charge current drops down to a specified limit. Different cell chemistries show different responses to CC-CV charging. Figure 1.1 shows the CC-CV charging regime for $LiCoO_2$ type Li-ion battery indicating charging current, cell voltage and SoC. Lead-acid battery chargers employ a third section called trickle charge or float charge. This section is necessary to compensate self-discharge of lead batteries that is mentioned before.

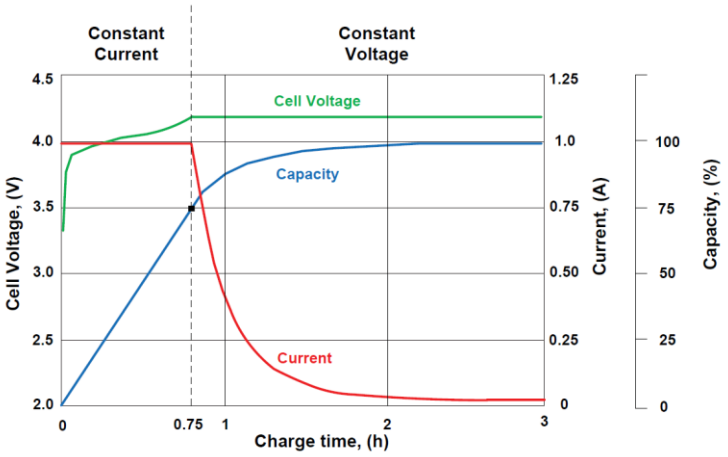

Figure 1.1. CC-CV charging profile for $LiCoO_2$ [9]

Sinusoidal-like DC Charging: Sinusoidal charging refers to the charging current being in sinusoidal shape with a DC offset. It is usually seen in chargers with single stage power conversion topologies[1]. In those topologies, twice of the frequency of input voltage is seen at the output current waveform. The frequency of output current ripple depends on the input voltage and cannot be controlled without changing the input voltage frequency. Studies on advantages and disadvantages of frequency controlled sinusoidal-like DC charging are underway and it is an open research area.

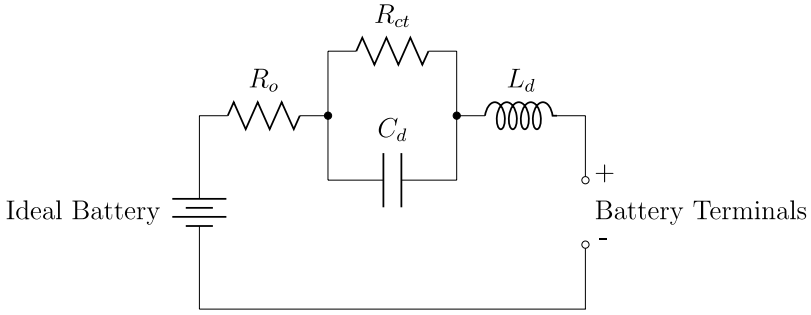

Figure 1.2. Li-ion battery simplified AC impedance model [13]

In [13], effects of sinusoidal-like DC charging on Li-ion batteries were investigated. Simplified AC impedance model of a Li-ion battery is given in Figure 2. Using an AC impedance analyzer, the frequency at which the equivalent impedance is minimum can be found. Then, frequency of the charging current is adjusted to that frequency. Study showed that charging performance of the Li-ion battery increases when it is charged with sinusoidal-like DC current, because minimizing equivalent series impedance reduces the losses and allows the current to flow into battery easily. With this method, charging time can be

[1] Single stage topologies will be explained in detail in further sections.

reduced, charging efficiency can be increased and temperature variation of the battery pack while charging can be reduced. A similar study was also conducted and results are promising [14]. However; in those studies, it is required to have an ac impedance analyzer to determine the optimum frequency and researchers used sample batteries from one manufacturer. Li-ion batteries have many different types of cell chemistries and until the research scope is widened, it would not be practical to assume all Li-ion batteries will react the same. The effects of sinusoidal charging are also investigated for lead-acid batteries [15]. All of these studies show that no significant performance degradation is caused by the ripple in the charging current.

Ripple Effects: In [16], Breucker tried to assess the effects of current ripple on the Li-ion batteries and concluded that current ripple does not have measurable effect on battery resistance, discharge and regen performance of the batteries. In the tests, two battery packs underwent a 3-month current ripple cycle. One battery pack was subjected to high current ripple in the first month, while the other was subjected to low current ripple. In second month, the situation was reversed. And on the third month, both packs were subjected to low current ripple. Battery resistance increased and the general discharge and regen performance of the battery packs decreased during the tests, but this was to be expected with 3-month combined life cycle test which includes several other environmental factors affecting the batteries.

1.3.4 Battery Management Systems and Battery Chargers

Li-ion cells are rather sensitive to certain situations, such as overcharging, over discharging and temperature. Li-ion batteries have different rated open circuit voltages and voltage operating window depending on the cathode chemistries. When the voltage of the battery exceeds its charge voltage, CO_2 forms inside the cell in gas form increasing the pressure inside the battery. If charging continues, battery may blow up with a flame causing safety risk for the user and the environment [17]. Also, when they are discharged below the specified limit, their performance is degraded [16]. Temperature is also a critical element in charging Li-ion batteries. Normally, Li-ion batteries should be charged between temperatures 5°C~45°C. No charging is allowed at subzero temperatures, because metallic plating would occur on the anode and it cannot be removed [18]. Also, at low temperatures internal resistance of the battery increases causing decrease in charging efficiency. To address all aforementioned situations, Li-ion batteries have battery management system (BMS) at the pack level. BMSs have five main functions; thermal management, cell

balancing, monitoring overcharge and over discharge situations to prevent batteries from hazardous effects and loss of performance, calculating SoC of the battery and monitoring the battery pack for internal shorts, loose connections to ensure the safety of battery, device and people [19], [20]. Most modern BMSs have communication busses allowing them to exchange information with in vehicle components, especially the battery charger, and outside components, like electric vehicle supply equipment (EVSE). Using battery information, chargers can optimize their charging algorithms according to the battery.

Battery chargers have significant impact on the reliability and operating life of batteries. Most consumer electronics; cell phones, digital cameras, etc., uses rechargeable batteries and they often come with a dedicated charger with a simple task of charging the battery. It is easy to replace the batteries of small electronics when they malfunction, whereas battery pack is one of the most important and most expensive parts of a BEV and it should be carefully protected. Hence, high quality voltage and current supply, overcurrent and overvoltage protections, and optimized charging algorithm should be among the advanced features that need to be implemented on vehicle battery chargers. For modern Li-ion energy storage systems, battery chargers work together with BMSs to achieve aforementioned tasks.

Battery chargers for BEVs can be categorized in three according to their power levels; Level 1, Level 2 and Level 3. Level 1 charging allows power flow up to 1.9 kW. It can be used in home or office power outlets. However, the time required for full charging can reach to 36 hours for an EV which is impractical for most consumers. Level 2 charging uses 240 Vac single phase or 400 Vac three phase power outlets to charge the vehicle batteries up to ten times faster than Level 1 charging, reaching to 19.2 kW rated power [21]. Level 2 charging provides faster charging process which is more suitable for vehicle owners. Both Level 1 and Level 2 chargers are on-board chargers that are equipped inside the vehicles. Size and weight constraints limits the maximum power available from these type of chargers. Level 3 charging is developed to address this issue and it is an off-board charger that are usually placed on charging stations. Level 3 chargers supply high DC currents directly to the batteries bypassing on-board chargers on vehicles. Their power level can reach to 100 kW and can charge most EVs and PHEVs under an hour [21]. A summary of charging levels and estimated charge times for different types of vehicles can be seen in Table 1.2.

Table 1.2. Charging power levels [21]

Power Levels of Chargers	Charger Location	Expected Power Level	Charging Time	Vehicle Types
Level 1 120 V rms (US) 240 V rms (EU)	On-board 1-phase	1.4 kW 1.9 kW	4-11 hours 11-36 hours	PHEVs (5-15 kWh) EVs (16-50 kWh)
Level 2 240 V rms (US) 400 V rms (EU)	On-board 1- or 3-phase	4 kW 19.2 kW	1-4 hours 1-3 hours	PHEVs (5-15 kWh) EVs (16-50 kWh)
Level 3 208-600 V rms or V DC	Off-board	50 kW 100 kW	0.4-1 hours 0.2-0.5 hours	EVs (16-50 kWh)

EV battery chargers can also be identified based on their functionality; regular chargers, smart chargers and bi-directional smart chargers. Regular chargers are the first EV battery chargers developed and their main goal is to charge the batteries as soon as they are plugged in. Smart chargers are advanced versions of regular battery chargers in the sense that they have a number of features that make them smart. They can communicate with BMSs as stated before, but more importantly they can also communicate with the grid to determine charging time window and charging power so as not to disturb the grid functionality while providing the optimum charging performance for the battery. Users may also want to put the focus on the fastest charging routine and can do so by programming the smart charger. Bidirectional smart chargers are even one step further away than conventional smart chargers. As the name suggests, they can provide two-way power flow between the grid and the vehicle battery pack on top of being smart. In order for bi-directional power flow to be meaningful these chargers have to be smart and have the information of grid status. These battery chargers make vehicle-to-home (V2H) and vehicle-to-grid (V2G) technologies possible. Detailed information on the impacts of the EVs on grid functionality and V2G operation will be given in next section.

1.4 Impacts of EV Charging on Utility Grid and V2G Operation

In order to have a better look at the effects of a PEV on the utility grid, energy consumption comparison can be made between average electricity consumption of a house in Turkey and a PEV. According to the information taken from Turkish Statistical Institute website, number of households in Turkey in 2015 is 21,662,260 [22]. Also from the same website, annual electrical energy consumption of residential buildings can be found as 47,808 GWh [23]. Then, average annual electrical energy consumption of a household in Turkey can be calculated as 2,207 kWh. Energy consumption of a BEV is estimated as 0.16 kWh/km from

the information gathered from three BEVs from their estimated range and battery capacity information. By 2015, the total road motor vehicles in Turkey is 19,994,472 [24] and the vehicles have travelled 113,274,000,000 km on the roads of Turkey in 2015 according to the information taken from Turkish Statistical Institute [25]. This information would put the average annual mileage of a vehicle at 5,663 km. If a BEV is used to cover that much distance, it would require approximately 906 kWh electrical energy from the batteries. As reported in [26], battery charger of a popular PHEV operates at 87% efficiency at half power and at 91.5% efficiency at full power. Also, the charger topology reported in [27] achieves 89.9% peak efficiency. Considering these facts, a conventional battery charger on an electric vehicle can be assumed to operate at 90% average efficiency. Then, an EV would draw 1,006 kWh of energy from the grid annually. This energy is 46% of an annual average electrical energy consumption of a house in Turkey and it would mean that every battery electric vehicle would put a strain on the utility grid about half of a new house would. If charging mostly takes place at home, average electrical energy consumption of that house will increase about 41%. Impacts of probable wide electrification of vehicles on the utility grid should be studied and researched extensively to prevent possible downsides of EVs on the utility grid.

To evaluate the hourly electrical energy usage of Turkey, the data on the electrical energy transmission of Turkey is taken from Turkish Electricity Transmission Company website [28]. Turkey decided not to comply with the world-time standard by rejecting to switch to winter time in October 2016. To consider the effects of the rejection of complying world time standard between October 2016 and March 2017, the hourly electrical energy usage data gathered for January 2016 and January 2017. A two-week span covering 2nd and 3rd weeks of both years are selected to eliminate the effects of New Year's Holiday. Average hourly electrical energy consumption of Turkey from 11.01.2016 and 24.01.2016 is depicted in Figure 1.3 and average hourly electrical energy consumption of Turkey from 09.01.2017 and 22.01.2017 is depicted in Figure 1.4. In 2016 the peak hour is at 18, however this peak is shaved off in 2017 probably due to longer use of sun light with the rejection of complying world time standard.

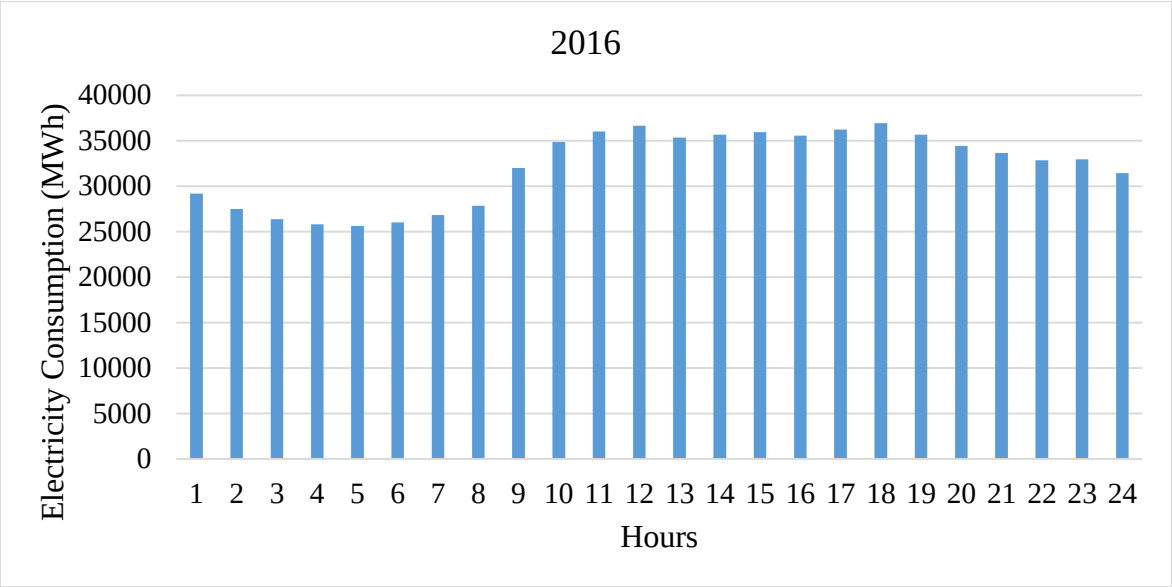

Figure 1.3. Hourly electrical energy usage of Turkey for 2nd and 3rd weeks of 2016 [28]

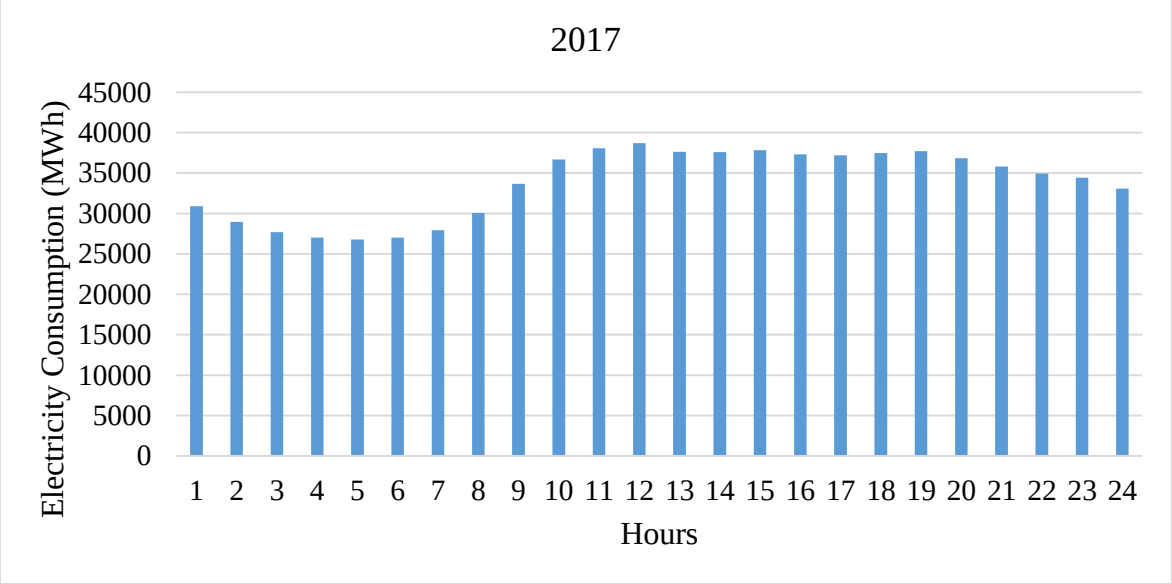

Figure 1.4. Hourly electrical energy usage of Turkey for 2nd and 3rd weeks of 2017 [28]

Although the evening peak is shaved off, the energy usage is increased at 8 hours. This is more vividly depicted in Figure 1.5 which shows the increase in electrical energy consumption between 2016 and 2017. The average increase in electrical energy consumption is calculated as 5.19% for these two weeks. Figure 1.5 shows that at 8 hours in the morning the increase is above average, while it is lower than average at 17 and 18 hours. This can also be attributed to the rejection of complying world time standard.

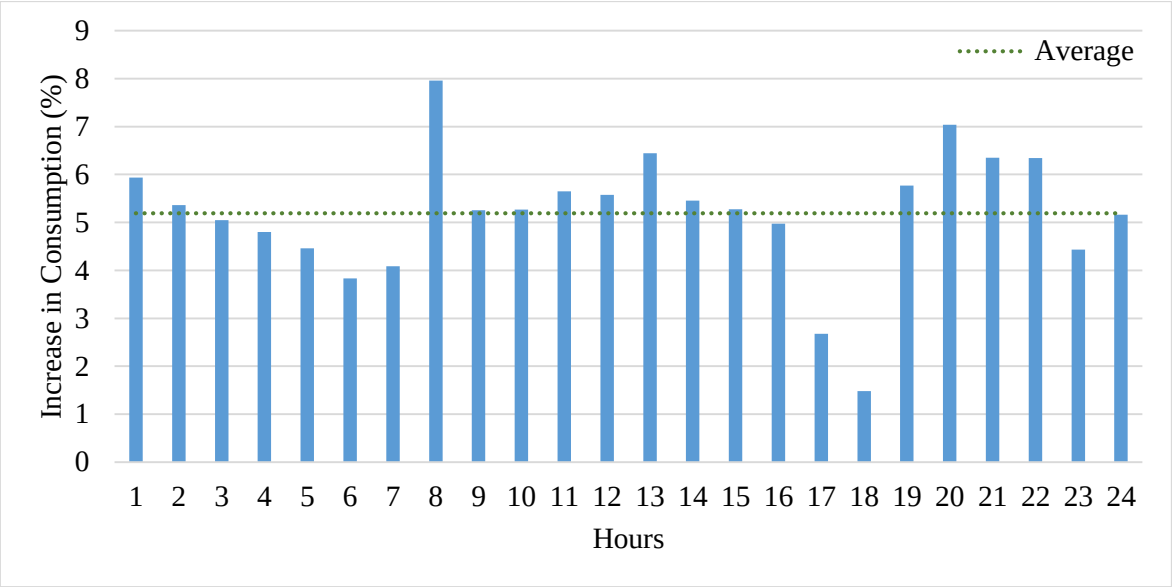

Figure 1.5. Increase in electrical energy consumption of Turkey from 2016 to 2017

Regardless, electrical energy consumption is higher when people are awake and actively working. Utility grid has to be designed to supply the peak power when needed, thus most of the grid capacity is not used in valley hours as can be seen from the hourly electrical energy usage figures of Turkey. Uncoordinated charging of PEVs can dramatically increase the peak load of the grid. In [30], a simulation study on the uncoordinated direct charging of EVs is conducted. Grid model in this study is based on the Danish island of Bornholm and assumes the EV's share in the total number of vehicles is 10%. Also driving behavior of the EVs in the simulation is based on real world data. Figure 1.6 shows the results of uncoordinated charging of PEVs on the utility grid [30]. It is clearly seen that EVs increase the peak loads even more. Also, a simulation study was conducted in Australia and results showed significant increase in transformer loads and voltage unbalance [31].

Considering the negative impacts of uncoordinated EV charging to the utility grid, charging process could be moved to valley hours for better utilization of the electrical grid with the use of smart chargers. With the wide electrification of transportation, a flatter curve for the hourly electrical energy use in a day can be obtained which leads to higher grid utilization. Higher grid utilization reduces grid installation and operation costs. Reduction in operation costs can be increased by giving incentives to PEV owners, creating new tariffs, etc. This way, both parties would benefit from the situation [32].

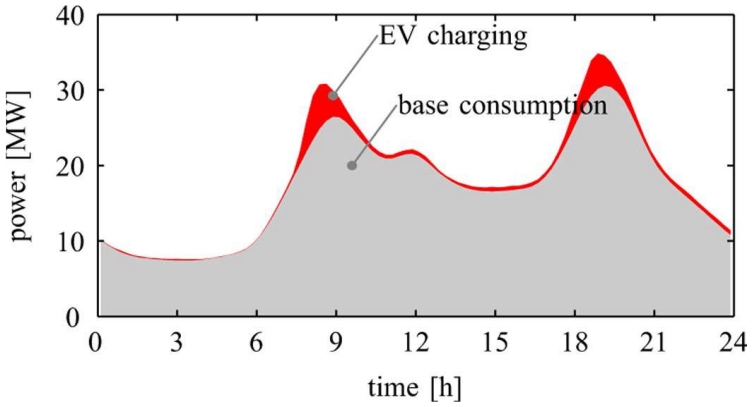

Figure 1.6. Effect of uncoordinated charging of PEVs to the grid load [30]

Taking one step further from controlled charging of PEVs, energy storage capabilities of PEVs can be used to increase the utilization of the grid even to a higher level. With the help of V2G capable bidirectional smart chargers mentioned in previous part, energy stored in PEVs can be supplied to the grid at peak hours to shave the top of the peak load and PEVs can be charged again at valley hours [33], [34]. To use the PEVs as energy storage units and power quality improvement agents have been researched extensively, suitable methods to achieve that have been discussed [35]-[39]. There are yet to be V2G enabled PEVs on the roads, but in [32] it is estimated that V2G adaption could take place in 8 to 10 years.

1.5 Proposed Study

Increasing power conversion efficiency is one of the most important matters in PEV charger design. PEVs store and use significant amount of electrical energy as stated in previous section and power conversion stage is where the most of energy losses take place. Considering future widespread adoption of PEVs, efficiency improvement becomes a prominent issue to be addressed above all. Any efficiency improvement on the power conversion will have a significant cumulative impact on the energy used by PEVs and reduce the possible negative effects of large scale adoption of PEVs on the utility grid.

In order to quantify the importance of a small efficiency improvement in efficiency, a forecast on the energy savings for the electric vehicles in Turkey can be considered. However, unfortunately Turkey lags behind the world's averages concerning the electrification of vehicles. This is apparent from the PEV share in the global vehicle sales from 2010 [64] and number of EVs sold in Turkey [40]. Figure 1.7 illustrates the statistics of PEV share in global vehicle sales and 10-year projection. Figure 1.8 depicts statistics on number of vehicles in use from 2010 and 10-year projection based on the data taken from Turkish Statistical Institute [24]. If Turkey had been able to keep up with the world averages on the PEV sales the number of PEVs on the road would have been much higher. This is

also illustrated in Figure 1.9. As can be seen from the projection curve, the number of PEVs on the road reaches to almost 500,000 by 2026. This number is projected to be 2,079 considering the "current" number of EVs sold in Turkey as it is depicted in Figure 1.10. Unless some drastic measure is taken, Turkey will definitely fall behind of the world on the electrification of vehicles in the future. To see the big picture, the energy savings of the next 10 years to be gained from 2% increase in charging efficiency of electric vehicles can be calculated with the assumption that the world averages is met in Turkey. When this calculation is carried out, the result comes out to be 36,356 MWh, and that is equivalent to the annual electrical energy consumption of 16,473 houses in Turkey.

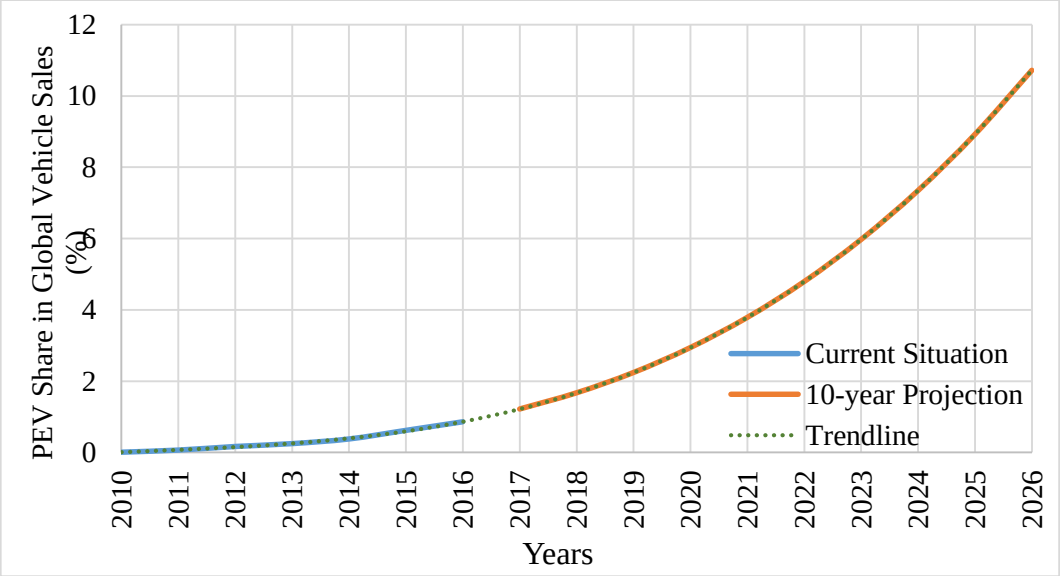

Figure 1.7. PEV share in global vehicle sales from 2010 and 10-year projection

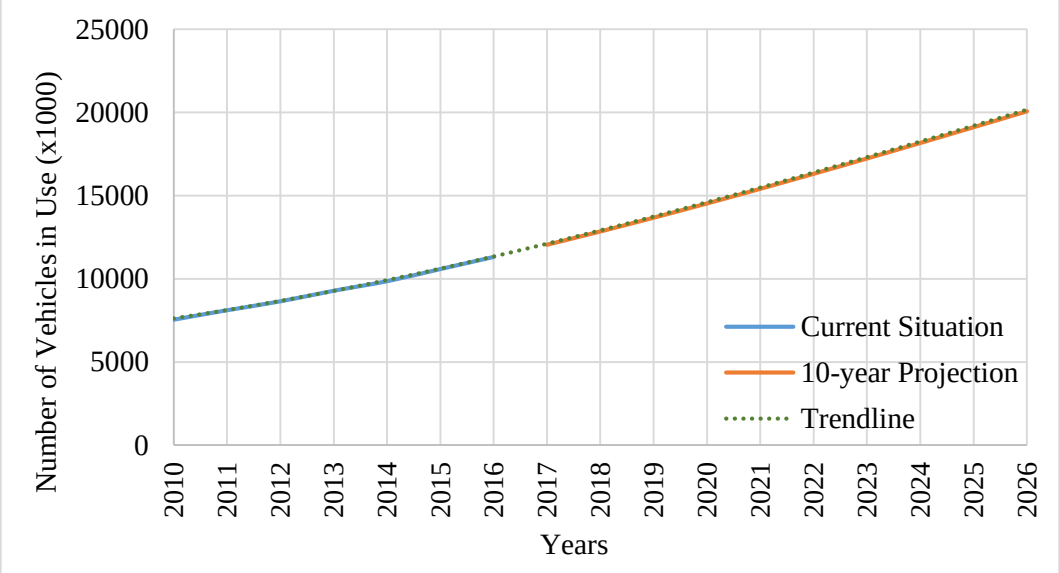

Figure 1.8. Number of vehicles in use in Turkey from 2010 and 10-year projection

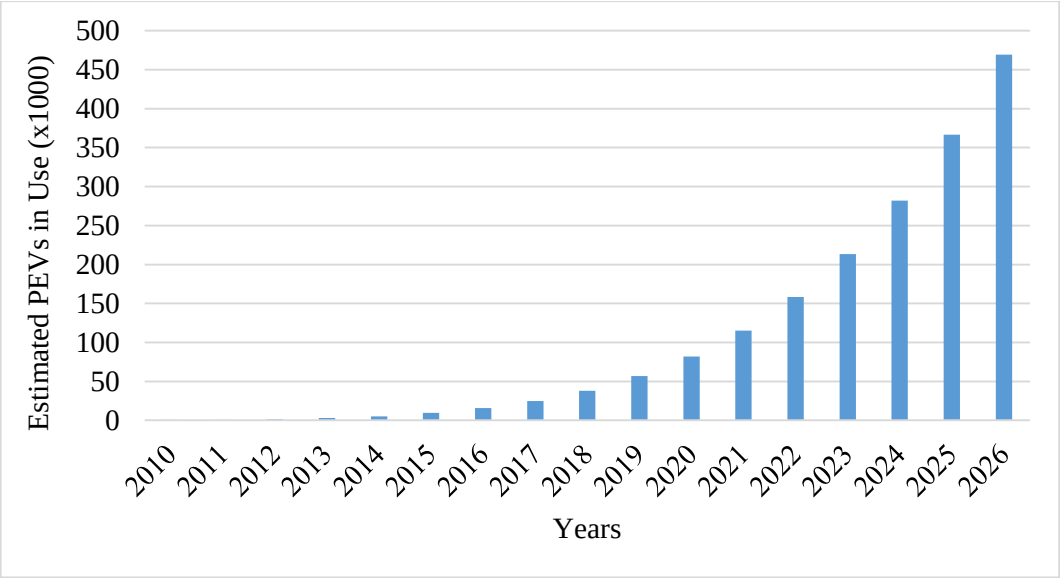

Figure 1.9. Estimated number of PEVs that would be in use in Turkey between years 2010-2026 if the world averages could have been achieved

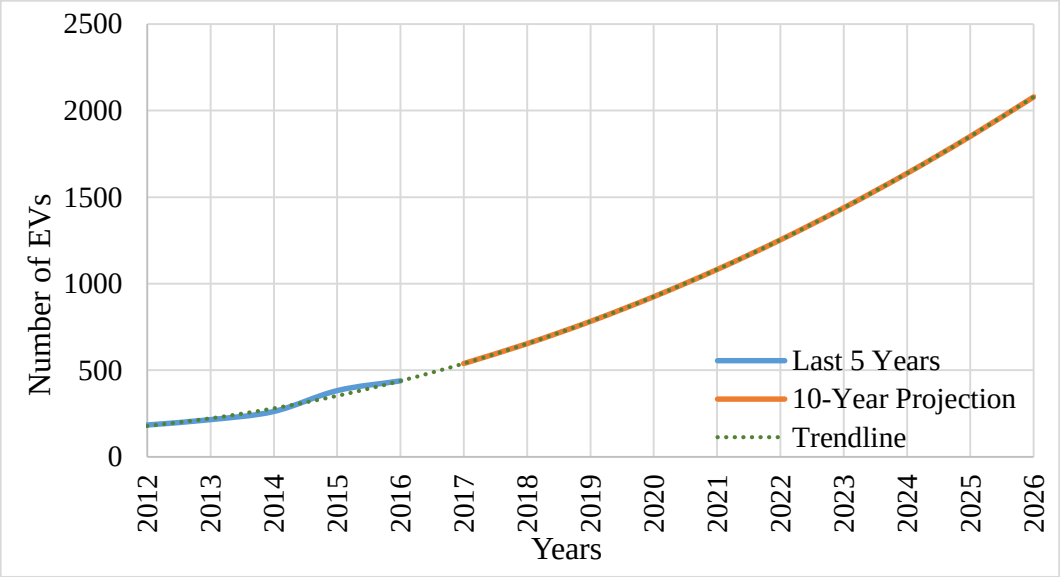

Figure 1.10. Number of EVs for the last 5 years and 10-year forecast in Turkey

This calculation signifies the importance of efficiency improvement in the long term. If the increase in the electrification of vehicles takes place at a more aggressive pace than predicted in Figure 1.7, the energy savings will be even greater. Also considering the V2G technologies that is expected to deploy in the next ten years, studies on the newer charger units that are to be employed in electric vehicles are essential to keep with the current trends in transportation technologies.

This study proposes a new modular, bidirectional smart charger design to be used in EV and PHEV applications. In the scope of this study, bidirectional EV charger modules are designed and tested, and a modular charger system are developed. One of the most important

aspects of the system design is the optimization control algorithm for modular charger system. Most power electronic system exhibits lower efficiency in light to middle load conditions. In this study, an optimization control algorithm is designed and this algorithm determines the operating points of the individual charger modules based on the load/efficiency data of the modules in order to keep the overall efficiency of the charger system high at all charging powers. Moreover, optimization approach can be extended to other power electronic systems in the future. This study contributes to the literature by proposing a new design and control method to decrease the power losses in EV charger systems. Moreover, at light loads harmonic distortion on the grid input current is high and power factor is low in general application of power electronic converters. Modular approach also keeps the total harmonic distortion low and power factor high from light loads to full load to improve power quality of the battery chargers. Another aspect of the design is bidirectional operation which enables the use of V2G technologies to better adapt to the technologies of the future considering the increasing penetration rate of EVs.

This thesis is formed as follows. In Section 2, a literature survey on the existing power electronic converter topologies utilized mainly in EVs, emerging single-stage topologies and the modular applications are shared. Section 3 is focused on the modular system design, statement of the optimization problem and possible solution methods and the detailed mathematical analysis of the selected power conversion topology that is utilized in the hardware implementation. Section 4 presents the detailed results of the simulation studies in both single module operation and the modular operation. The block diagram of the optimization algorithm is also given in this section. In Section 5 detailed information and the necessary calculations on the design of the hardware modules and the concrete experimental results verifying the operation of the charger modules in parallel configuration are given. Section 6 presents conclusions and contributions of the study and discusses the possible impacts that it might carry in the long term. Last section presents preliminary future work on the subject.

2. LITERATURE SURVEY

With today's power electronics technology, it is possible to design and manufacture smart battery chargers that are smart grid compatible and capable of unidirectional or bidirectional power flow. Battery charger topologies can be categorized according to their safety features, direction of power flow and number of stages of power conversion. This categorization is depicted in Table 2.1. In this classification, the term "safety features" is selected because isolated chargers add an extra level of security that non-isolated ones do not have. Power conversion stages refer to the number of stages that is employed to convert the electrical energy to suitable form to charge the batteries. Power flow was explained in section 1.4.

Table 2.1. Classification of battery charger topologies

Safety Features	**Power Flow**	**Power Conversion Stages**
Isolated	Unidirectional	Single Stage
Non-isolated	Bidirectional	Double Stage

A battery charger can be identified in topological aspect using a combination of these three categories. In subsequent chapters the point of approach will be around power conversion stages. Also, this study will focus on bidirectional topologies, so details on unidirectional topologies will be kept at minimum.

2.1 Double Stage Topologies

In electric vehicle battery chargers, double stage topologies are more commonly used today [43]. Double stage topologies have two main conversion steps; at first stage from AC to DC and at second stage from DC to DC. This configuration is depicted in Figure 2.1. In a double stage topology, at first stage AC line voltage is rectified to an intermediate DC link voltage [43] using an active rectifier that provides power factor correction (PFC) by keeping the input current in phase with input voltage. Along with PFC operation, it keeps the input current total harmonic distortion (THD) as low as possible to comply with standards. They are also called PFC circuits.

In second stage, conversion from the DC voltage present at the output of PFC to regulated DC charging current takes place. Control feedbacks are employed in second stage to realize CC-CV charging for Li-ion batteries, overcurrent protection and overvoltage protection, etc. In addition, a high frequency transformer can be employed to provide galvanic isolation

between grid and battery. Galvanic isolation is a way of providing double fault protection system that is required for plug-in electric vehicles [44].

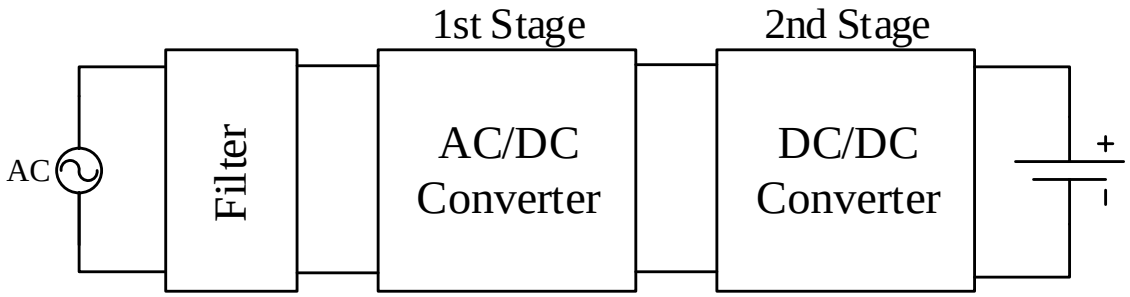

Figure 2.1. Block diagram of double stage topologies

2.1.1 Power Factor Corrector Topologies

In PFC circuits, boost converter topology and its variants are mostly used. In [45] and [46] various unidirectional PFC topologies are reviewed and compared. Conventional boost PFC, which is shown in Figure 2.2, is suitable for applications <1000W power rating, and current ripple, output voltage ripple and component stresses are rather high. Hence, it is not suitable to be used in vehicle battery charger applications. To overcome the shortcomings of conventional boost PFC, interleaved boost PFC are proposed. In interleaved boost PFC, power rating is increased, current stresses and ripples are reduced; however, EMI is still high. To further improve the performance bridgeless interleaved, bridgeless interleaved resonant, phase shifted semi-bridgeless interleaved and back-to-back bridgeless interleaved topologies were proposed. These topologies have various advantages over one another. An efficiency comparison is shown in Figure 2.4.

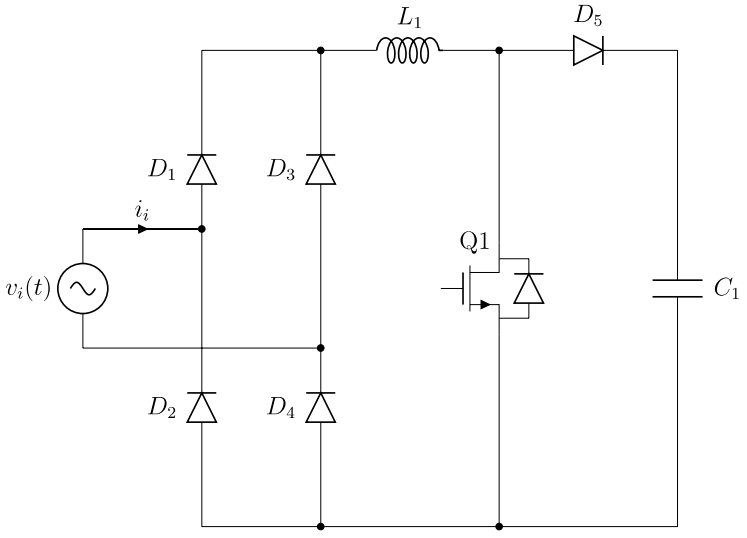

Figure 2.2. Conventional Boost PFC

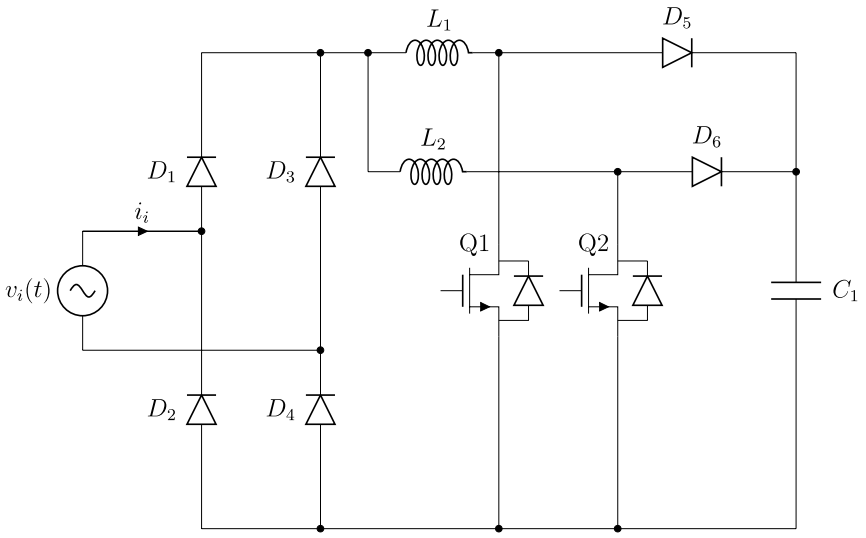

Figure 2.3. Interleaved Boost PFC

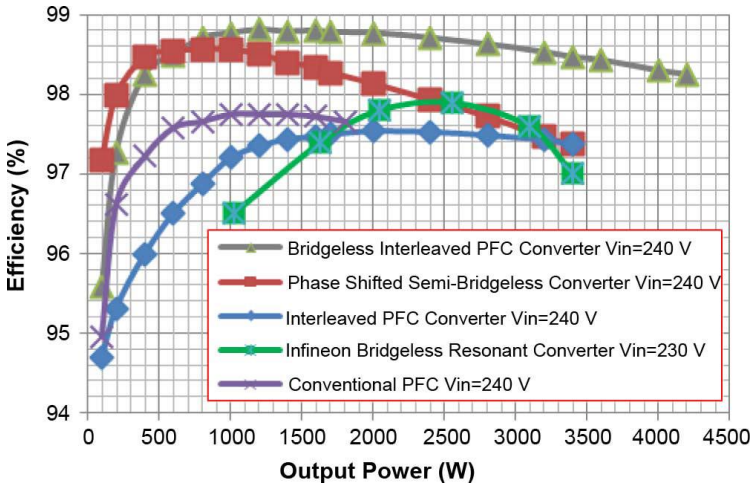

Figure 2.4. Efficiency comparison of unidirectional PFC topologies [45]

To realize bidirectional operation in double-stage topologies both stages have to provide two-way power flow. Israeli et al. [47], proposed that a bidirectional PFC can be used for reactive power compensation purposes. Reactive power compensation might be necessary for the utility grid to keep the power factor of the whole grid close to unity in order to increase the percentage of real power delivered to the loads. Reducing reactive power travelling back and forth through the utility grid also decreases the losses associated with it. In [9] and [48], reactive power compensation is verified for electric vehicle battery chargers using full bridge AC/DC converters. In [49], half bridge, full bridge and three level PWM converters are suggested for bidirectional PFC applications. Half bridge converter is the simplest one among the three and it can be used in three phase applications as well by connecting three single phase converters in parallel. The two major advantages of this converter are its

simplicity and low component count. However, it is hard to suppress harmonics in this converter which can be detrimental to grid and at high power levels component stresses are high which leads to selecting more expensive components.

2.1.2 DC/DC Converters

Among isolated DC/DC converters, full bridge, LLC and their variants stand out for electric vehicle battery charger applications. Phase shifted full bridge (PSFB) converter is implemented in EV battery charger applications successfully [50], [51]. PSFB converters employ a soft-switching technique to reduce the switching losses to reach higher operating frequencies, and reduce the size of passive components. Soft switching is achieved by adjusting the turn-on and off sequences of the switching elements. When a semiconductor switch is about to be turned on, the leakage inductance of the isolation transformer and the output capacitance of the switching element goes into resonance and the voltage on that switching element is reduced or zeroed. Achieving complete soft switching depends of the reactive power stored in the leakage inductance, hence, it is not always possible in light load conditions. In [50], full bridge DC/DC converter stage achieves higher than 95% peak efficiency while operating at wide output voltage levels from 200V to 450V. In [51], full bridge DC/DC converter achieves higher than 96% peak efficiency while operating at 200 kHz switching frequency. It uses newer transistors manufactured with silicon carbide (SiC) semiconductors to reach that level of operating frequency with high efficiency. The system is designed to operate at 6 kW power level which corresponds to Level 2 charging.

LLC resonant converters have the advantage of achieving soft-switching for the entire load range over PSFB converters. A detailed analysis and design methodology is discussed in [52] for LLC resonant converters to be used in battery chargers. A 3.3 kW, 400 V input, 250-450 V output LLC converter achieved 98.2% peak efficiency. Another variant of LLC topology cascaded with buck converter is also presented in [53]. Charger as a whole has 13.1 W/in^3 power density with 6.6 kW rated output power. DC/DC converter stage achieves 97.2% peak efficiency at rated output power.

Achieving isolated bidirectional power flow is possible with dual-active bridges (DAB) and also with the variants of LLC resonant converter topologies. In [53]-[55], variants of LLC topology are used for isolated bidirectional power transfer and galvanic isolation. In [54], peak efficiency of 97.5% is achieved for forward operation and 97% for the backward operation. In [55], similar results are achieved with 97.5% efficiency for both forward and

backward power transfer modes. Circuit schematic of the topology used in [55] is given in Figure 2.5.

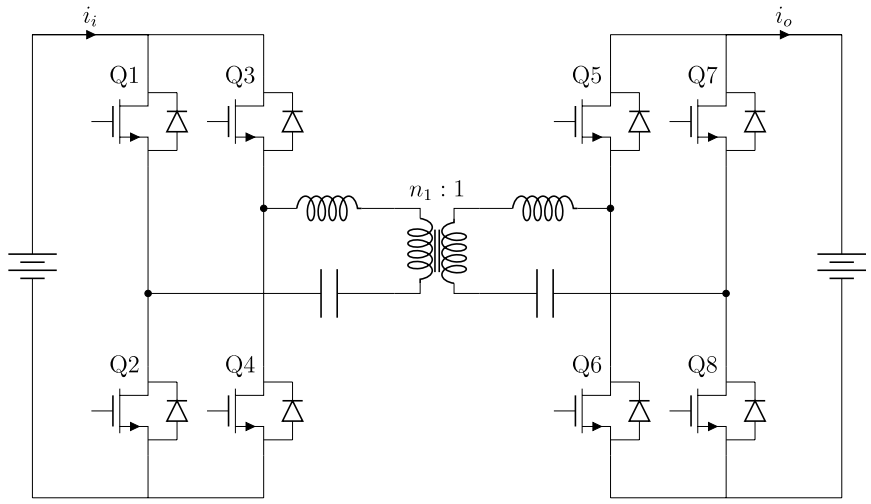

Figure 2.5. CLLC resonant bidirectional DC/DC converter [55]

2.2 Single-Stage Topologies

Although they are less common, single stage isolated topologies are also used in PEV battery charger applications, and they are gaining more popularity because of their compactness, high power density, and lack of electrolytic capacitors. Electrolytic capacitors have limited lifetime which makes them undesirable in automotive applications where durability and long lifetime are important features. Single-stage power conversion results in inherent sinusoidal ripple at twice of the line frequency. This ripple can be filtered out with using large electrolytic capacitors, however that would defeat the purpose of single-stage power conversion. An example topology for unidirectional single-stage converter is reported in [56]. Efficiency is around 92% from 20%-to-100% output power, THD is less than 3% at full load, and PF is about 0.997.

For bidirectional operation, DAB is the most common topology among single-stage converters. A recent DAB-based topology is proposed in [27]. Proposed control scheme brings inherent PFC operation and easily controlled bidirectional power flow. A high frequency transformer also provides galvanic isolation, which increases the safety level. This topology utilizes the leakage inductance of the transformer to transfer power [27]. Experimental prototype is rated at 1.4 kW power level and achieves 89.9% peak efficiency. Another DAB application for bidirectional charger and its control techniques are presented in [57]. The control techniques employed are considerably more complex than that of the presented in [27]; however it can reach higher level of efficiency. It operates with 230 V

RMS grid voltage and 400 V DC output voltage at 3.7 kW rated power level with 2.2 kW/lt power density. Its peak efficiency is higher than 96%. It is specifically designed for PEV battery charger applications.

The circuit schematic of the single-stage DAB converter is given in Figure 2.6. Here, the bidirectional switches are used in the first stage because AC line voltage swings in both positive and negative directions. This can be realized with back-to-back MOSFETs or IGBTs.

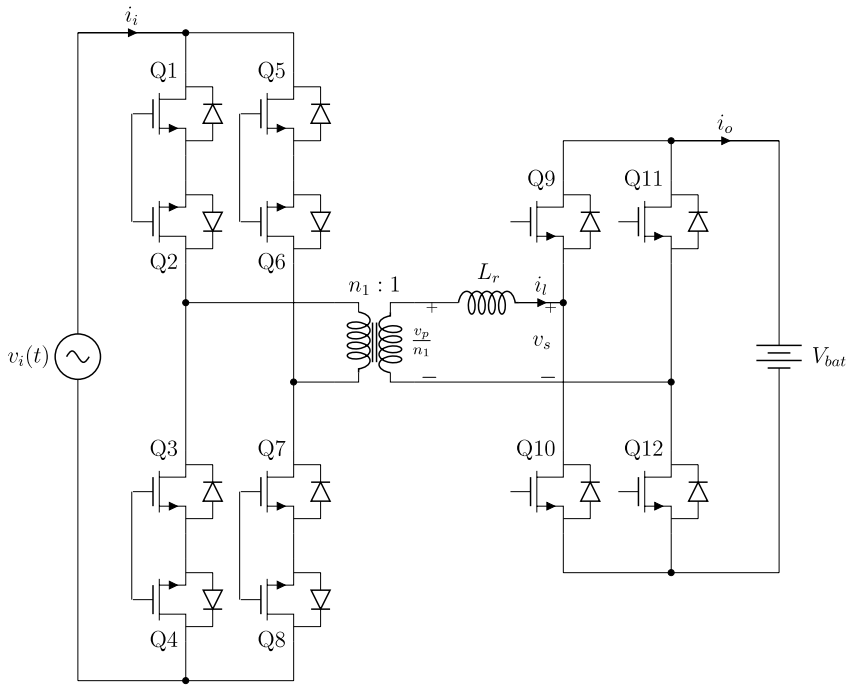

Figure 2.6. Single-phase single-stage DAB AC/DC converter [27]

2.3 Modular Electrical Applications

Modular approach finds its use in many electrical applications. It is convenient for engineers to design a small device and use them to achieve higher specifications by paralleling them where it is possible. Even battery packs used in PEVs are comprised of several cells that are connected series and parallel to achieve higher voltage, power and energy ratings.

Modular structures bring numerous advantages, such as flexibility, ease of maintenance and increased reparability. They are used in power supplies [58], power factor correction applications [59] and especially grid connected photovoltaic (PV) systems [60]-[62]. PV cells are inherently modular, like the batteries. They can be connected in series or parallel to achieve higher voltage and power ratings. When user purchases extra PV modules to increase the solar power capacity, it may be necessary to increase the inverter output power as well. If the inverter is not designed to operate at that power levels, then it should be

replaced with a more powerful one. However, in that case older inverter is redundant and the more powerful one will probably be more expensive than the first and this would significantly increase the cost. Instead, inverters can also be designed as modular structures, then it would suffice to connect another inverter in parallel to increase the total system output. The procedure may be repeated, in case there may be further increase on the PV modules.

On top of the aforementioned advantages, some modular systems can be adjusted to increase the overall system efficiency as well, especially at light loads [59], [60]. When solar radiation decreases due to clouds or position of the Sun, output power from the PVs will decrease as well. Power supplies and inverters in general are designed to provide highest efficiency close to their full load ratings. In case of power decrease in PV panels, if a single inverter is connected to the system, then it would have to operate at lower efficiency. However, in parallel connected modular inverter systems, a number of inverters may be shut down completely and the others would operate at their rated conditions to provide higher overall efficiency, hence increasing the solar power utilization [60].

Possible disadvantages of modular systems may include the increased cost of production, lower power and/or energy density and increased cost of maintenance. Generally, the production cost of a single higher power rated module is lower than multiple modules to achieve the same power. However, this is an optimization problem itself, and by adjusting the power levels of individual modules appropriately the cost per kW power can be kept at acceptable levels, but that will highly depend on the application specifics and requirements.

3. SYSTEM DESIGN

This section will focus on the general system design, different system configurations and the detailed analysis of the system components.

3.1 Modular System Design

Modularity is one of the key aspects of this study. In power electronics applications, modular converters are generally operated at balanced power. However, at light load modules will be operating at even lower power levels. This will be detrimental to the overall system efficiency. The final system to be designed in this study will in fact benefit from modularity to increase the overall system efficiency at light load. This can be realized using two different approaches. First, modules can be turned on/off according to the load demand. This way only one module will operate at the middle of the load/efficiency curve and other operating modules will be used at the full load as it is stated in [60]. Since efficiency of a power electronic converter tends to approach its peak at or near full load, the overall efficiency will be increased. However, there might be a more efficient operating point for a given load. Second method is using the load efficiency curve of each individual module to determine the operating point of each one in a way to maximize efficiency through all load conditions.

This study will focus on designing a system with appropriate power electronic basis for the converters and an optimization controller to orchestrate the operation of the whole system in order to maximize the overall efficiency. To determine the operating point, load/efficiency data of each charger module should be obtained beforehand for both G2V and V2G operations. According to the desired system autonomity and complexity, obtaining the data can be realized in two ways. First method is to obtain efficiency data and loading this information to master controller via human interaction. This method will not be autonomous and require a person to gather information to plot the load/efficiency curves and may be more expensive in the long term. In the second method, each charger module should be designed to be able to monitor and gather its own efficiency data and transmit this data to master controller via a communication interface during a calibration process. This method is fully autonomous and can be easily scaled up or down to achieve lower cost, however initial design phase will be more complex and it will require more effort to calibrate the modules to acquire precise data. Furthermore, master controller configuration that will determine the operating point of each module can be arranged in two different ways. A separate master controller can be utilized to control the operation of *n* number of modules as depicted in Figure 3.1. Second method is embedding the master control algorithm in a

charger module, which will determine the operation point of each controller as well as its own. This configuration is depicted in Figure 3.2. Since performance of MCUs is increased considerably in recent years, second method may be more convenient and cheaper than the first.

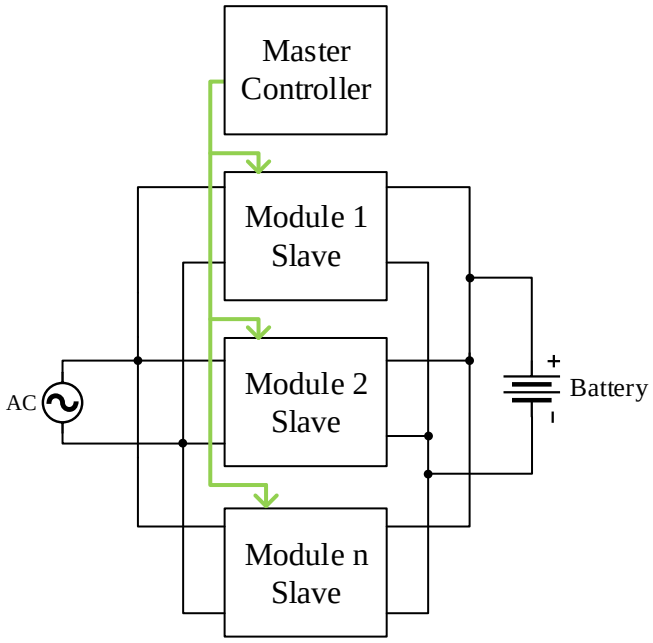

Figure 3.1. Modular system configuration with separate master controller

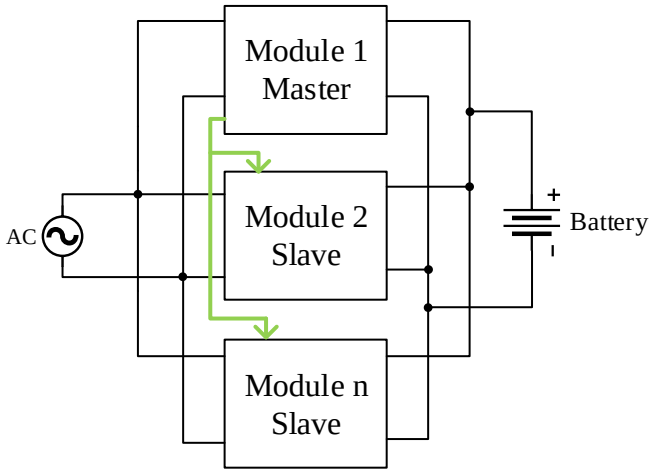

Figure 3.2. Modular system configuration with one module as master controller

Proposed modular system configuration can also be arranged in single- or three-phase configuration to bring higher level of system flexibility and it can be very useful in some countries, especially Turkey and EU countries, where three-phase grid voltage can be used in residential buildings. Three-phase charging may be more preferred at higher power levels, since when phases are operated at balanced power, the net power drawn from the grid will

be DC. In single-phase operation the power drawn from the grid pulsates at twice of the grid frequency. That is why balanced three-phase operation is beneficial for the grid as well.

In single/three-phase configuration, a system depicted in Figure 3.3 can be used to provide transitions between single- and three-phase configurations. In this configuration there are *n* number of strings in which each string has three individual charger modules connected in a way to provide both single- and three-phase power. In three-phase configuration switches S1 and S2 should be left open and in single-phase operation switches S1 and S2 should be closed. In single-phase operation, line and neutral connections should be made between L1 and N nodes respectively. The number of modules for each individual string can be expressed as shown in Figure 3.3 and there are total of *3n* number of charger modules in this system.

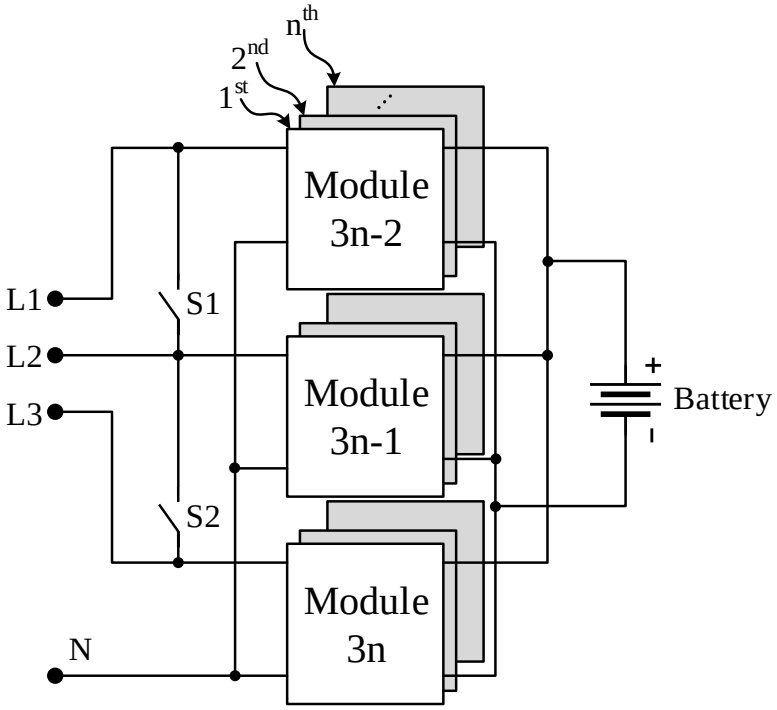

Figure 3.3. Single/Three-phase configuration of modular system

3.2 Optimization

One of the main features of the system is to find the optimal operating point in order to maximize overall efficiency, which is especially beneficial for light load conditions. Finding the optimal efficiency point at all times is especially hard when there are numerous factors affecting the efficiency, such as temperature, input/output voltages and currents, etc. Temperature dependency of efficiency is not easy to model and experimentally it is difficult to gather reliable data. Therefore, this study will not take temperature into account when

forming the efficiency functions. The load/efficiency curves will be obtained and utilized at room temperature. Moreover, the inputs and outputs of the modules are connected in parallel, thus the voltages seen by modules from input and output sides are also the same. This is why input and output voltages will also be left out. In this chapter, load/efficiency behavior of charger modules will be modeled and expressed as mathematical functions, optimization problems to be solved will be formulated and solution methods for constraint optimization problems will be laid out.

3.2.1 Statement of the Optimization Problem

Stating the optimization problem mathematically is a crucial first step in achieving the objective of the study at hand. In this manner, the load/efficiency curves of individual modules should be expressed in mathematical functions with appropriate variables. Since the main property of the system to be designed is charging EV batteries and providing power to the grid, it makes more sense to express the efficiency in terms of charging current in G2V mode, and in terms of grid power in V2G mode. Let's assume that there are n number of modules, then charging current of individual modules can be expressed as i_n and grid power of individual modules can be expressed as p_n. If efficiency of the n^{th} module in V2G mode is expressed as $\eta_{V2G,n}$ and efficiency of the n^{th} module in G2V mode is expressed as $\eta_{G2V,n}$, n number of functions can be written for each operating mode. G2V efficiency of a module can be written as a function in terms of charging current and V2G efficiency of the first module can be written as a function in terms of grid power as it can be seen below.

$$\eta_{G2V,1} = f_{G2V,1}(i_1) \tag{3.1}$$

$$\eta_{V2G,1} = f_{V2G,1}(p_1) \tag{3.2}$$

Overall efficiency function will define a surface in an $(n+1)$-dimensional space. In a system with n number of modules, overall efficiency in G2V mode can be expressed as follows,

$$\eta_{G2V} = \frac{i_1 + i_2 + \cdots + i_n}{\frac{i_1}{f_{G2V,1}(i_1)} + \frac{i_2}{f_{G2V,2}(i_2)} + \cdots + \frac{i_n}{f_{G2V,n}(i_n)}} \tag{3.3}$$

Also, overall efficiency of a system in V2G mode with n number of modules can be expressed as follows;

$$\eta_{V2G} = \frac{p_1 + p_2 + \cdots + p_n}{\frac{p_1}{f_{V2G,1}(p_1)} + \frac{p_2}{f_{V2G,2}(p_2)} + \cdots + \frac{p_n}{f_{V2G,n}(p_n)}} \tag{3.4}$$

The purpose of this study is to maximize η_{G2V} and η_{V2G} using the available information. This maximization can be expressed as a constraint optimization problem. There are three constraints to the optimization problem. First, the sum of charging current or grid power of individual modules should be equal to total demand from the system in terms of charging current or grid power. Second, charging current or grid power of individual modules cannot be negative. Third, steady-state charging current and grid power cannot exceed the rated power and current of the individual modules.

The cost function of this optimization problem is the overall efficiency function of the system for either mode. Also by convention the optimization problem should be formulated so as to minimize the cost function, thus reciprocal of η_{G2V} and η_{V2G} should be used when formulating the problem. Since η_{G2V} and η_{V2G} is always positive and cannot be zero, using the reciprocal will not pose an issue mathematically. In light of this information, formal statement of the optimization problem of this study can be expressed as follows;

$$min \frac{\sum_{k=1}^{n} \frac{p_k}{f_{V2G,k}(p_k)}}{\sum_{k=1}^{n} p_k} \tag{3.5}$$

Subject to;

$$\sum_{k=1}^{n} p_k = p_{demand} \tag{3.6}$$

$$[p_1\ p_2\ \cdots\ p_n] \leq p_{rated} \tag{3.7}$$

$$[-p_1\ -p_2\ \cdots\ -p_n] < 0 \tag{3.8}$$

In G2V mode;

$$min \frac{\sum_{k=1}^{n} \frac{i_k}{f_{G2V,k}(i_k)}}{\sum_{k=1}^{n} i_k} \tag{3.9}$$

Subject to;

$$\sum_{k=1}^{n} i_k = i_{demand} \tag{3.10}$$

$$[i_1\ i_2\ \cdots\ i_n] \leq i_{rated} \tag{3.11}$$

$$[-i_1\ -i_2\ \cdots\ -i_n] < 0 \tag{3.12}$$

There are numerous methods for solving constraint optimization problems. Next section will elaborate these methods.

3.2.2 Solution Methods of the Optimization Problem

The solution method of this optimization problem depends on the available resources. Master controller, whether it is stand-alone or embedded in one of the charger modules, will work in discrete domain and it should be able to solve the optimization problems and decide on the operating point. Analytical methods such as Gradient Descent and Newton's Method can be modified to be executed discretely, or heuristic methods such as Particle Swarm Optimization, Artificial Bee Colony or brute force methods can be used to find the optimal operating point for a given charge or grid power command.

Analytical methods rely on two parameters; namely direction and step size, thus two algorithms should be executed successively in order to determine the direction and step size separately. Name of the analytical methods is based on the direction determining method. Gradient Descent is a first-order iterative optimization algorithm and descent direction is determined from the negative gradient at given point. That way, value of the function is guaranteed to decrease in the next step if the amount of step taken is adjusted appropriately. Too large step might increase the function value and too small step prolongs the time needed to achieve convergence.

Newton's Method not only takes the descent direction into account, it also takes the surface curvature into account to reach the minimum faster. In Newton's Method, quadratic approximation of the cost function is calculated in each step based on Taylor's Expansion of the cost function and minimum point of that approximation is found. Newton's Method

reaches to a local minimum much faster than Gradient Descent in terms of number of steps taken; however, computational power required in each step is also much higher. The main advantage of the Newton's method is that if the cost function to be minimized is quadratic, convergence is achieved in just one iteration, or if it is almost quadratic convergence is achieved in a few steps.

Particle Swarm Optimization (PSO) is a type of swarm intelligence algorithm. In PSO, there are particles each having its own position and velocity in search-space [65]. They move around the search space and gather information. A particle's movement is influenced by randomness, its local best known position and global best position found by other particles. It is expected that this process will guide the particles towards the best positions. Applying PSO is fairly simple and only requires simple mathematical computation in each iteration. Its complexity depends on the size and dimension of the search-space and the number of particles to be deployed.

Artificial Bee Colony (ABC) is also a type of swarm intelligence algorithm and it is based on the behavior of honey bees. In an ABC system, there are three different type of bees; namely, employed bees, onlooker bees and scout bees. Employed bees are randomly scattered around the search-space to food sources, and these food sources represent the solution candidates. They then evaluate the nectar amount in the food sources, i.e., the fitness of the solution candidate and share this information with onlooker bees. Onlooker bees go to the food sources in the neighborhood of the best ones. Worst food sources are abandoned by employed bees and these bees become scout bees and search new food sources randomly. This process attempts to guide the bees towards the best food source by combining global and local search methods [66].

Brute force methods try to find the optimal solution by evaluating the cost function for all possible combinations of the inputs with a predetermined sampling interval. If solution accuracy is to be increased, the number of candidates to be evaluated to reach the optimal solution increases exponentially. A close approximation of the optimal solution can be determined by adjusting the sampling interval appropriately.

Any of the three methods mentioned can be utilized in the solution of the optimization problem defined in previous section. When number of charger modules in the system is higher than a certain number, application of brute force methods might require more memory

than available. And when number of charger modules is less than a certain number, application of swarm intelligence methods might prove costlier and less efficient.

3.3 Power Electronic Basis of the System

3.3.1 Selection of Converter Topology

The selection of the suitable power conversion topology is crucial for the realization of modularity in addition to bidirectional operation. Isolation, compactness and high efficiency are also desirable properties for a PEV battery charger unit. Providing isolation in a compact form is a challenging task with double-stage topologies. It is more suitable to follow single-stage power conversion techniques to provide both isolation and compactness at the same time. There is a growing interest in single-stage power conversion topologies in the literature as well. Implementing a single-stage topology for a PEV charger would align with the approach of this study to keep up with the current trends in technology and recent literature. Because of these reasons a single-stage isolated bidirectional topology based on DAB [27] is selected for the study.

DAB topology can be used in the study with a few modifications to provide more flexibility in component selection and to prevent potential problems and issues. Modified circuit model of the topology to be used in the study is depicted in Figure 3.4. There are two main modifications to the circuit. First, in [27] power flow in the first stage for both positive and negative cycles of grid voltage is realized by using dual IGBT switches that operates in the four quadrants of voltage-current plane. That way all switches in the first stage experiences high frequency switching loss and this may reduce the overall efficiency of the charger. Instead, a low frequency front-end synchronous rectifier can be employed to separate the dual switches in the first stage. In this manner, since first full-bridge comprised of Q1-Q4 just rectifies the line voltage at the line frequency and takes no part in high-frequency power conversion, it is not considered as a power conversion stage and only conduction losses will be effective in this stage. Second, the average current flowing in the transformer may increase or decrease ever so slightly due to possible imbalance between the transitions of the semiconductor switches. This may cause flux imbalance and drive the transformer into saturation, and wreak havoc in the operation of the charger. This phenomenon can be avoided by using a DC blocking capacitor C_{dcblk} at the secondary side of the transformer.

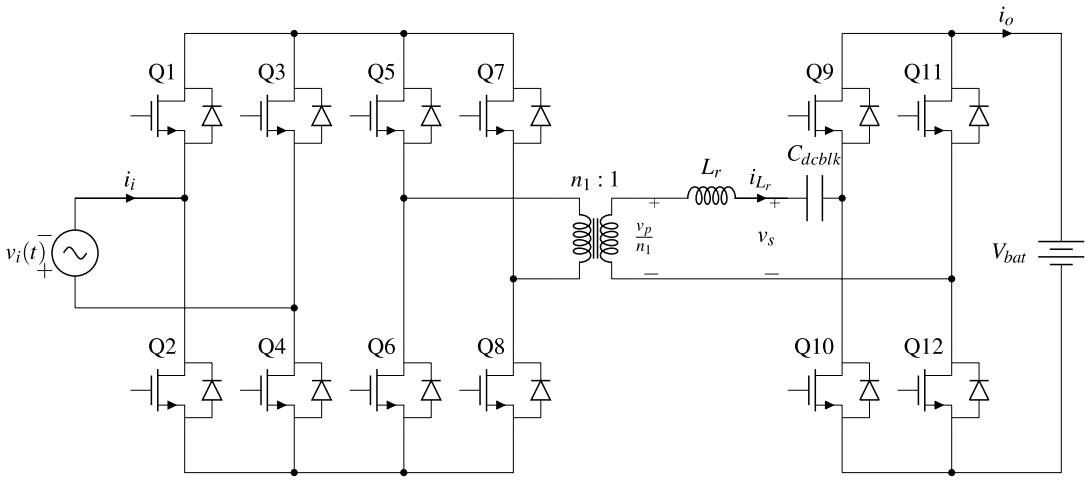

Figure 3.4. Single-phase single-stage DAB AC/DC converter with a separate synchronous rectifier

The modulation scheme employed in [27] suggests that the current waveform will track the input voltage at any time. This feature of the control method is crucial for modular operation. That means the modules connected at the same voltage bus will track the line voltage whatever the operating conditions of the independent modules may be. Technical details about the topology will be explained in detail in further sections.

3.3.2 Mathematical Analysis of the Topology

In this section, detailed analysis of the converter operation will be shared according to the modulation scheme given in [27]. In this modulation scheme, leakage inductance of the transformer is used to realize power transfer from either side to the other. For the analysis, this configuration will be modeled as an ideal transformer with an additional discrete inductance representing the leakage inductance of the transformer. Furthermore, all components are assumed to be ideal. The converter that will be designed in the study will operate between the utility grid and a battery pack. In this manner the primary AC side supply will be modeled as sinusoidal source with constant amplitude and secondary DC side will be modeled as a constant DC source.

The schematic of the topology is given previously in Figure 3.4. Primary side consists of eight 2-quadrant switches. First four switches, Q1-Q4, are used to rectify the AC line voltage at the line frequency. Consecutive four switches, Q5-Q8, are used for high frequency AC chopping at 50% duty cycle. This is performed to utilize a high frequency transformer to realize galvanic isolation. Four switches at the secondary are then used to apply a voltage pulse to charge and discharge L_r as required to shape the input current and transfer power.

Necessary voltage and current waveforms of one complete modulation cycle is given in Figure 3.5. Detailed explanation of the modulation cycle is given in Section 3.3.2.1.

3.3.2.1 Modulation Scheme

The operation of the synchronous rectifier is relatively straightforward. During positive AC cycle, Q1-Q4 will be ON and during negative AC cycle Q2-Q3 will be ON to rectify the line voltage. Assuming the AC source has a voltage in the form of;

$$v_i(t) = V_i \, sin(2\pi f_i t) \tag{3.13}$$

Where V_i is the amplitude of the line voltage and f_i is the input frequency; rectified voltage can be expressed as;

$$v_r(t) = |V_i sin(2\pi f_i t)| \tag{3.14}$$

The operation of the high frequency AC chopper is also similar to the synchronous rectifier in the sense that cross-pair of switches operate in parallel, but only at a much higher frequency. Q5-Q8 and Q6-Q7 will be switched complementarily at a switching frequency f_s with 50% duty cycle, where $f_s \gg f_i$. Then transformer primary voltage can be expressed as;

$$v_p(t) = \begin{cases} v_i(t), 0 < t < \dfrac{T_s}{2} \\ -v_i(t), \dfrac{T_s}{2} < t < T_s \end{cases} \tag{3.15}$$

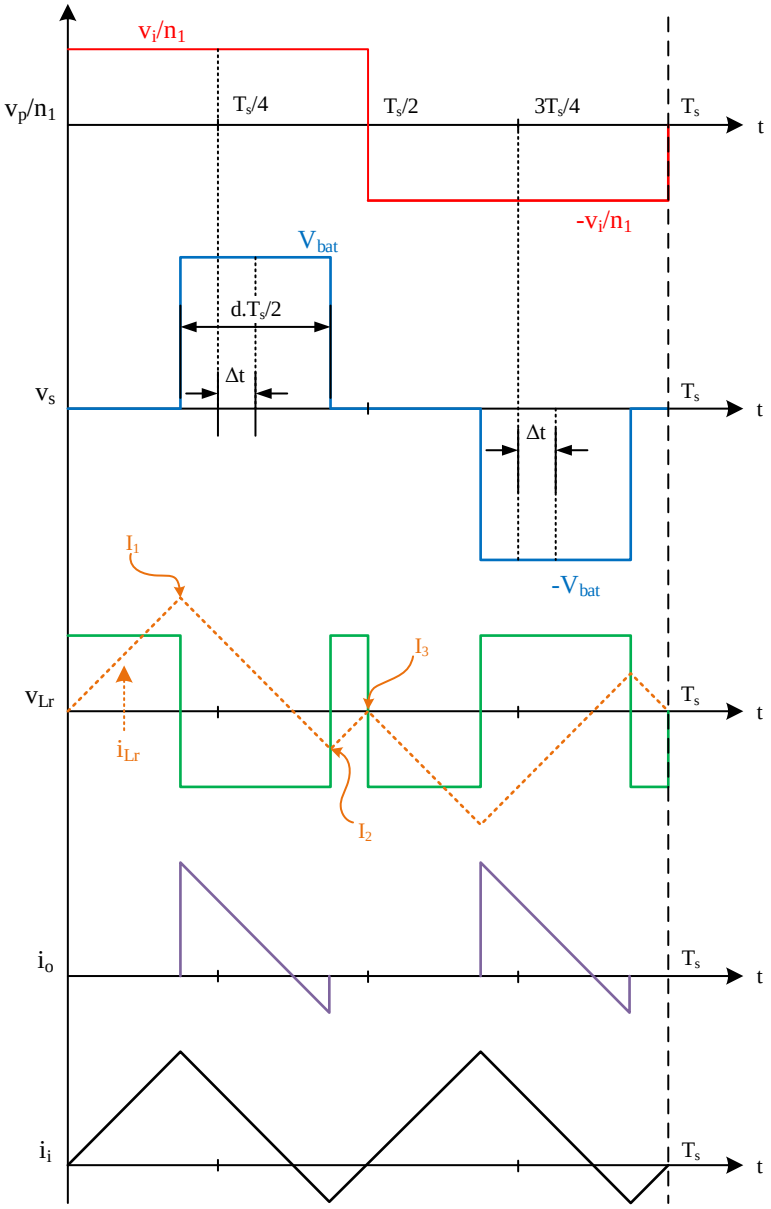

Figure 3.5. Modulation scheme for one switching cycle [27]

The voltage on the transformer secondary then can be expressed as;

$$\frac{v_p(t)}{n_1} = \begin{cases} \frac{v_i(t)}{n_1}, 0 < t < \frac{T_s}{2} \\ \frac{-v_i(t)}{n_1}, \frac{T_s}{2} < t < T_s \end{cases} \tag{3.16}$$

The duty cycle of the voltage pulse applied by the secondary side switches in a half switching cycle will be adjusted by the ratio of the transformer secondary side voltage to the DC output voltage, i.e.,

$$d(t) = \frac{v_p(t)/n_1}{V_{bat}} \tag{3.17}$$

Also a phase shift will be introduced to the voltage pulse with respect to the primary side voltage. Phase shift will be limited so as to restrict the voltage pulse to the related half switching cycle. This restriction can be expressed mathematically as follows;

$$|\Delta t| < \frac{T_s}{4}(1 - \hat{d}) \tag{3.18}$$

Where $\hat{d}$ is the peak duty cycle, which can be expressed as;

$$\hat{d} = \frac{V_i/n_1}{V_{bat}} \tag{3.19}$$

For the sake of convenience a new quantity based on the phase shift will be defined, namely phase shift ratio which is expressed by δ.

$$\delta = \frac{\Delta t}{T_s/4} \tag{3.20}$$

Then $|\Delta t|$ restriction can be more simply expressed in the form of δ and $\hat{d}$ as follows;

$$\delta < (1 - \hat{d}) \tag{3.21}$$

With all the timing scheme given, the voltage $v_s(t)$ applied by the secondary side switches can be expressed as follows;

$$v_s(t) = \begin{cases} 0, 0 < t < \frac{T_s}{4}(1-d+\delta) \\ V_{bat}, \frac{T_s}{4}(1-d+\delta) < t < \frac{T_s}{4}(1+d+\delta) \\ 0, \frac{T_s}{4}(1+d+\delta) < t < \frac{T_s}{2} + \frac{T_s}{4}(1-d+\delta) \\ -V_{bat}, \frac{T_s}{2} + \frac{T_s}{4}(1-d+\delta) < t < \frac{T_s}{2} + \frac{T_s}{4}(1+d+\delta) \\ 0, \frac{T_s}{2} + \frac{T_s}{4}(1+d+\delta) < t < T_s \end{cases} \quad (3.22)$$

The timing of gate signals of the high frequency (HF) switches to apply this modulation scheme is shared in Figure 3.6.

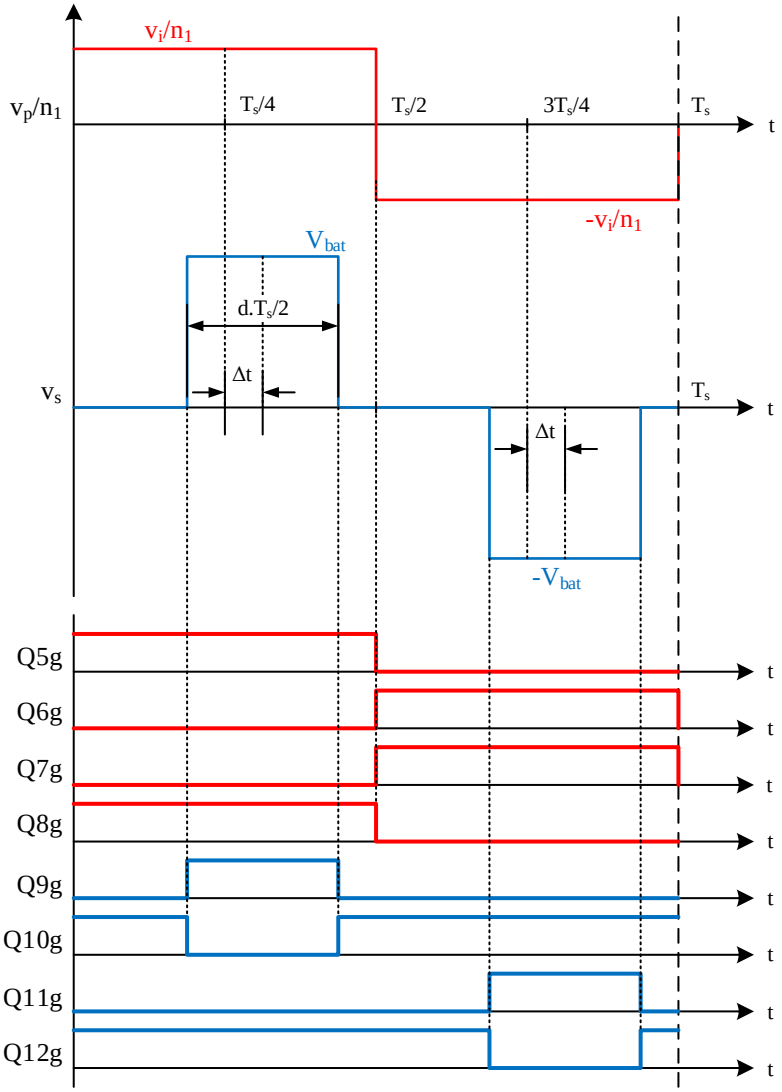

Figure 3.6. Gate Signals of HF switches

3.3.2.2 Current and Power Transfer Relationships

Since the topology is assumed to be lossless in the analysis, the voltage and the current of the leakage inductor can be expressed as follows;

$$\frac{v_p(t)}{n_1} - v_s(t) = v_{L_r}(t) = L_r \frac{di_{L_r}}{dt} \tag{3.23}$$

$v_s(t)$ and $v_p(t)$ was given previously, thus $v_{L_r}(t)$ for one complete switching cycle can be obtained as follows;

$$v_{L_r}(t) = \begin{cases} \frac{v_i}{n_1}, 0 < t < \frac{T_s}{4}(1 - d + \delta) \\ \frac{v_i}{n_1} - V_{bat}, \frac{T_s}{4}(1 - d + \delta) < t < \frac{T_s}{4}(1 + d + \delta) \\ \frac{v_i}{n_1}, \frac{T_s}{4}(1 + d + \delta) < t < \frac{T_s}{2} + \frac{T_s}{4}(1 - d + \delta) \\ \frac{v_i}{n_1} + V_{bat}, \frac{T_s}{2} + \frac{T_s}{4}(1 - d + \delta) < t < \frac{T_s}{2} + \frac{T_s}{4}(1 + d + \delta) \\ \frac{v_i}{n_1}, \frac{T_s}{2} + \frac{T_s}{4}(1 + d + \delta) < t < T_s \end{cases} \tag{3.24}$$

Assuming inductor current starts at 0 at the beginning of the switching cycle, it will linearly increase until it reaches I_1. I_1 can be expressed from the inductor voltage-current equation as follows;

$$\frac{v_i}{n_1} = L_r \frac{I_1}{\frac{T_s}{4}(1 + \delta - d)} \tag{3.25}$$

$$I_1 = \frac{v_i}{n_1} \frac{T_s}{4L_r}(1 + \delta - d) \tag{3.26}$$

Similarly, inductor current will start to decrease linearly to I_2 and it will increase linearly until it reaches I_3. These currents can be expressed in similar manner to I_1 as follows;

$$I_2 = I_1 + (\frac{v_i}{n_1} - V_{bat}) \frac{dT_s}{2L_r} \tag{3.27}$$

$$I_3 = I_2 + (\frac{v_i}{n_1} - V_{bat}) \frac{T_s}{4L_r}(1 - \delta - d) \tag{3.28}$$

The inductor current waveform will be mirrored with respect to the horizontal axis since the voltage on the inductor is also mirrored with respect to the horizontal axis. Also, it can be

seen from the volt-second balance, the average voltage on the inductor in the half switching cycle, and the current expressions that when the inductor current starts from zero, it will again be zero at the end of half switching cycle.

$$\int_{0}^{\frac{T_s}{4}(1+\delta-d)} v_i\,dt + \int_{\frac{T_s}{4}(1+\delta-d)}^{\frac{T_s}{4}(1+\delta+d)} \left(\frac{v_i}{n_1} - V_{bat}\right)dt + \int_{\frac{T_s}{4}(1+\delta+d)}^{\frac{T_s}{2}} v_i\,dt = 0 \qquad (3.29)$$

Please note that, the inductor current is the same as the transformer secondary side current and it will be scaled with the transformer turns ratio to the primary side. Transformer primary side current is also passing through the AC side HF switching devices. Also please note that the HF AC side switches are switched at every half cycle. This observation leads to Zero Current Switching (ZCS) of the AC side HF switches at all load conditions; hence eliminating the switching losses for AC side HF switches.

Average AC source current can be found by averaging the inductor current in the half switching cycle with taking transformer turns ratio into account.

$$\overline{i_i}(t) = \frac{2}{n_1 T_s}\int_{0}^{\frac{T_s}{2}} i_{L_r}(\tau)d\tau \qquad (3.30)$$

$$\overline{i_i}(t) = \frac{\delta V_{bat}}{4n_1 L f_s}\,d(t) \qquad (3.31)$$

Given that, battery voltage, leakage inductance, switching frequency and transformer turns ratio is constant, AC source current depends on duty ratio and phase shift ratio. Duty ratio is defined in (3.17) and it is sinusoidally changing with the AC source voltage. This results in the following relationship;

$$\overline{i_i}(t) = \frac{\delta V_{bat}}{4n_1 L f_s}\frac{v_i(t)}{n_1 V_{bat}} \qquad (3.32)$$

$$\overline{i_i}(t) = \frac{\delta V_i}{4n_1^2 L f_s}\sin(2\pi f_i t) \qquad (3.33)$$

The last relationship for the AC source current provides three crucial insights for the operation of the topology. First, amount of current delivered is proportional to the phase shift ratio and current/power can be controlled easily by changing the phase shift ratio. Second, sign of phase shift ratio can be toggled to change the direction of the current, hence

bidirectional power flow. Three, AC source current is in phase with the AC source voltage, resulting in open-loop power factor correction.

Assuming the topology is lossless, average output power will be same as average input power. This power relationship can be used to obtain DC side battery current.

$$\overline{i_{bat}}(t) = \frac{\delta V_i^2}{4n_1^2 L f_s V_{bat}} \sin^2(2\pi f_i t) \tag{3.34}$$

This relationship can also be written in the following manner;

$$\overline{i_{bat}}(t) = \frac{\delta V_i^2}{8n_1^2 L f_s V_{bat}} (1 - \cos(4\pi f_i t)) \tag{3.35}$$

DC side current has a constant DC component and AC component at twice the frequency of the AC source voltage. When DC current is multiplied with the battery voltage, transferred output power can be expressed in the form of;

$$\overline{P_{bat}}(t) = \frac{\delta V_i^2}{8n_1^2 L f_s} (1 - \cos(4\pi f_i t)) \tag{3.36}$$

And average power in one grid cycle can be expressed as;

$$\overline{P_{bat}} = \frac{\delta V_i^2}{8n_1^2 L f_s} \tag{3.37}$$

As can be seen in (3.37), output power is directly proportional to phase shift ratio. This phenomenon can be used to control the power of current to be delivered to either side. Also the amount of power to be transferred is inversely proportional to leakage inductance and switching frequency and it is related to the square of amplitude of AC source voltage. By choosing the appropriate values for the inductance, switching frequency and the turns ratio of the transformer, a wide operating range for the AC and DC side voltages can be obtained.

3.3.2.3 Soft Switching for DC Side Switches

Soft switching is an important improvement for any type of power converter, since it eliminates switching losses, greatly decreases electromagnetic interference and allows the power converter to be operated at much higher switching frequencies. In the selected topology, DC side switches can achieve soft switching under all load conditions. When any of the DC side switches is to be turned on, the inductor current should be in particular direction and amount, and this current should discharge the output capacitance of the

MOSFET to be turned on before its gate pulse is applied. To achieve this, a certain amount of dead-time should be introduced for each MOSFET in each half bridge for DC side full bridge. This condition is more vividly shown in Figure 3.7 and Figure 3.8.

In Figure 3.8 (a), Q10 is just switched OFF and Q9 is about to be switched ON. At this instant, inductor current is in positive direction and during dead-time inductor current can only flow through Q9's body diode. In dead-time interval, inductor current should discharge the output capacitance of Q9 to decrease $Q9_{ds}$ voltage to approximately zero. After that is achieved, Q9 can be turned ON at zero voltage. Other cases given in Figure 3.8 (b), Figure 3.8 (c) and Figure 3.8 (d) can be explained in similar manner.

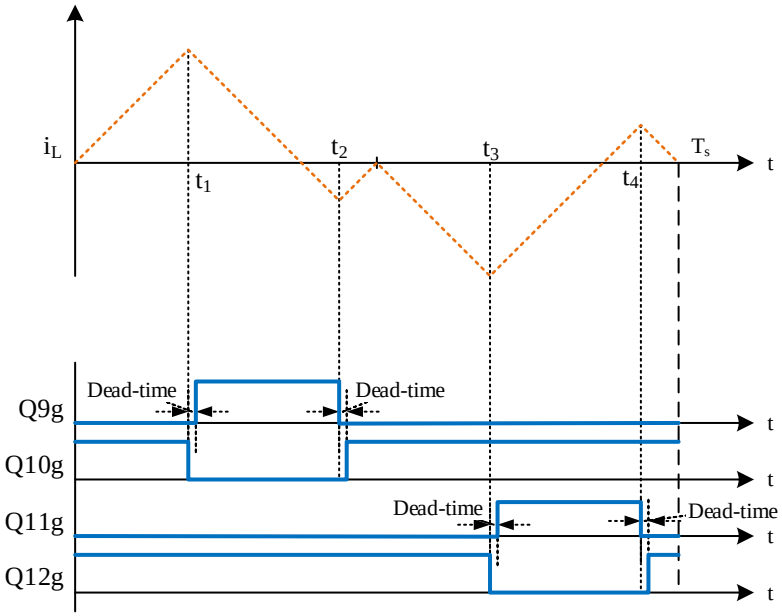

Figure 3.7. Gate signals for Zero Voltage Switching

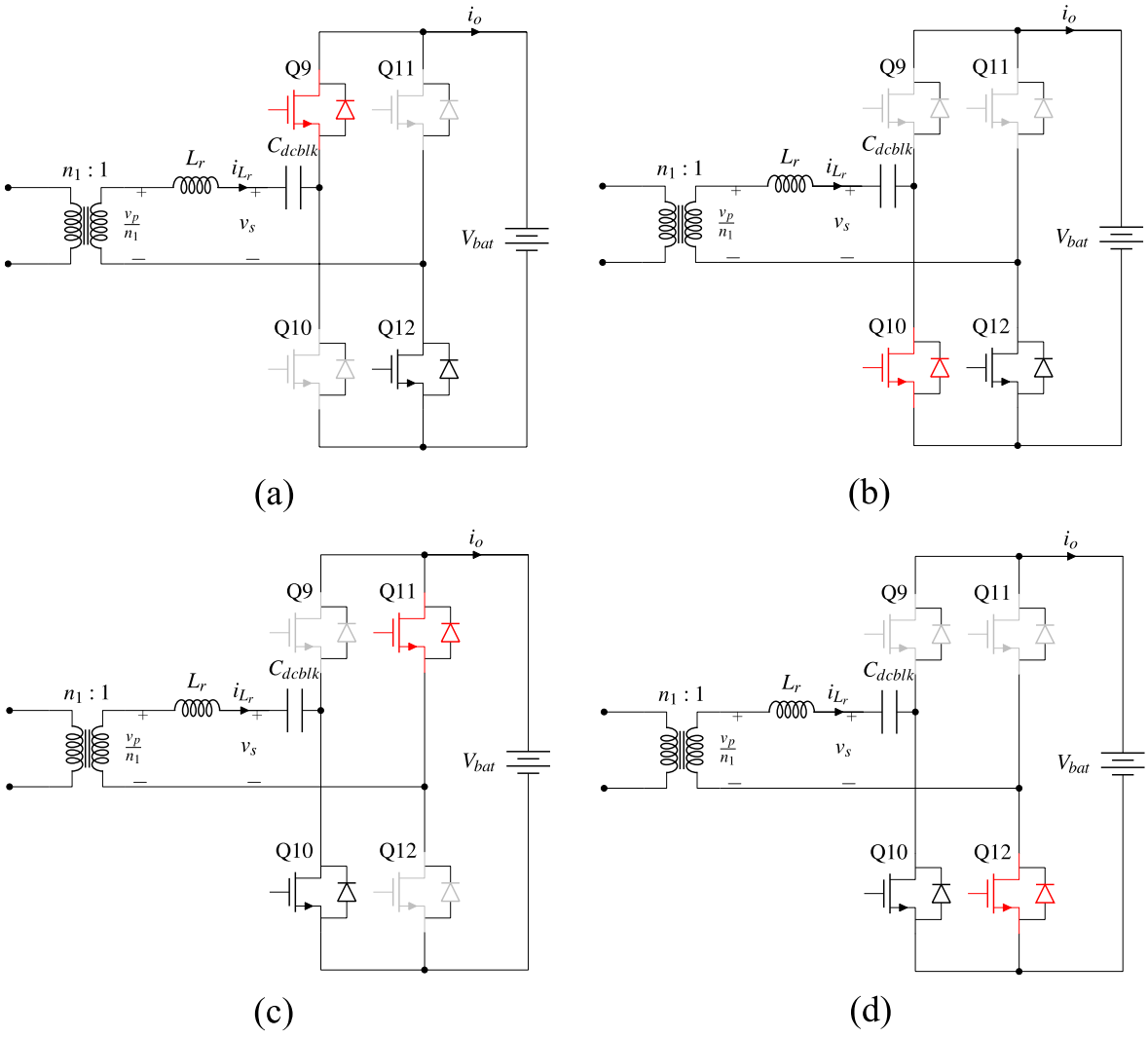

Figure 3.8. DC side MOSFETs' switching instants. (a) $t=t_1$. (b) $t=t_2$. (c) $t=t_3$. (d) $t=t_4$.

4. SIMULATION RESULTS

4.1 Single Module Conceptual Simulation

Selected topology is not readily used in EV chargers and the proposed modulation scheme [27] is relatively new. Because of that, as first step in system design, the operation of a single module is verified. To get fast initial results, PLECS is selected as a first simulation medium. Since the components are assumed to be ideal, grid is modelled as an AC source, semiconductor switches are realized with MOSFETs with body diodes, high frequency transformer is modelled as an ideal transformer and a discrete inductance, and battery is modeled as a constant DC source with a series resistance. Control algorithm described in [27] implemented using the C-block in PLECS. Simulation setup is given in Figure 4.1.

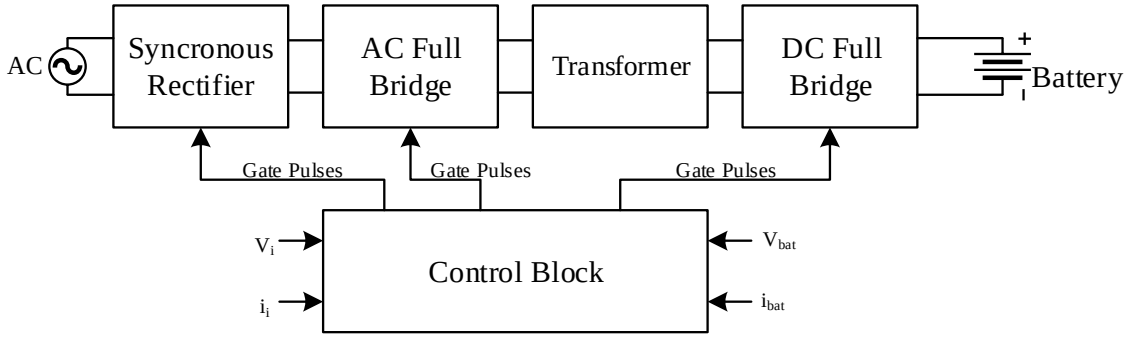

Figure 4.1. Simulation setup

4.1.1 Open Loop Simulation

At first the simulation is run open-loop and the theoretical operation of the charger is verified for bidirectional power flow by adjusting the phase shift ratio. Open loop simulation parameters are given in Table 4.1. Two simulation scenarios are realized and this is given in Table 4.2.

Table 4.1. Parameters for open loop simulation

Grid Voltage/Frequency	230 Vrms/50Hz
Battery Voltage	200 V
Transformer Turns Ratio	3:1
Leakage Inductance	15 µH
Switching Frequency	25 kHz
Rated Grid Power	600 W
Rated Charging Current	3 A

Table 4.2. Simulation scenarios

Simulation 1	Simulation 2
δ = 0.25	δ = -0.25

The steady state results of the simulation are given in Figure 4.2 and Figure 4.3. In both cases, current harmonics are very low and power factor is unity. This is because grid current waveform is obtained by an averaging block instead of a filter. In real world, the switching ripple of the grid current will be filtered out with LC filter and that will introduce certain amount of reactive power to the grid.

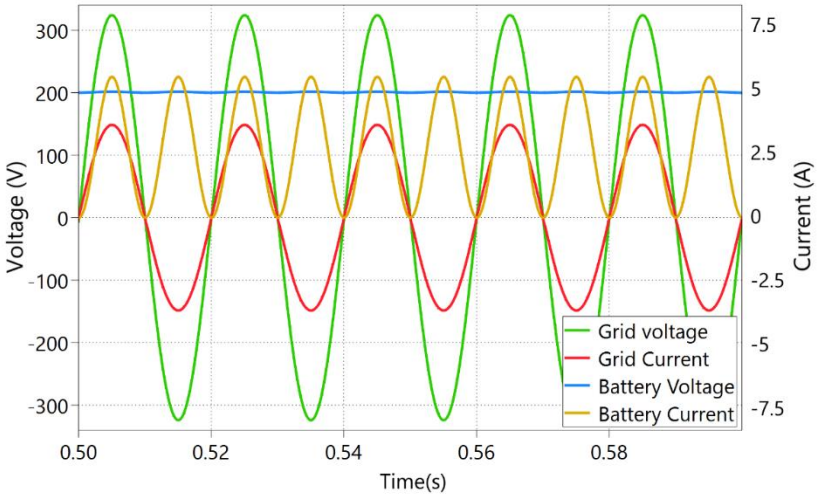

Figure 4.2. Open loop simulation result for case 1, δ=0.25.

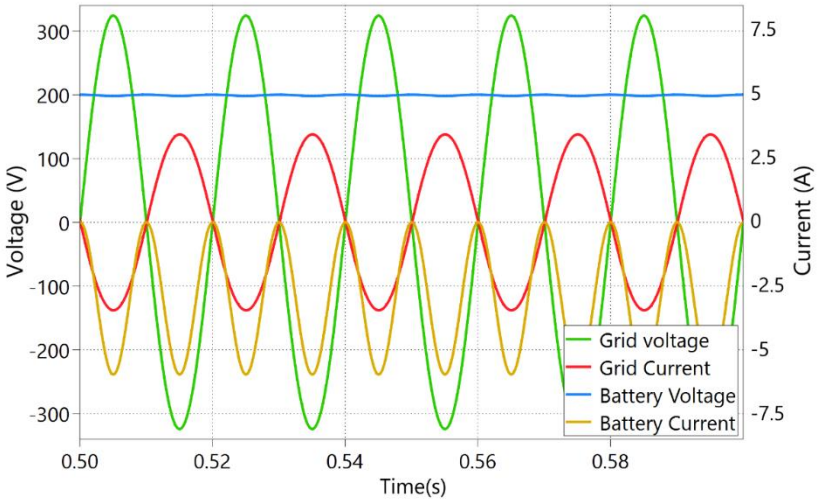

Figure 4.3. Open loop simulation result for case 2, δ=-0.25.

4.1.2 Closed Loop Simulation

Closed loop control of the charger is realized by discrete PI controllers. As stated in mathematical analysis section, phase shift ratio can be adjusted to control current or power flow to either side. For charging operation, controlling charging current makes more sense and for V2G operation, controlling power makes more sense. PI control loop of charging operation is depicted in Figure 4.4. For charging operation, actual battery current is measured and subtracted from reference charge current. Resulting error is fed to PI controller, whose output determines phase shift ratio.

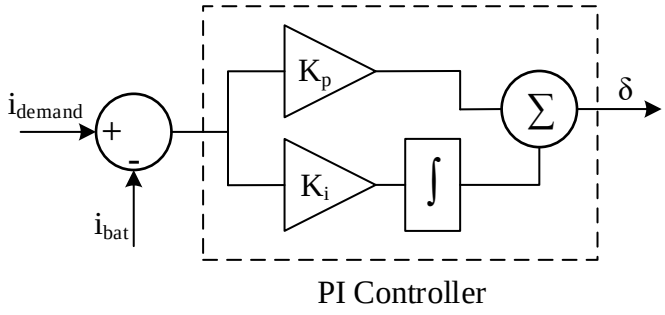

Figure 4.4. Controller for charging operation

To supply power to grid, actual voltage and current have to be measured at the point of connection to the grid. When this is accomplished, power flowing from the charger can be calculated based on this data. Since the simulation setup does not include any reactive elements, reactive power of the charger will be zero. When the system is to be implemented in real world, phase angle of the current should be measured to accurately calculate the real power. Real power value is then subtracted from power reference to generate power error signal. This error is then fed to a PI controller to generate phase shift ratio which adjusts the power flowing to the grid. This controller configuration is shown in Figure 4.5.

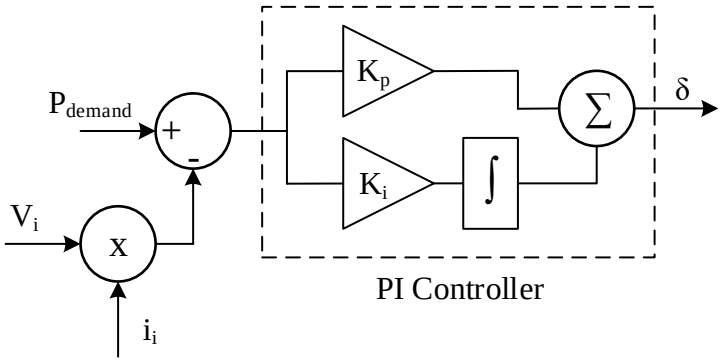

Figure 4.5. Controller for V2G operation

Executing both of the controllers concurrently will create conflicts in system operation, thus this scenario must be avoided. That is why a reference selecting algorithm should be used in order to select the positive reference and utilize the relevant controller based on the reference. If both of the references are positive, deciding algorithm turns off the charger. Final configuration of the closed-loop controller is given in Figure 4.6.

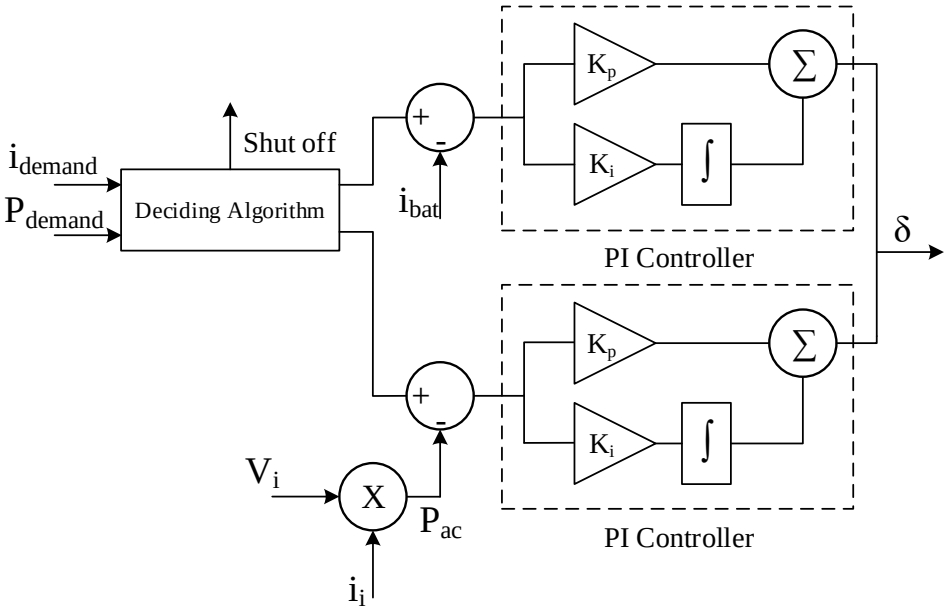

Figure 4.6. Closed-loop system controller.

To verify the operation of the closed-loop system controller, a simulation scenario is developed in which both current and power references change in time and overlap for certain duration of time. This is depicted in Figure 4.7.

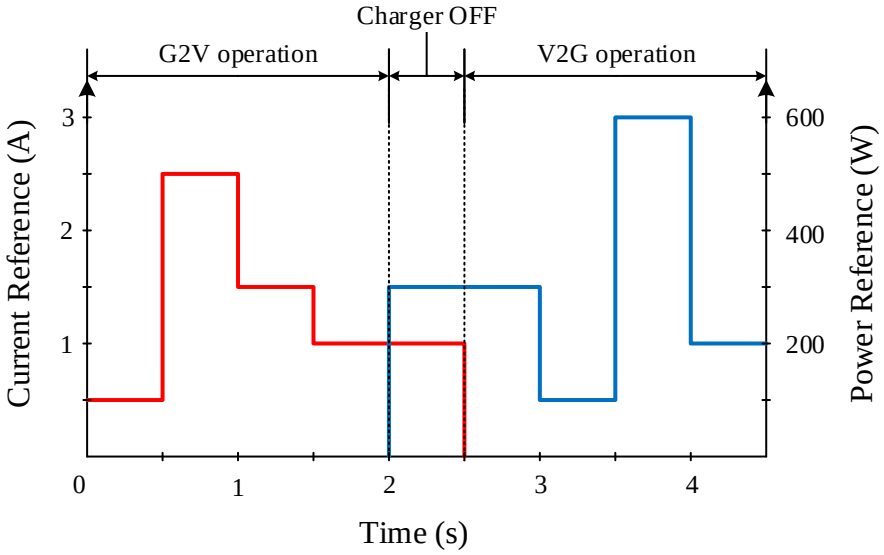

Figure 4.7. Closed-loop simulation reference signals.

The response of the charger's control algorithm is given in Figure 4.8. As it can be seen, charger responds to the reference signals in very short time, settling time is short and overshoot is small. Also, in the interval when the two references are positive, charger does not operate.

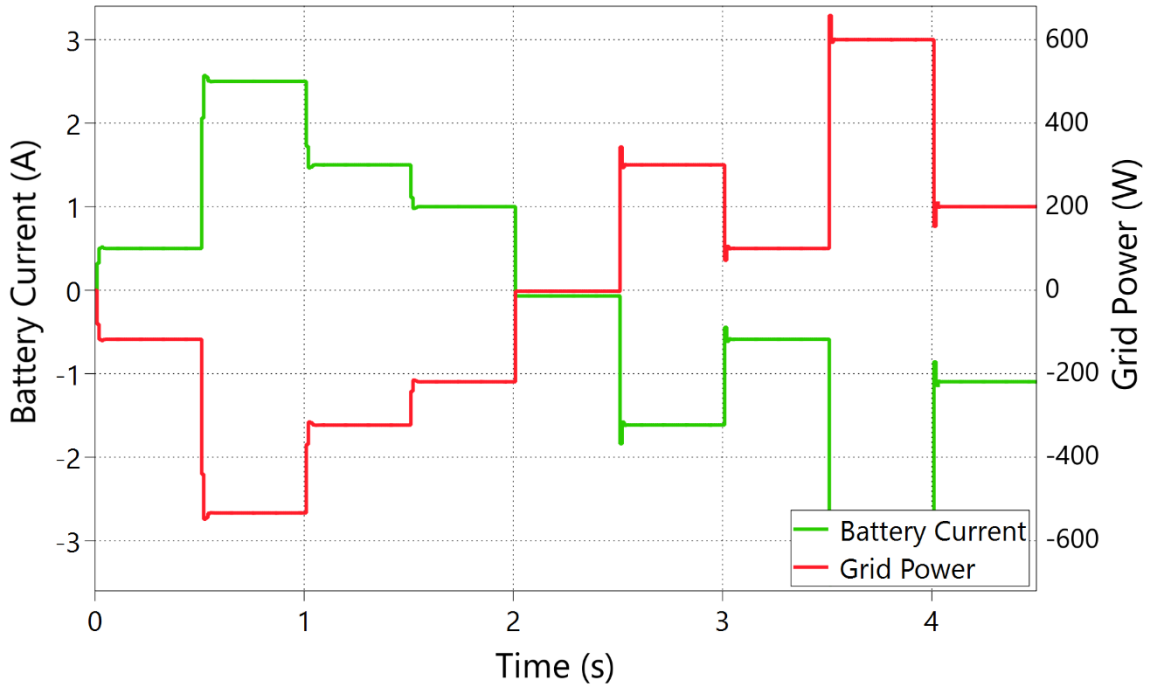

Figure 4.8. System closed-loop response to reference signals.

4.2 Modular System Simulation

Modular system simulation is verified with two individual modules where one of them is in master configuration and the other is in slave configuration. Master charger module gets grid power and charging current demand, applies optimization algorithm and commands the other module accordingly. Each module has its own closed-loop controllers and they act to achieve the desired command given to them. This chapter will focus on the verification of the proposed idea through computer simulations.

4.2.1 Simulation Setup and Optimization Algorithm

Simulation system setup is built as depicted in Figure 4.9. Modular system simulation should verify the benefits of the optimization controller by comparing the efficiency increase between equal current sharing and optimized current sharing. The proposed modular system should have higher overall efficiency at low to moderate loads compared to a modular system in which all the modules are operated at balanced power. Since there is no working hardware prototype during the simulations yet, two modules with hypothetical

load/efficiency curves are assumed. These curves are depicted in Figure 4.10 and Figure 4.11.

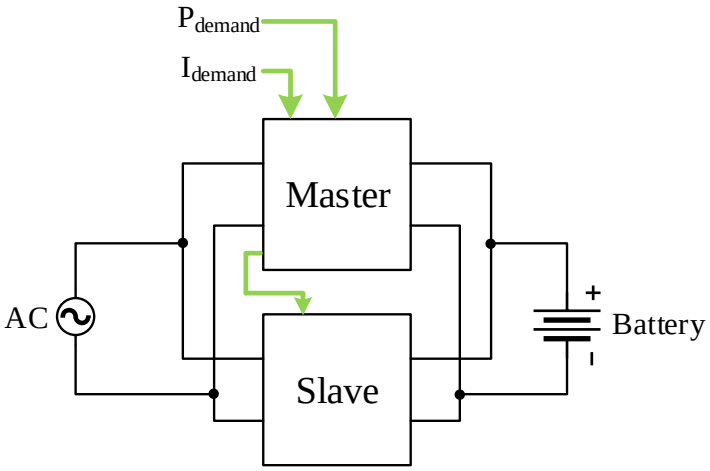

Figure 4.9. Modular system simulation setup

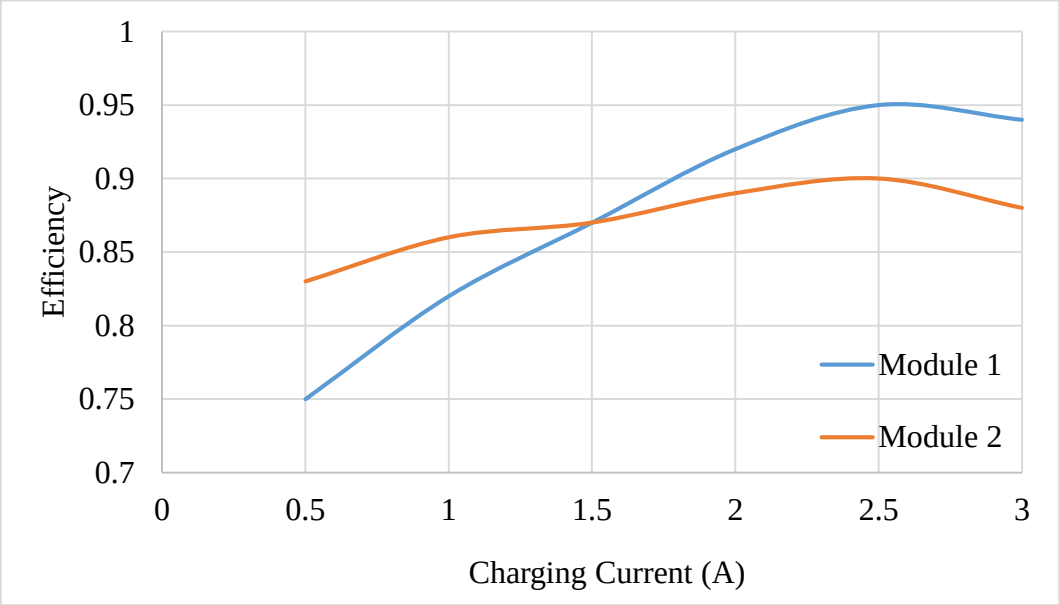

Figure 4.10. Charging current vs efficiency curves of simulation models

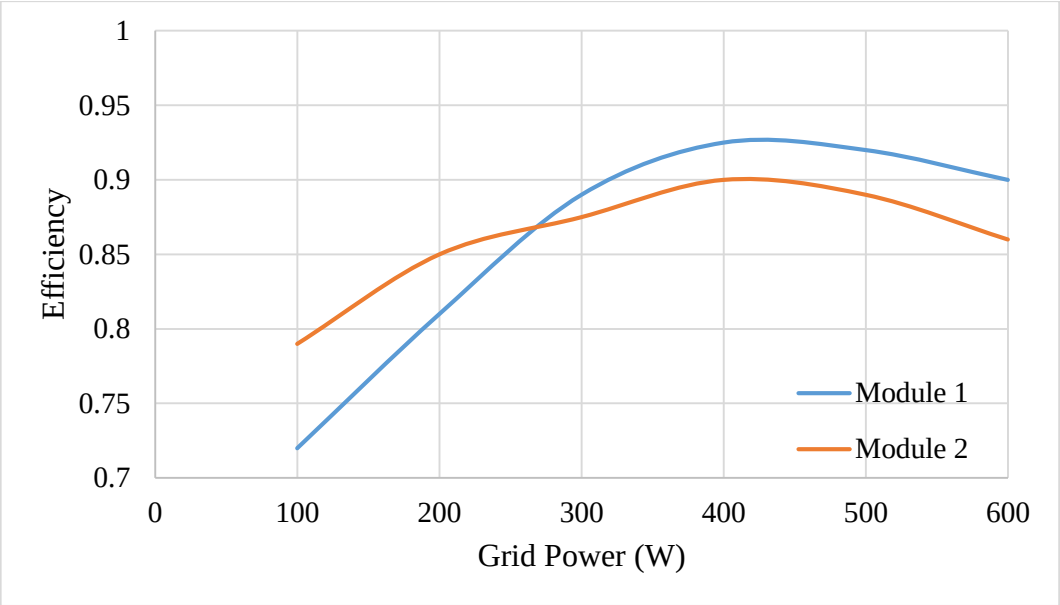

Figure 4.11. Grid power vs efficiency curves of simulation models

Load/efficiency curves are fitted to polynomials using MATLAB. Also surface function representing the overall efficiency of the modular system in G2V mode is depicted in Figure 4.12. A similar surface representation can be obtained for V2G mode as well.

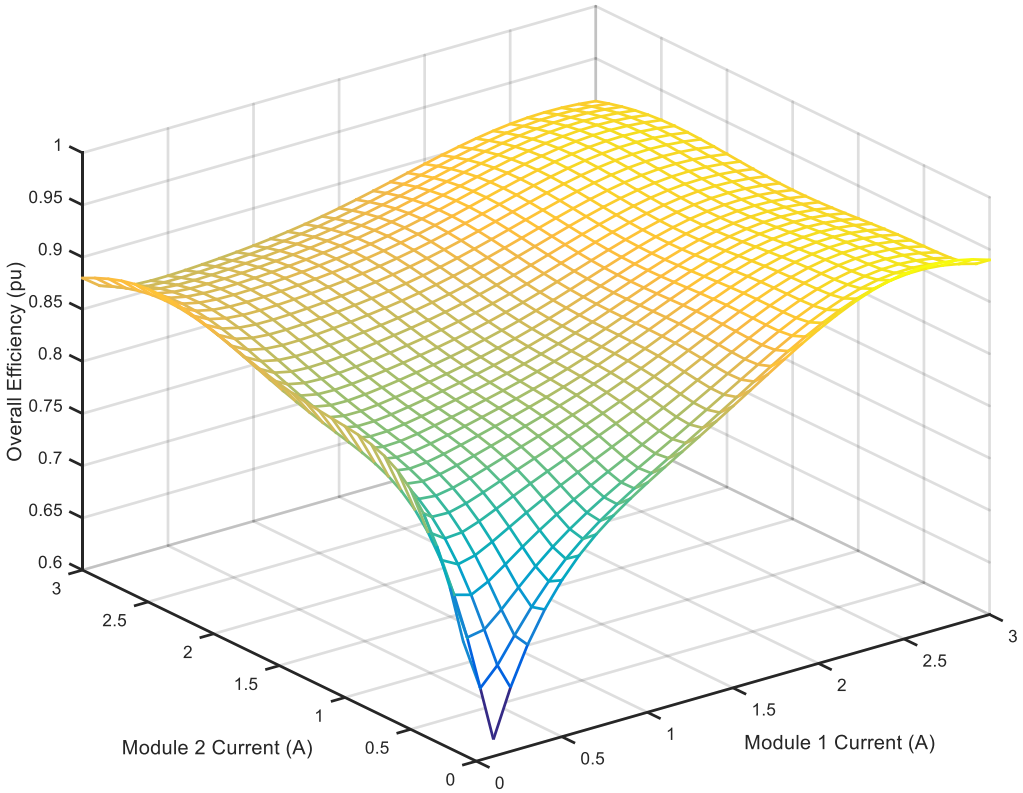

Figure 4.12. Surface plot representing the overall efficiency in G2V mode

Optimization algorithm is implemented with C-block in PLECS using line search method which is a narrowed down version of brute force method using the constraints of the optimization algorithm. Since the number of modules in the simulation is two, using line search method for the optimization is easier and cost effective to implement. If number of modules are increased a more generalized optimization algorithm can be used. To visualize the optimization algorithm, a flowchart is built and in this flowchart *x1* and *x2* and are used as temporary variables for module 1 and module 2 replacing the reference variables of each module *p1* and *p2* or *i1* and *i2*. Throughout the algorithm number suffixes will represent the module numbers. *xRef1* and *xRef2* are the final reference commands, *maxEffPoint* represents the maximum overall efficiency at given condition, *demand* is the current grid power or charging current demand, *f(x1,x2)* is the surface function for the overall efficiency of the whole system and *ratedV* is the maximum grid power or charging current that can be supplied by a charger module. Flowchart of the optimization algorithm is given in Figure 4.13.

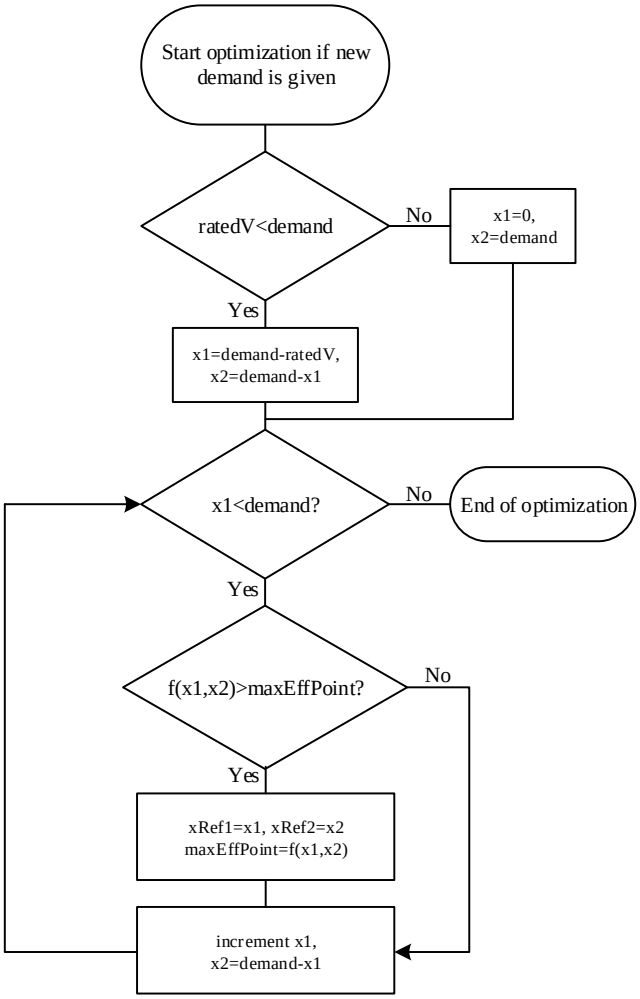

Figure 4.13. Flowchart of optimization algorithm

The operation of the optimization algorithm can be explained as follows. When a new demand is given, optimization algorithm is started. Then, according to the demand, starting value of the first reference is initiated. For example, if the *ratedV* of each module is 600 and the *demand* received is 500, *x1* is set to 0 and *x2* is set to 500. However, if *demand* is 800, it exceeds the *ratedV* of the modules. In that case, *x1* is set to 200 and *x2* is set to 600. Once this initialization is done, algorithm starts inserting *x1* and *x2* values into surface function, and compares the values in each loop to determine the *maxEffPoint*. Each time *maxEffPoint* is found, the reference values are updated with the current values of *x1* and *x2*. The algorithm stops when tracing of all the values is finished. At the end of the algorithm *maxEffPoint* variable holds the value of the maximum efficiency that can be reached at given condition, and *xRef1* and *xRef2* hold the necessary reference values to reach that efficiency.

4.2.2 Optimized Sharing Simulation Results

At first, simulation results are gathered for both V2G and G2V operating modes for equal current sharing and then for optimized current sharing. Circuit elements of the simulation model are built nearly ideal and thus it is hard to determine the exact overall efficiency from the simulation. That is why the overall efficiency of the system is derived from the surface function of the overall efficiency for each discrete reference grid power of charge current.

There are four simulation scenarios in total; equal current sharing in V2G mode and G2V mode, and optimized current sharing in V2G mode and G2V mode. Reference values with corresponding time steps are given in Table 4.3.

Table 4.3. Modular system simulation references

Time Step (s)	Charge Current Demand (A)	Grid Power Demand (W)
0.5	1	200
1	2	400
1.5	3	600
2	4	800
2.5	5	1000
3	6	1200

In equal current sharing mode, the modules will be loaded equally for all demand values. In optimized current sharing mode, when the demands are changed at given times, the master controller will run optimization algorithm and determine the new charge current or grid power command values for each individual module. Figure 4.14 shows the charge current

commands for each module when the system is operated in G2V optimized current sharing mode. The dynamic current sharing for each module while keeping the total current equal to the demanded charge current can be easily seen from the figure.

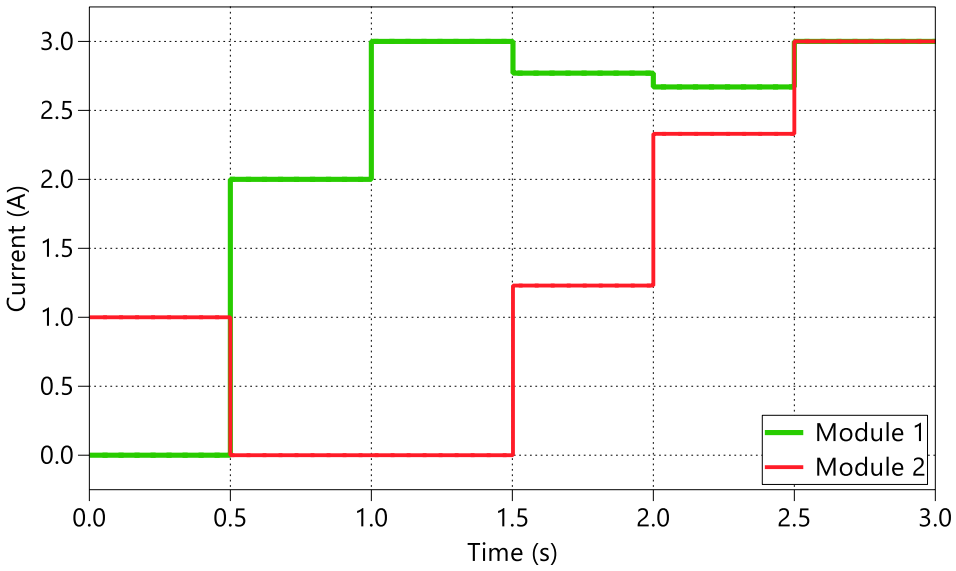

Figure 4.14. G2V mode optimized current sharing

The overall system efficiency for each demanded current can easily be calculated from overall efficiency surface function by inserting the operating currents of the individual modules for each time section. The overall efficiency curves for optimized current sharing and equal current sharing modes are obtained by using this method. Comparison of both modes is depicted in Figure 4.15. Efficiency increase from light loads to middle loads can easily be seen from the graph. The currents of the modules approach each other at near full load and that is why there is almost no difference in efficiency near full load.

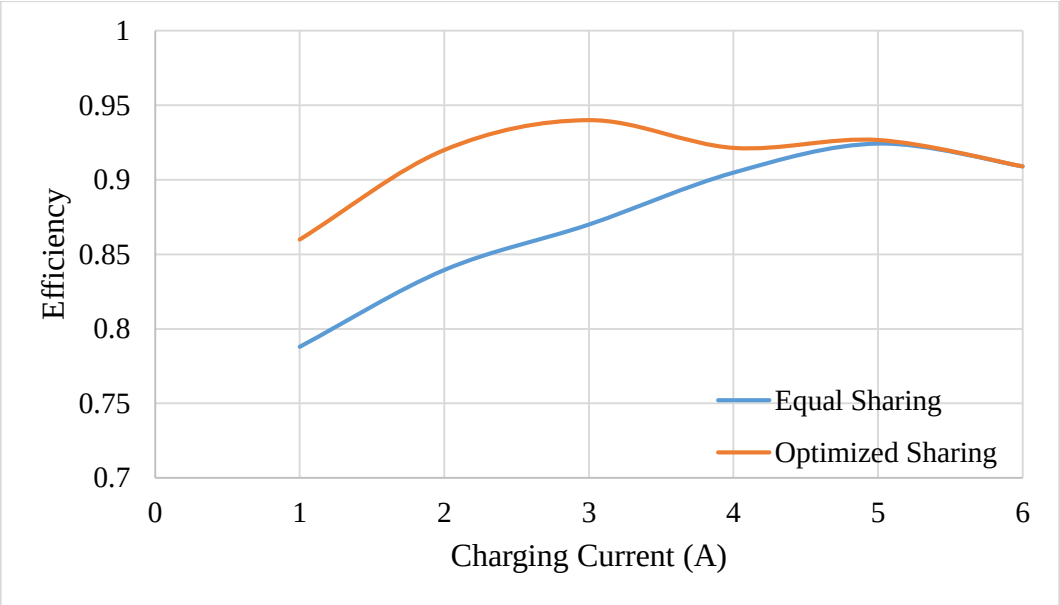

Figure 4.15. Efficiency comparison of equal and optimized current sharing methods in G2V mode

The same approach is also applied for V2G mode. The master controller gets grid power demand as given in Table 4.3 and the resulting power sharing is depicted in Figure 4.16. The dynamic sharing resembles that of G2V mode and chargers almost share equally when close to full power. Comparison of equal sharing and optimized sharing is given in Figure 4.17. Again the benefits of the proposed system can easily be seen at light to middle loads.

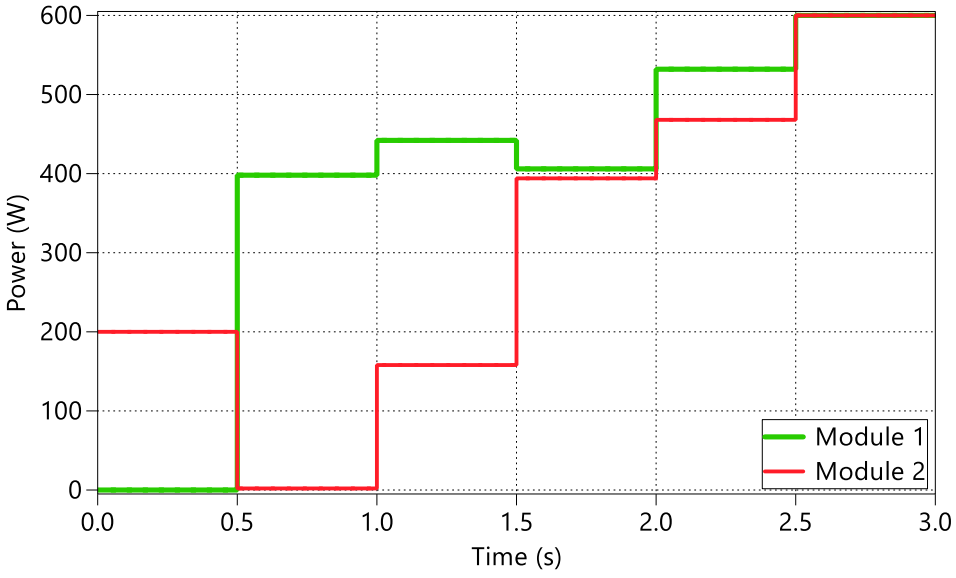

Figure 4.16. V2G mode optimized current sharing

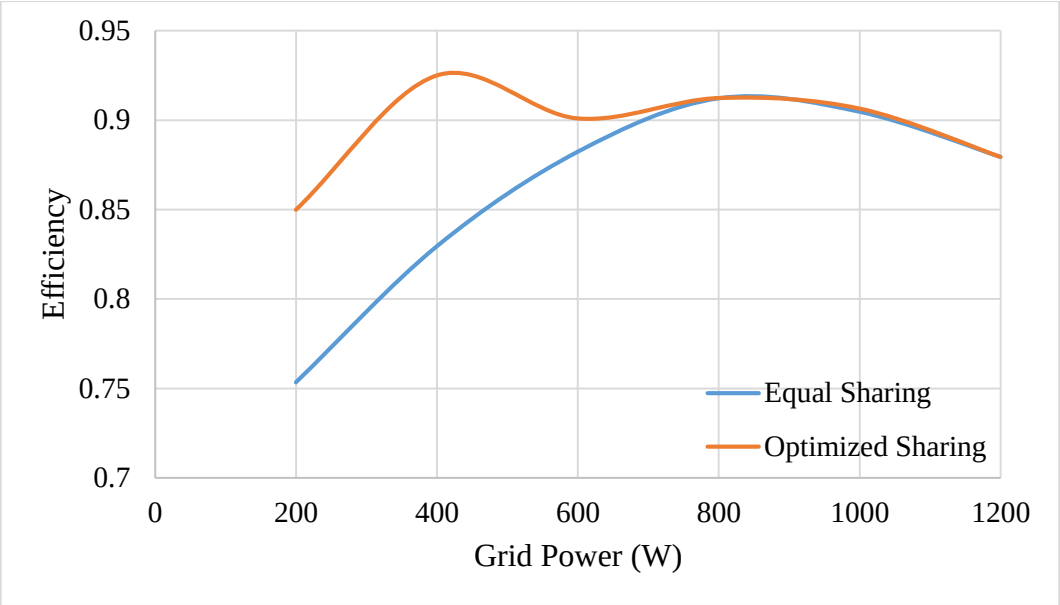

Figure 4.17. Efficiency comparison of equal and optimized current sharing methods in V2G mode

Simulation results align with the aim of this study and confirm the operation of the optimization method to improve the overall efficiency of a EV charger system through modular system design approach. Next chapter will focus on hardware implementation.

5. HARDWARE DESIGN AND EXPERIMENTAL RESULTS

In this section details on hardware design of the charger modules and the experimental results of the working prototypes will be shared. First, specifications of system will be elaborated and the block diagram of a module will be given. Second, further details on hardware sub modules will be shared. Last, experimental results of the working prototypes will be shared. The benefits of the proposed optimizer algorithm will be clearly depicted by comparing the load/efficiency curves of the equal current sharing mode and optimized current sharing mode.

5.1 Specifications of the Hardware Prototype

For modular operation, there must be more than one charger module. Due to price, only one digital signal controller could be purchased, and the peripheral units of a one controller is only sufficient to build two prototypes. That is why modular operation will be verified with two modules as it is done in simulations. From here on, the charger modules built for the study will be referred as Module 1 and Module 2.

Hardware implementation of a bidirectional charger system requires three key elements. First, a power stage, which will process AC or DC power appropriately to transfer power in each direction. Second, proper sensing circuitry with appropriate resolution and response time to make the control of the power stage stable. Last, a control block which can be implemented using a digital signal processor which will process the information gathered from sensing circuitry to apply necessary PWM signals to the power stage semiconductors.

Block diagram of the designed charger module prototype is given in Figure 5.1. Low pass filters at the AC and DC sides are crucial for filtering out high frequency switching ripples. Auxiliary supplies are necessary for signal conditioning and gate drive circuitries. Other blocks were discussed in previous chapter; thus it will not be repeated here. Next section will give detailed information on the workings of the hardware prototype by explaining the sub modules.

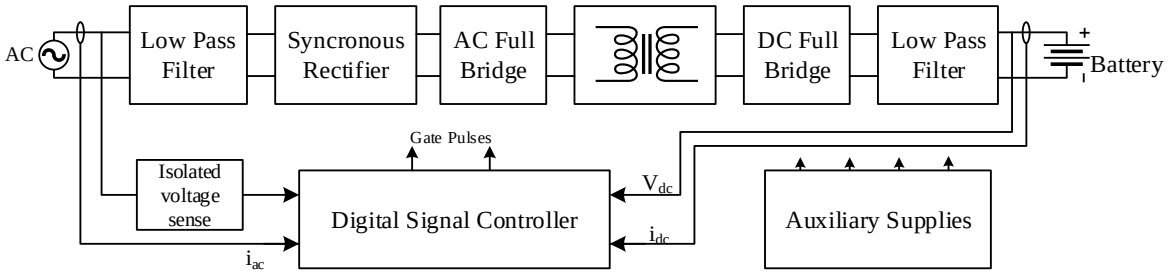

Figure 5.1. Block diagram of the hardware prototype

The specifications of the system is given in Table 5.1. Battery voltage is given approximately because it will change as the batteries are charged and discharged. Details on battery pack system will be given in further sections.

Table 5.1. Specifications of hardware prototype

Grid Voltage/Frequency	220 Vrms/50Hz
Battery Voltage	~200 V
Transformer Turns Ratio	3:1
Leakage Inductance	15 µH
Switching Frequency	25 kHz
Rated Grid Power	600 W
Rated Charging Current	3 A

5.2 Implementation of Hardware Prototype

Two identical hardware prototypes are built which uses the same controller. In this section building blocks of one prototype will be demonstrated and details on the construction of its building blocks will be shared.

5.2.1 Magnetic Elements

AC side low pass filter is comprised of classical L and C components. The MOSFETs in the hardware system is also switched at 25 kHz, thus a filter whose cut-off frequency is one tenth of the switching frequency would be sufficient to filter out most of the switching ripple. L and C values are determined considering the reactive power that is consumed by the capacitor component of the filter. At full power of 600 W and at rated operating voltage of 220 Vrms, for a power factor (PF) of 0.98, total apparent power can be calculated as,

$$P = PF \cdot S \tag{5.1}$$

S equals to 612.24 VA. Below, reactive power can be found as 121.83 VAR.

$$Q = \sqrt{S^2 - P^2} \tag{5.2}$$

Since the impedance of an inductance linearly increases with the frequency, at 50 Hz its reactive power consumption can be ignored. Almost all the reactive power will be consumed by the capacitor. Using reactive power value calculated from (5.2), required capacitor value can be found as follows.

$$C = \frac{Q}{V^2 \cdot 2 \cdot \pi \cdot 50} \tag{5.3}$$

Where V is rms value of AC voltage. Using this equation capacitor value is found as 8.01 µF. 4 capacitors of 2.2 µF standard value can be used in parallel to reasonably approach the calculated value. Then the filter inductor value should be found by using the cut-off frequency f_c. This can be expressed as follows;

$$L = \frac{1}{4 \cdot \pi^2 \cdot {f_c}^2 \cdot C} \tag{5.4}$$

By setting the cut-off frequency to 2.5 kHz and the capacitor value 8.8 µF as stated before, L value is found as 461 µH. For this inductor, core is selected as 77930A7 from Koolµ series from Magnetics Inc. Its permeability is 125µ and A_L value is 157 ±8% nH/T^2. Considering the worst case scenario, A_L value is chosen at the lower boundary which is 144.44 nH/T^2. For an L value of 461 µH, number of turns can be calculated from the following equation.

$$N = \sqrt{\frac{\mathrm{L}}{\mathrm{A}_L}} \tag{5.5}$$

Using the aforementioned values, N is calculated as 56.43, and since the number of turns must be an integer, it is truncated to 56 turns. Inductor is wound with 1.2mm diameter enameled copper wire. Its inductance is measured to be 506 µH.

DC side low pass filter comprises of C-L-C structure. DC switching network of the charger module applies high frequency voltage pulses and to minimize voltage ripple a large amount of capacitor should be used right after DC full bridge to act as a low impedance source. Then the switching ripple in the current can be filtered by using a standard LC filter. This configuration is depicted in Figure 5.2.

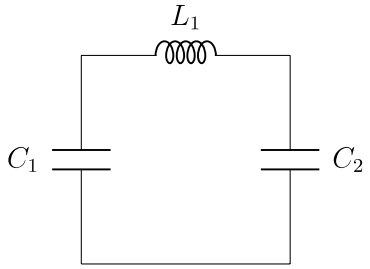

Figure 5.2. DC side C-L-C filter

C_1 value is selected as 35 µF and to reach this value 16 pieces of 2.2 µF low equivalent series resistance (ESR) ceramic capacitors are used. Since some of the ripple will be filtered with C_1 the cut-off frequency of the LC filter is chosen one fifth of the switching frequency which is 5 kHz. Reactive power is not a concern for DC side. That is why L_1 and C_2 values are

found iteratively through simulations. L_1 value is set to 80 μH and C_2 value is found as 13 μF. Filter inductor is wound on the same core as AC filter inductor, which is 77930A7 from Magnetics Inc., with 1,2 mm enameled copper wire. For the specified inductance value required number of turns is found from equation (5.5) as 23.53 which is rounded to 24. Inductance of the constructed inductor is measured to be 94.8 μH. For the filter capacitor 6 pieces of 2.2 μF ceramic capacitors are used.

In physical hardware implementation, a tightly coupled nearly ideal transformer with a discrete inductance to model the leakage inductance approach is followed. Design of isolation transformer and the leakage inductance is the most important among all magnetic elements of the charger. Isolation transformer transfers power between either side and leakage inductance makes the desired power conversion possible.

Transformer coupling should be maximized in order to increase the power transmission efficiency. That way energy storage in the transformer will be minimized. For future scalability a bigger core than required is chosen for isolation transformer. An ungapped core with N97 material and ETD54 package is more than sufficient for the requirements of the design. Since the applied voltage to the primary of the transformer is essentially square wave within a sinusoidal envelope, following relationship is used for calculating the number of turns in the AC side, where $V_{AC,peak}$ is the peak value of the AC voltage, f_{sw} is the switching frequency, B is the flux density of the magnetic core, A_c is the core area and N_{pri} is the number of primary windings.

$$V_{AC,peak} = 2 \cdot \pi \cdot f_{sw} \cdot B \cdot A_c \cdot N_{pri} \tag{5.6}$$

$V_{AC,peak}$ is 324 V, f_{sw} is 25 kHz, A_c is 280 mm^2 for ETD54 core, and B is selected as 0.15 T for moderate core losses. By inserting these values to the equation, N_{pri} is found as 49.1 and it is rounded to 50. Turns ratio is specified as 1/3 and this translates to 17 turns for the secondary.

Winding design of the transformer is important to reduce copper losses and increase the coupling as much as possible. To reduce AC losses stranded wire construction is preferred where the diameter of individual strands is equal or lower than skin depth of copper at the frequency of the current. Skin depth of copper at 25 kHz is 0.41 mm. However, since multiple-strand wires can carry less current than single-strand wires at the same diameter, due to air gap between individual strands; winding window of the coil former is not adequate

if the transformer is wound with the wire with the required number of strands for the rated current where diameter of each strand is 0.41mm or less. That is why primary winding of the transformer is wound by using 6 strands of 0.5 mm diameter enameled copper wire. The current in the secondary will be three times that of flowing in the primary, thus secondary winding is wound with 20 strands of 0.5 mm diameter enameled copper wire. To decrease the AC losses due to the proximity effect and increase the coupling between the primary and secondary windings, interleaved winding structure is utilized in the transformer winding structure. Half of the primary winding is wound first, and secondary winding is wound on top of that followed by the remaining half of the primary winding. No airgap is used between cores to maximize the magnetizing inductance. Final cross sectional winding scheme is depicted in Figure 5.3.

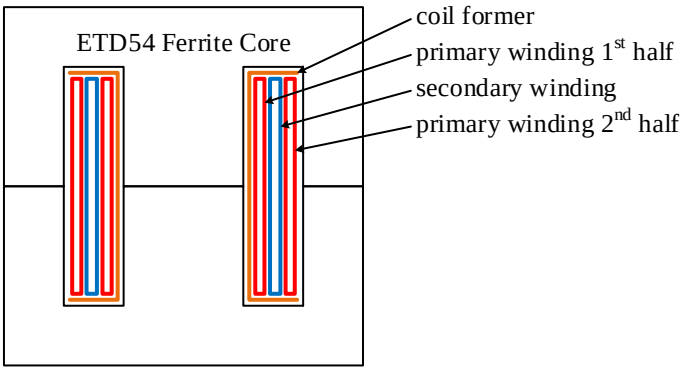

Figure 5.3. Winding scheme of the isolation transformer

Transformer constructed based on specifications and it is shown in Figure 5.4. Winding inductances are measured as 12.8 mH for the primary and 1.47 mH for the secondary. Secondary leakage inductance is measured as 4.2 μH which is an indication of tight coupling between windings.

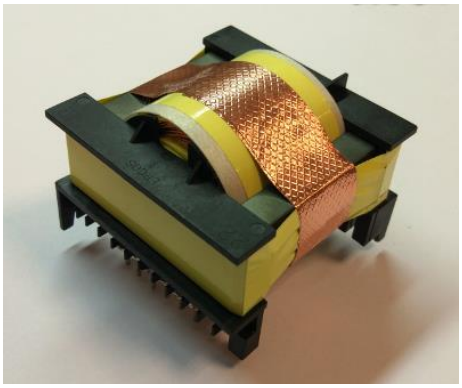

Figure 5.4. Constructed isolation transformer

External leakage inductor will be designed considering energy storage and core losses. Since the current flowing in the secondary will be very high, the core used for the inductor must not saturate and the flux swing should not be very high to increase core losses. That is why a core manufactured from a low permeability, distributed airgap material is chosen for the application. Core is made from MPP material from Magnetics Inc. and its part number is 55550A2. It has low permeability at 26 μ, and presents low core losses. Using (5.5) required number turns can be calculated. A_L value of 55550A2 is 28±8% nH/T^2, and for the specified 15 μH of inductance, required number of turns is 24. The current flowing through inductor and transformer secondary is identical. Thus, 20 strands of 0.5 mm diameter wire that is used in transformer secondary will be used here as well. However, during the mechanical construction of the inductor it was realized that winding window cannot accommodate the calculated number of turns; thus number of turns had to be decreased to 22. Resulting inductance is measured as 14.50 μH. The final look of the inductor is given in Figure 5.5.

Figure 5.5. Leakage inductor

5.2.2 Digital Controller Unit

Designed charger requires a smart controller block to orchestrate the operation of semiconductor switches to perform power conversion, to be able to get grid power and charge current demands and apply optimization algorithm. As a digital controller unit (DCU) of the charger, TMS320F28335 is used from Texas Instruments. To alleviate another design challenge, eZdsp evaluation board with on-board debugger and MCU swappable holder from Spectrum Digital is selected. DCU is shown in Figure 5.6. The specifications of the controller are given in Table 5.2.

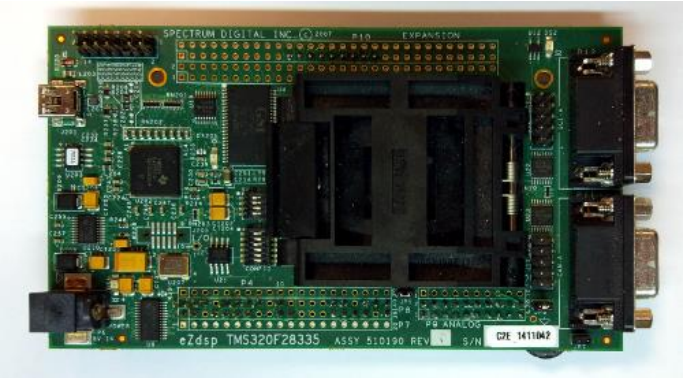

Figure 5.6. Digital controller unit

Table 5.2. Specifications of digital controller unit

Central Processing Unit (CPU)	TMS320C28x series CPU operating at 150 MHz
Clock and System Control	• On-Chip Oscillator • Dynamic PLL Ratio Changes Supported • Watchdog Timer • Three 32-bit Timers
Memory	• 256K × 16 Flash • 34K × 16 SARAM • 8K × 16 Boot ROM
Enhanced Control Peripherals	• 12 PWM Outputs • Six Event Capture Inputs • Two Quadrature Encoder Interfaces
Analog-to-Digital Converter (ADC)	• 12-bit resolution • Two Sample and Hold • 12,5 MSPS Throughput
General Purpose Input/Output (GPIO)	88 Multiplexed GPIO Pins With Input Filtering
Serial Port Peripherals	• One Inter-Integrated-Circuit Bus • One Serial Peripheral Interface • Three Universal Asynchronous Receiver/Transmitter Modules

Digital control ground is referenced to DC side ground of the charger. That is why voltage and current measurements from AC side are obtained in an isolated fashion. Control algorithm running in the DCU makes use of the voltage and current measurements taken from both AC and DC side and calculates the duty cycle of the DC side switches cycle-by-cycle. Since the DCU is used to control two charger modules simultaneously, the voltage and current measurements should be read from different ADC channels. To achieve this with identical charger modules, outputs of voltage and current transducers are routed to two different ADC channels in a double pole single throw switch like manner.

Enhanced pulse width modulation (EPWM) units in the DCU are used to drive semiconductor switches. AC side switches are driven by complementary signals with 50% duty cycle, so that is why just one EPWM unit with two outputs is sufficient to drive AC

side switches in both modules. However, DC side switches require complex gate drive signals for the system to operate properly, and because of that two independent EPWM units with four PWM outputs in total are dedicated to each DC full bridge for both charger modules. In total five EPWM units of the DCU are utilized for the control of semiconductor switches. EPWM5 is dedicated to AC side switches of the both charger modules, EPWM1 and EPWM3 are dedicated to DC side switches of the Module 1 and EPWM2 and EPWM4 are dedicated to the Module 2.

Time base counters of the EPWM units are counting at the operating frequency of the DCU, which is 150 MHz. For 25 kHz switching frequency, this translates to a time base period value of 6000. Also all the time base counters are synchronized with each other to start counting at the same time. Compare A (CMPA) and Compare B (CMPB) registers in EPWM units are used to achieve various PWM outputs. For EPWM1 and EPWM3 outputs, dead band module in the DCU is utilized to achieve precise dead band control. Dead band for AC side gate drive signals are achieved with integrated dead band control of the gate drive circuits. Time base counter and PWM adjusting scheme is clearly illustrated with color coded symbols in Figure 5.7 for Module 1.

CMPA and CMPB values of EPWM1 and EPWM3 are calculated cycle-by-cycle based on the available information on AC and DC voltage levels. Closed loop control algorithm determines the phase-shift for the desired grid power or charging current. Necessary precautions are taken to ensure stable operation of the control algorithm; for example, by saturating the output of closed loop control algorithm not to exceed the maximum phase shift value.

To calculate real, reactive and apparent power of the AC side, a square wave synchronized with the zero crossings of AC voltage is fed through a GPIO pin of the DCU. GPIO input filtering is utilized to get rid of the possible high frequency noise and jitter from the input signal. Moreover, necessary algorithms are developed for calculating root mean squares of voltage and current values.

Input and output current values of both chargers are used for protection purposes in overcurrent events. To achieve this purpose a gate driver module is selected with an external enable/disable pin. When either current of the charger exceeds the pre-specified threshold value, overcurrent flag is set and the gate driver modules are disabled through this

enable/disable pin via GPIO pins of the DCU. Overcurrent flag is not cleared and gate drivers are not enabled until charger is reset externally.

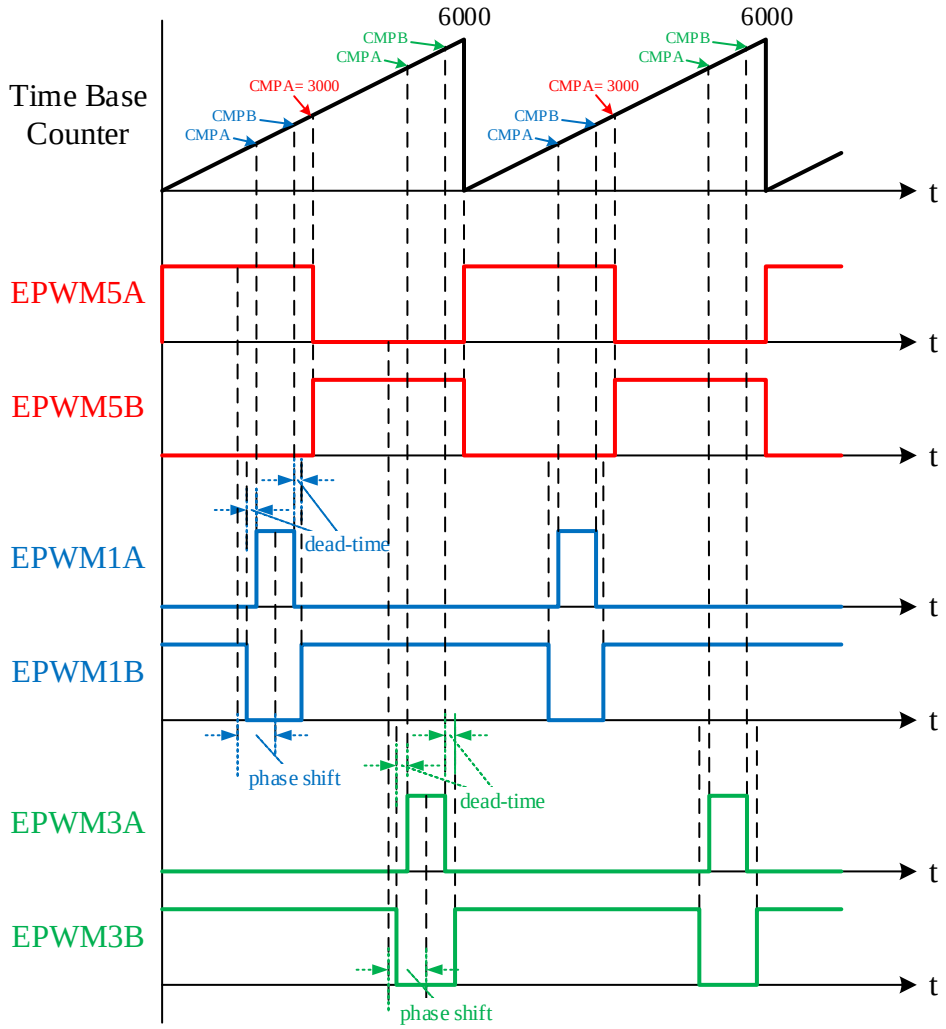

Figure 5.7. EPWM scheme utilized in the DCU

5.2.3 Auxiliary Supplies

Any power electronic circuit needs auxiliary supplies for the signal and gate drive circuitries to operate. AC side of the circuitry requires one auxiliary supply for gate drive and other signal conditioning circuits. On the other hand, DC side of the charger requires three isolated supplies in total, where one of them is for the signal conditioning and low side gate drive circuitry and remaining supplies are used for the gate drive circuit of the high side MOSFETs. A multi output flyback converter is designed for this purpose. Flyback converter is chosen because it is relatively easy to acquire multiple outputs and it offers galvanic isolation.

Flyback converter is supplied from the battery side of the charger with constant DC voltage. An integrated flyback MOSFET and error amplifier solution, TOP244YN from Power

Integrations is used in the design. For the flyback transformer design, E25 core is chosen according to the manufacturer's design suggestion for the required power level. Flyback converter can only regulate one output with the closed loop control and precise regulation cannot be achieved for other output without special attention. When one output is regulated precisely, the other outputs can be roughly regulated using the ratio of number of windings of corresponding outputs. For example, if closed loop control is realized according to a +12 V output and the number of windings of that output is 12, a second output with roughly +15 V regulation can be achieved with number of windings at 15. However, when the current drawn from 12 V output is increased, duty cycle of the converter will also increase to keep +12 V output constant and this will cause an increase in +15 V output.

Designed charger requires four auxiliary supplies in total. And since none of the gate drive voltage require precise regulation, rough regulation method can be utilized for the other outputs. And when precise regulation is required, linear regulators can be used if the current requirement is considerably small to ignore the low efficiency of linear regulators. First output is +12 V for the low side semiconductor switches gate drive supply and the signal conditioning circuitry of the DC side. Second and third outputs are used for isolated gate drive supply voltages for high side switches of DC side. These outputs are roughly regulated at +15 V. Fourth output is used at the AC side, for signal conditioning and gate drive supplies. This output is also roughly regulated at +15 V. Although DC side switches do not require isolated gate drives, same isolated gate drive circuit is used for both AC and DC side switches for design simplicity. Gate drive circuit requires a well regulated +5 V in its primary side, and this side of the circuit is referenced to DC side of the charger. A linear regulator is used to acquire +5 V from +12 V output of the flyback converter, because current requirement of gate drive circuit for this operation is very small.

5.2.4 Semiconductor Switches

Silicon MOSFETs are utilized for all main semiconductor switches in the charger module. Since synchronous rectifier circuit operates at the line frequency, switching losses can be neglected for this circuit. Conduction losses will be a significant factor for determining the suitable MOSFET for this part of the charger. That is why a low $R_{ds,on}$ MOSFET should be selected. AC side and DC side switches are operated high frequency, but thanks to soft switching technique utilized in the control of the charger, switching losses for these switches are also mostly eliminated and conduction losses will be the dominating factor. This is especially true for the DC side switches, since the current flowing in DC side switches is

three times that in AC side switches and the power loss is directly proportional to the square of current. That is why IPW60R045CP with $R_{ds,on}$ of only 45 mΩ is selected to be used in all active power switches. The important specifications of this MOSFET is given in Table 5.3.

Table 5.3. Specifications of the first selected MOSFET

Part Number	IPW60R045CP
Breakdown Voltage	650 V
Continuous Drain Current	60 A
Drain-Source On Resistance	0.045 Ω (Max)
Gate Charge	190 nC (Max)
Input Capacitance	6800 pF
Output Capacitance	820 pF
Intrinsic Body Diode Forward Drop	0.9 V

However, during the initial experimentation phase of the first charger module, it is noticed that the selected MOSFETs caused oscillations during switching on, in AC and DC full bridges. These oscillations are carried through the ground plane via conductive path and possibly via radiating path through the air and caused instabilities in operation of the DCU. The causes of the oscillations are thought to be fast switching of the MOSFET and designer's lack of experience to take necessary precautions in the printed circuit board (PCB) layout. These issues are mitigated with choosing a slower MOSFET and increasing the gate drive resistances to limit the turn on speed of the MOSFET. The trade-off for this decision is the higher $R_{ds,on}$ of the newer MOSFET and most probably lower efficiency for the individual charger. However, since the idea to be verified is the overall efficiency increase in the modular system, the efficiency of the individual modules is not an important factor. The part number of the new MOSFET is IXFH32N50Q and its key specifications are given in Table 5.4.

Table 5.4. Specifications of the second MOSFET

Part Number	IXFH32N50Q
Breakdown Voltage	500 V
Continuous Drain Current	30 A
Drain-Source On Resistance	0.15 Ω (Max)
Gate Charge	190 nC (Max)
Input Capacitance	4925 pF
Output Capacitance	800 pF
Intrinsic Body Diode Forward Drop	1.5 V

While building Module 2, a newer MOSFET is selected for the DC full bridge of the charger to increase its efficiency. Most of the current is flowing in the DC part of the charger and a MOSFET with lower $R_{ds,on}$ can increase the efficiency substantially. The specification of this MOSFET is given in Table 5.5.

Table 5.5. Specifications of the MOSFET used in DC side of Module 2

Part Number	IPP200N25N3
Breakdown Voltage	250 V
Continuous Drain Current	64 A
Drain-Source On Resistance	0.02 Ω (Max)
Gate Charge	86 nC (Max)
Input Capacitance	7100 pF
Output Capacitance	395 pF
Intrinsic Body Diode Forward Drop	1.2 V

5.2.5 Battery Pack

Battery pack for the laboratory experiments are built with lead-acid batteries. The reason for this choice is the wide availability of the lead-acid batteries, price, and easy scalability. Easy scalability refers to the fact that using the lead-acid batteries in series requires no extra hardware, whereas using li-ion batteries in series requires complex battery management hardware to balance each cell, monitor cell voltages and pack temperature for reliable operation. Nominal voltage of the individual batteries is 12 V and their rated capacity is given as 7 Ah. Specifications of the battery pack system is given in Table 5.6.

Table 5.6. Specifications of the battery pack

Number of Batteries	18
Nominal Voltage	216 V
Nominal Capacity	126 Ah
Nominal Capacity	1.4 kWh
Approximate Series Resistance	0.45 Ω
Approximate Weight	37.8 kg

5.2.6 Final Configuration

Final configuration of the hardware prototype is shown in Figure 5.8. Labels clearly identify the sub modules explained in previous sections. Modular system is built with integrating two working prototypes and it is shown in Figure 5.9.

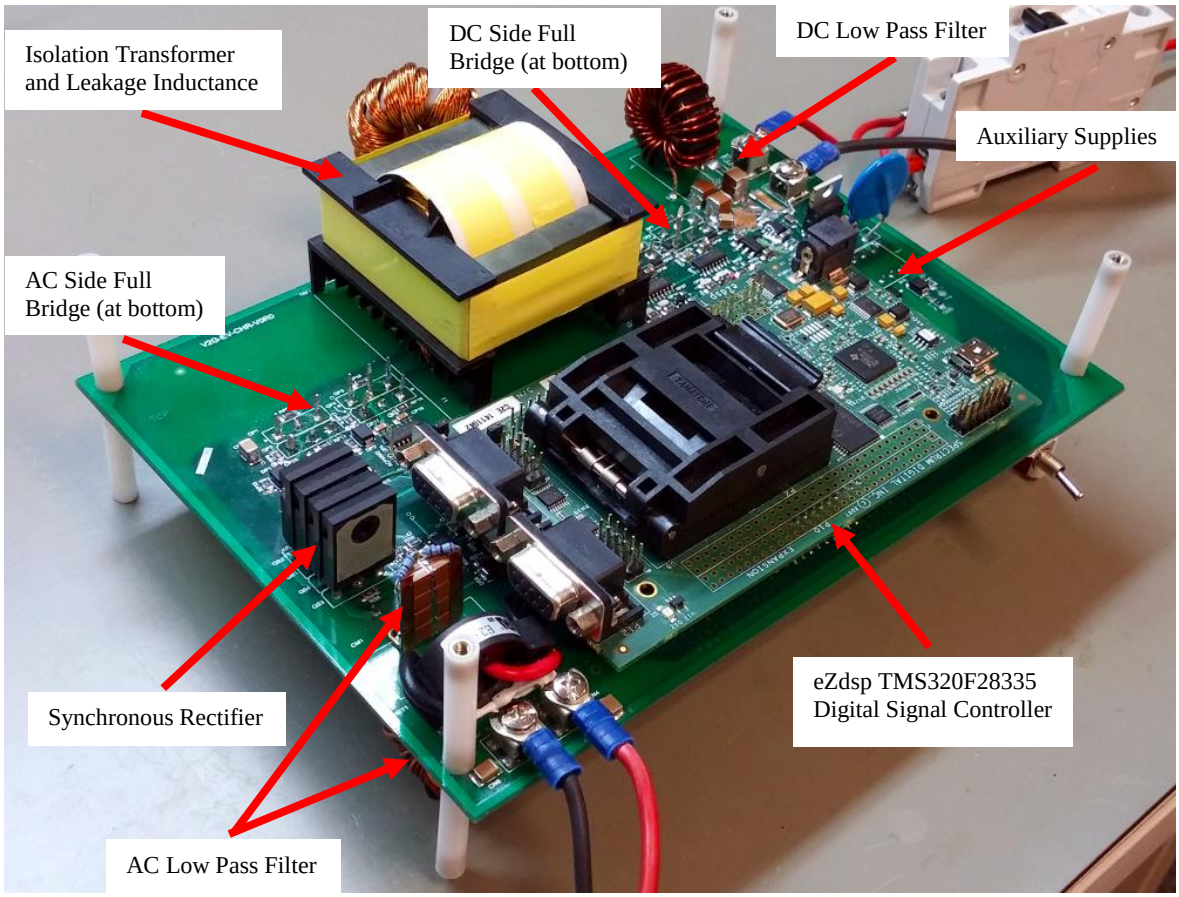

Figure 5.8 First hardware prototype

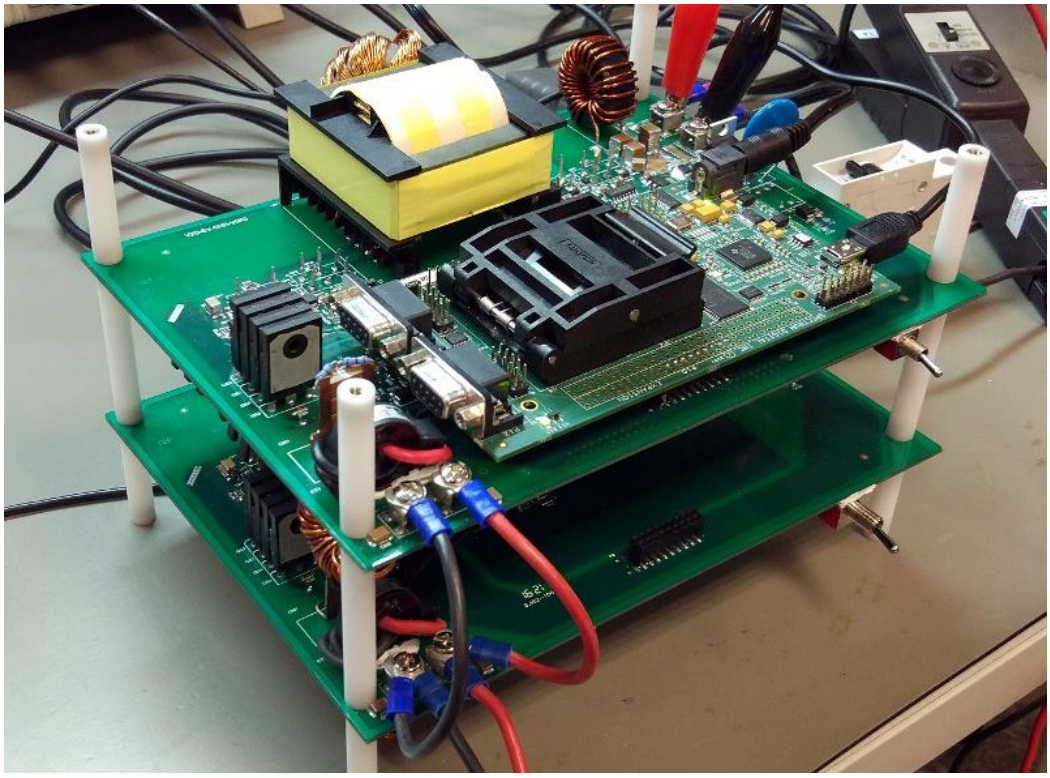

Figure 5.9. Modular system with two individual modules

5.3 Experimental Results

This section will present detailed experimental results via means of waveform plots and efficiency data. Simulation setup is shown in Figure 5.10. During the experimentation phase, an approach that is similar to simulation phase is followed by first verifying the operation of the individual modules and then moving on to the integration phase of the two modules.

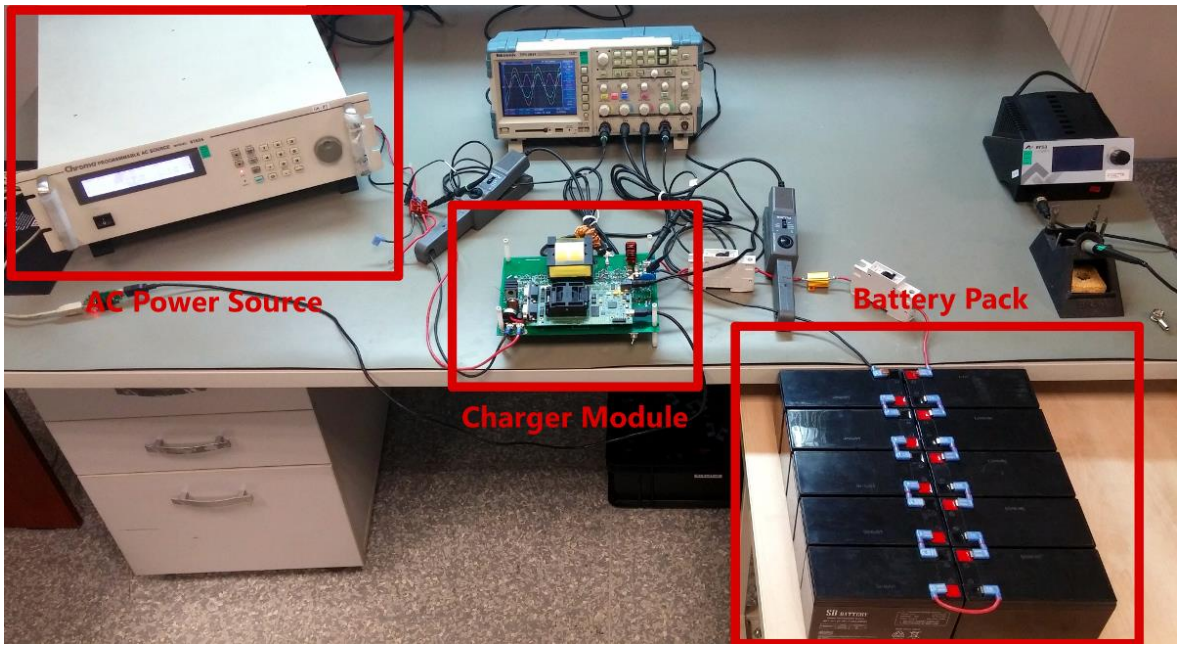

Figure 5.10. Experimental setup

5.3.1 Results of the Steady-State Operation of Chargers

Two modules built from ground-up are tested individually to verify their operation. To achieve this, sub modules are tested one by one and the issues are mitigated one by one and troubleshoot phase of the testing is completed. However, during testing it is decided to operate the chargers at lower voltage and power levels than designed in order not to risk any damage to them. AC voltage level is reduced to 120 V rms, DC voltage level is reduced to approximately 120 V and the power is limited to 300 W. Once the proposed optimization idea for the modular system is verified, power levels of the charger can easily be scaled up for a more meaningful hardware to be integrated in an electric vehicle. The voltage and current waveforms of a working prototype are given in following figures for G2V and V2G modes.

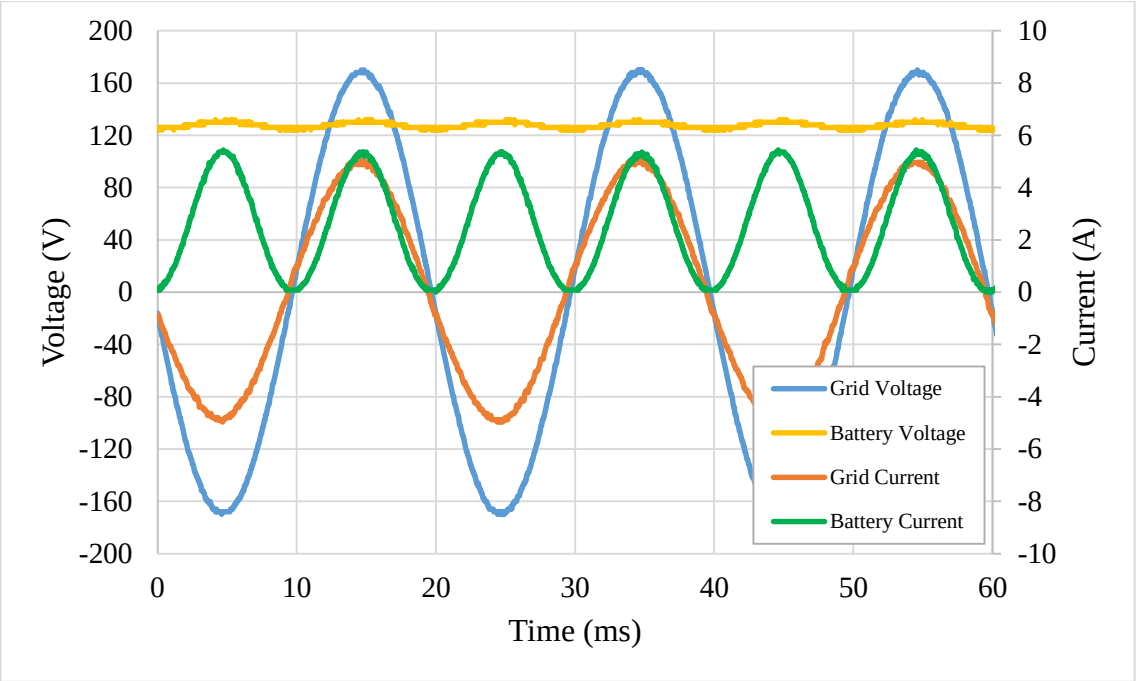

Figure 5.11. Voltage and current waveforms of a working hardware prototype in G2V mode

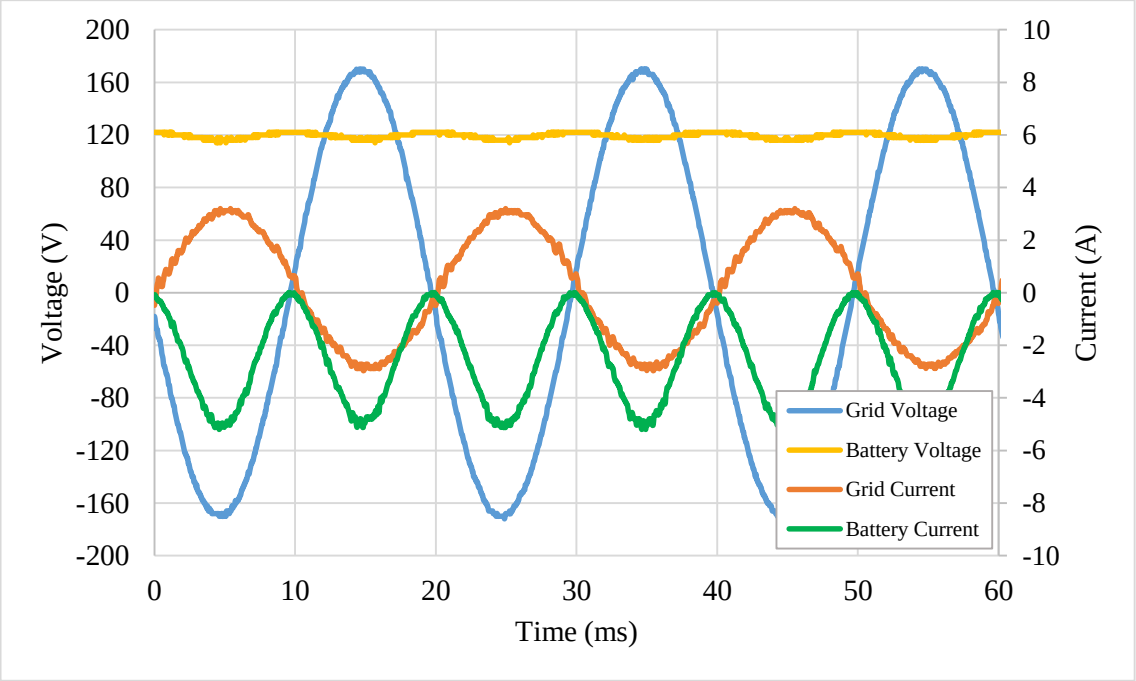

Figure 5.12. Voltage and current waveforms of a working hardware prototype in V2G mode

It is apparent from the figures that the harmonics in the AC current waveform is small and the battery current has sinusoidal ripple. The results are consistent with the results obtained from computer simulations. Power factor is slightly lower than unity due to input low pass filter that is used to attenuate switching ripple. Experimental results for the Module 1 and Module 2 are given in Table 5.7 and Table 5.8.

G2V Mode		V2G Mode	
Grid Voltage	120 Vrms	Grid Voltage	120 Vrms
Grid Frequency	50 Hz	Grid Frequency	50 Hz
Grid Current	3.75 Arms	Grid Current	2.12 Arms
Grid Power	446.4 W	Grid Power	249.8 W
Power Factor	0.992	Power Factor	0.982
THD	1.19 %	THD	2.77 %
Battery Voltage	147.2 V	Battery Voltage	116 V
Battery Current	2.54 A	Battery Current	2.58 A
Battery Power	373.88 W	Battery Power	299.3 W
Efficiency	83.75 %	Efficiency	83.47 %

Table 5.7. Results of the Module 1in G2V and V2G modes

G2V Mode		V2G Mode	
Grid Voltage	120 Vrms	Grid Voltage	120 Vrms
Grid Frequency	50 Hz	Grid Frequency	50 Hz
Grid Current	3.57 Arms	Grid Current	2.54 Arms
Grid Power	427.1 W	Grid Power	299.3 W
Power Factor	0.997	Power Factor	0.982
THD	2.33 %	THD	2.76 %
Battery Voltage	129.6 V	Battery Voltage	113.9 V
Battery Current	3 A	Battery Current	2.95 A
Battery Power	388.8 W	Battery Power	336 W
Efficiency	91.03 %	Efficiency	89.08 %

Table 5.8. Results of the Module 2 in G2V and V2G modes

Also harmonic spectrums of the grid current are given in following figures for both modules in G2V and V2G modes up to 19th harmonic. THD values of Module 1 and Module 2 in both G2V and V2G modes, and the magnitude of the individual harmonics are lower than the limits specified in IEEE 1547 standard [63]. THD limit is 5% and the limits for the individual harmonics are illustrated on the harmonic spectrum figures.

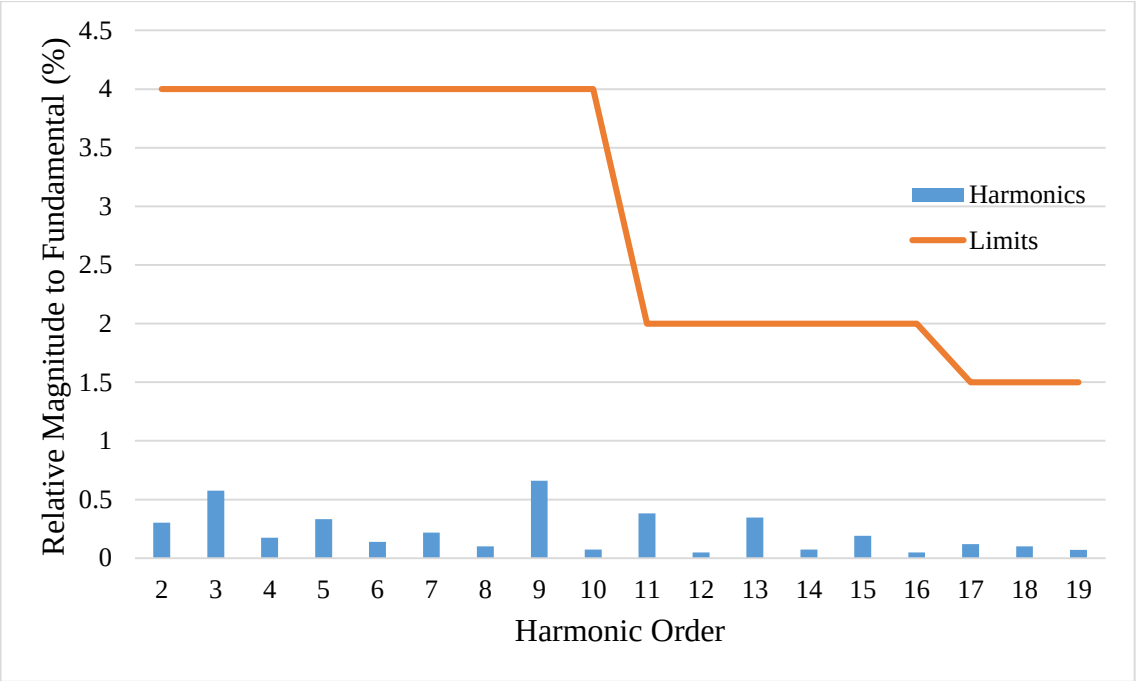

Figure 5.13. Harmonic spectrum of grid current of Module 1 in G2V Mode

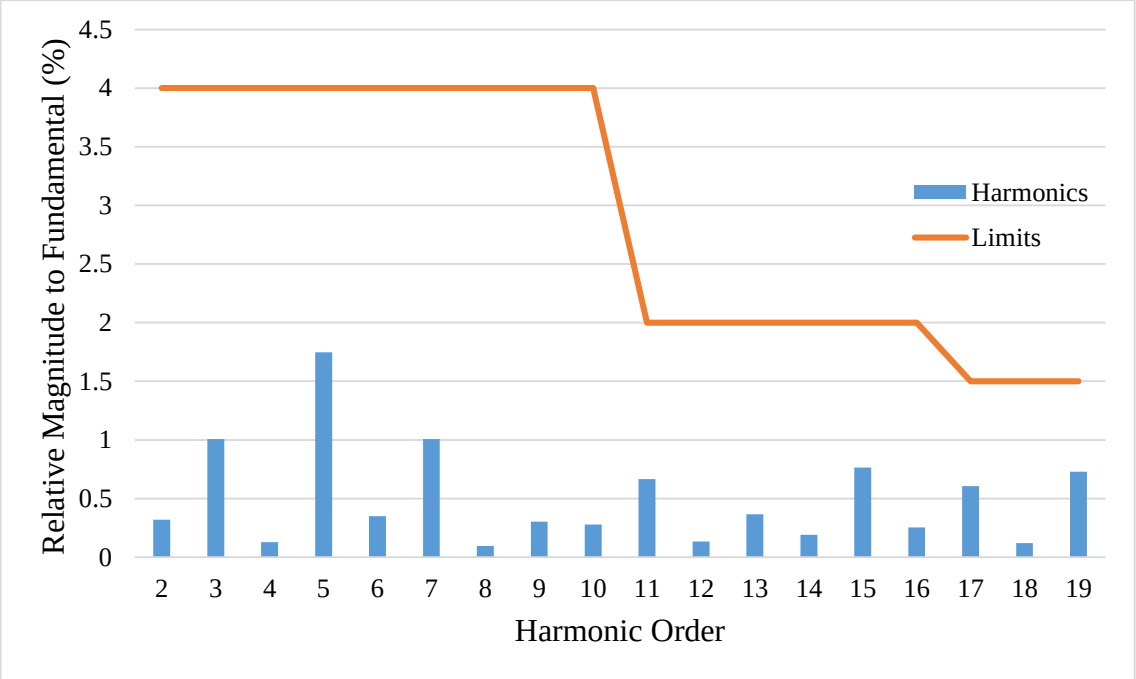

Figure 5.14. Harmonic spectrum of grid current of Module 1 in V2G Mode

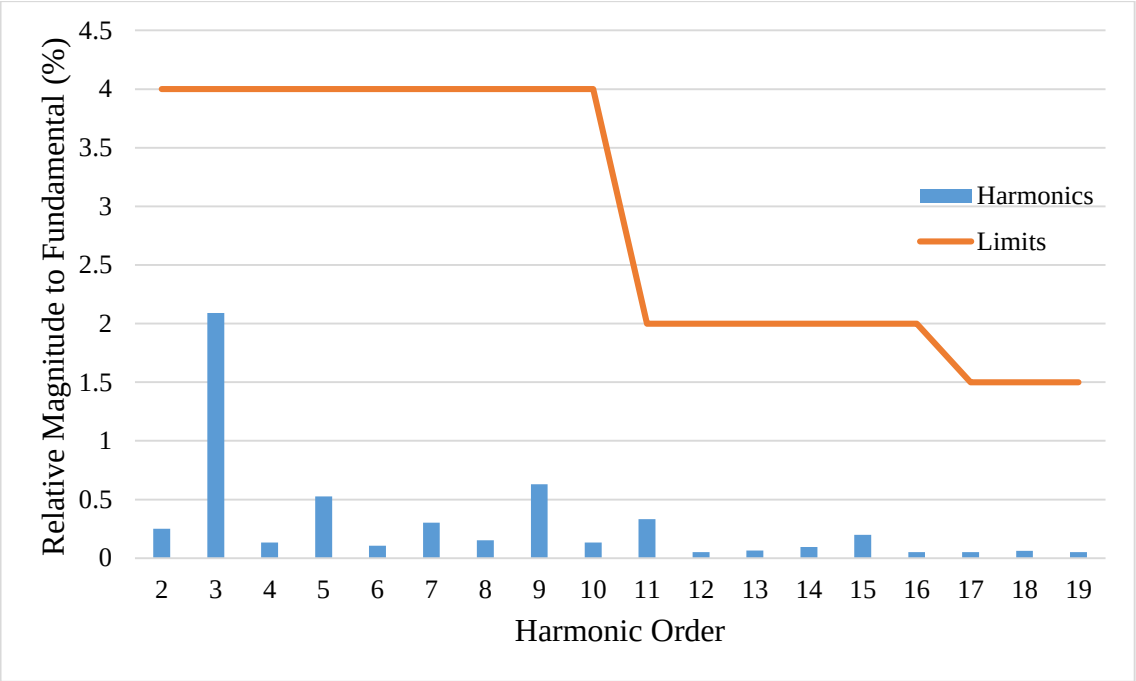

Figure 5.15. Harmonic spectrum of grid current of Module 2 in G2V Mode

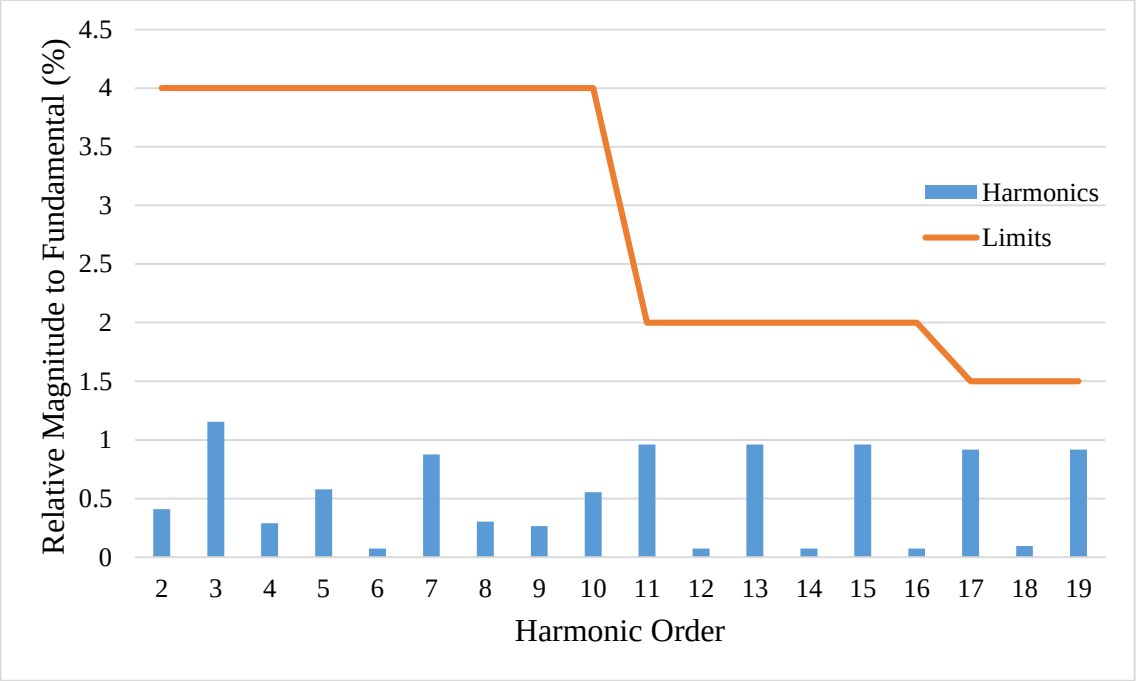

Figure 5.16. Harmonic spectrum of grid current of Module 2 in V2G Mode

5.3.2 Experimental Results for the Optimized Sharing

Verification method for the optimization algorithm is identical to the method that is followed during the computer simulations. First, load/efficiency curves of the individual chargers are plotted. Then, these curves are fitted to polynomials using MATLAB. These functions are loaded into the DCU and they are used in the optimization algorithm to determine charge

current and grid power reference values for the charger modules. The optimization algorithm utilized in the DCU follows the same flowchart given in Figure 4.13.

Module 1 is configured as the master module and Module 2 is configured as the slave module. This is clearly seen in the closed loop controller block diagram given in Figure 5.17, since Module 1 controller includes Optimization and Deciding Algorithm block. In the operation of the closed loop controller, grid voltage is fed to Zero Crossing Detector block to create pulse for each period of the grid voltage. This zero crossing pulse is used in RMS Calculation and Mean Calculation blocks and also gets the frequency information of the grid voltage. RMS Calculation block gets the grid voltage and current information and calculates rms values, these values are multiplied to obtain apparent power of the module. Grid voltage and current values are multiplied sample by sample and fed into Mean Calculation block to calculate the real power of the modules. Charging current of the individual modules are also fed into Mean Calculation block to obtain charging current values of the modules. When real and apparent power are calculated, these values are used to calculate reactive power and power factor of the individual modules. Once the master module gets grid power or charging current demand, it runs the deciding algorithm to activate the necessary PI controllers by turning on the corresponding switches. Then, it runs the optimization algorithm to determine the reference values of the modules for G2V or V2G mode operation. The resulting error signals are fed into PI controllers to calculate the required phase-shift ratio.

Load/efficiency curves of the modules for G2V mode is given in Figure 5.18. It can be seen from the figure that Module 2 has higher overall efficiency throughout all the load conditions. That is because of the newer MOSFET that is used in the DC side of the charger where most of the conduction loss comes from. Figure 5.19 depicts the grid power vs efficiency curves of the modules in V2G mode. Again higher efficiency of the Module 2 is apparent in this figure. Figure 5.20 and Figure 5.21 illustrate the overall efficiency surface function of the hardware system.

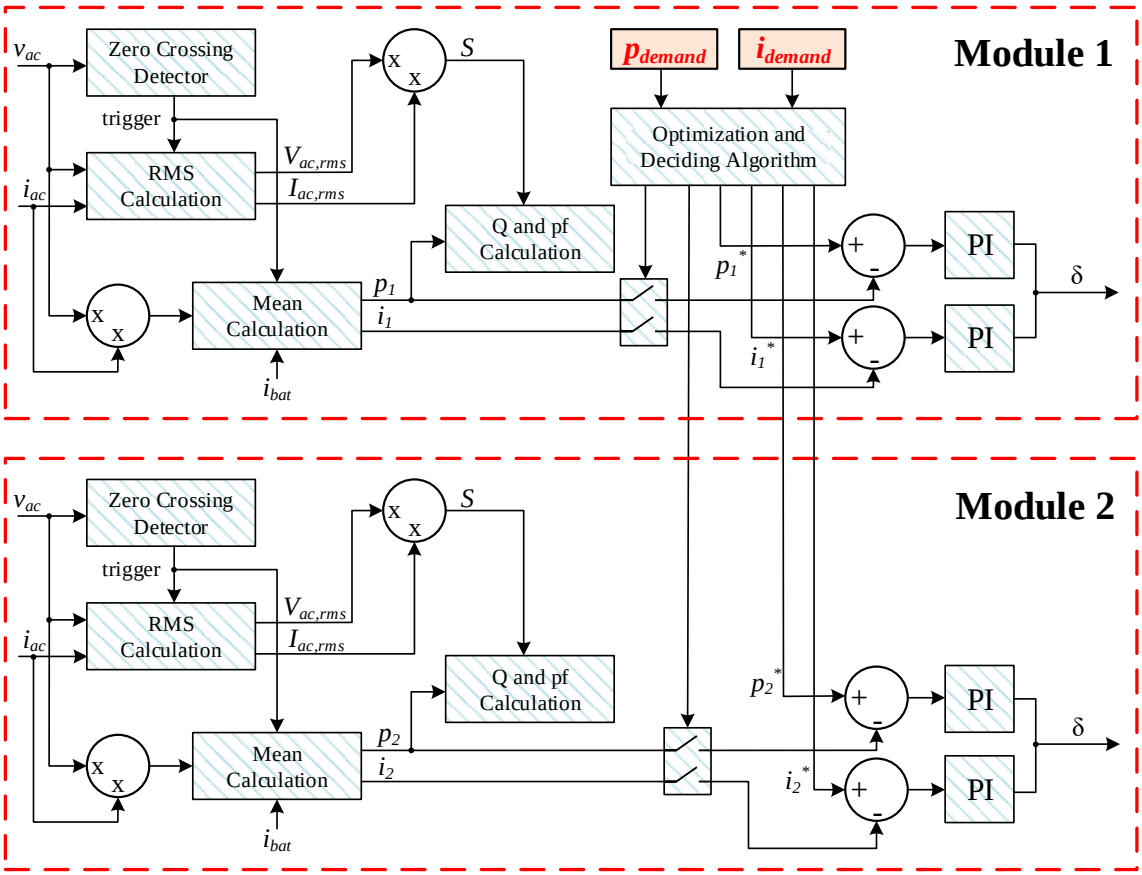

Figure 5.17. Closed loop controller block diagram of the built system

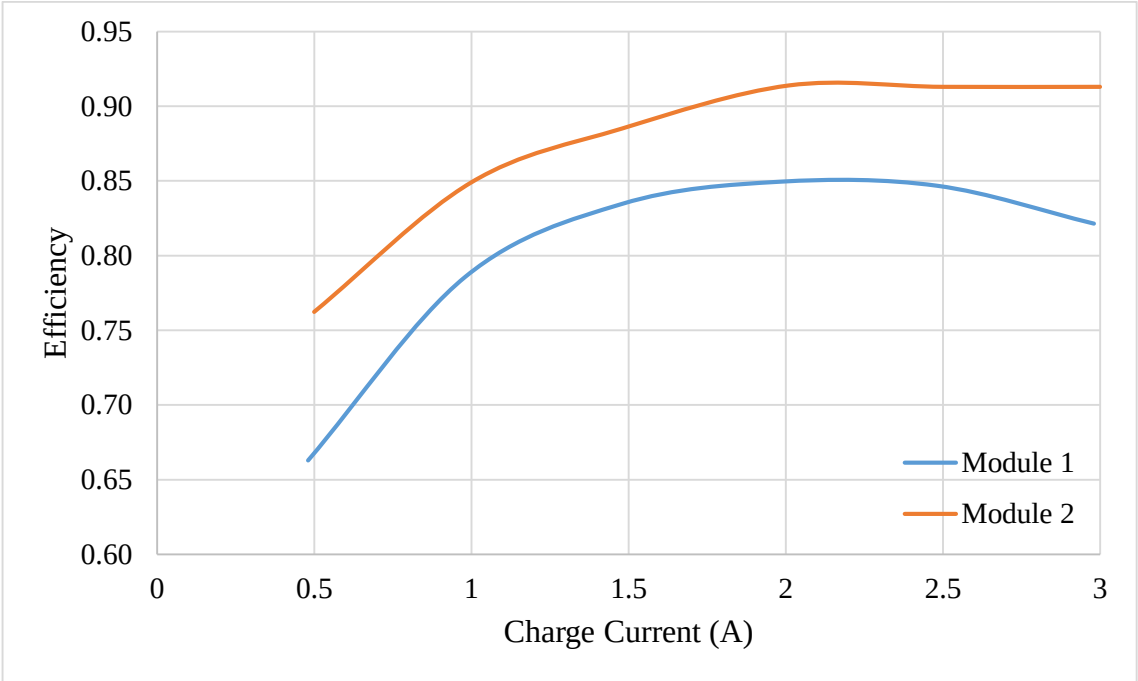

Figure 5.18. Charge current vs efficiency curves of the modules in G2V mode

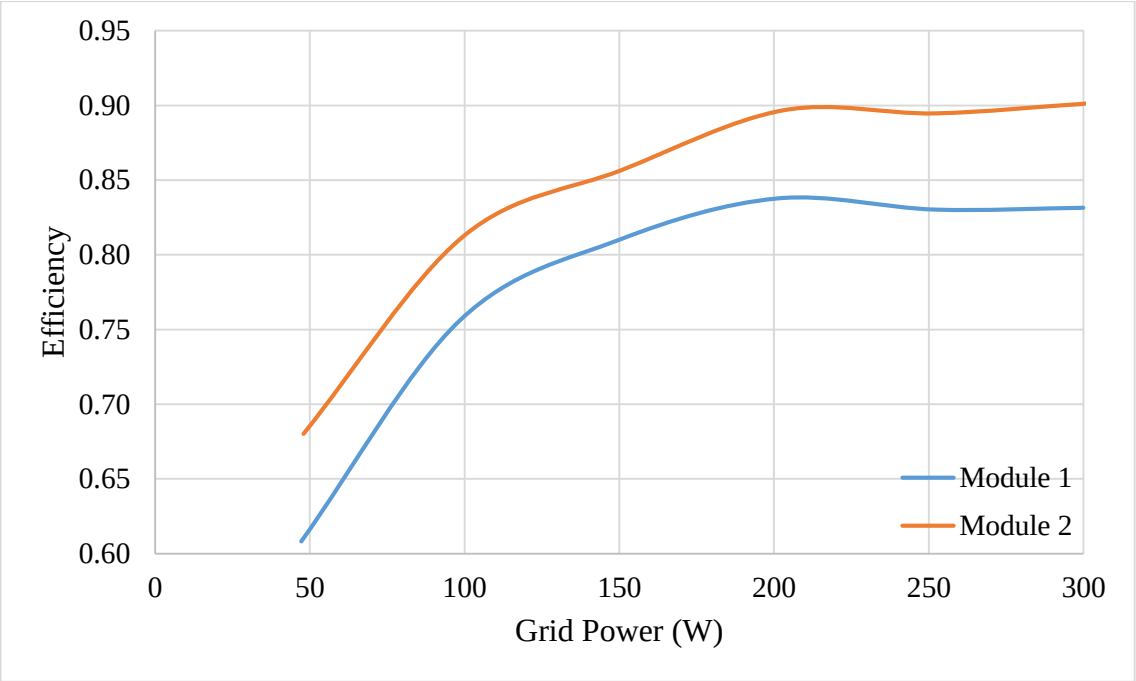

Figure 5.19. Grid power vs efficiency curves of the modules in V2G mode

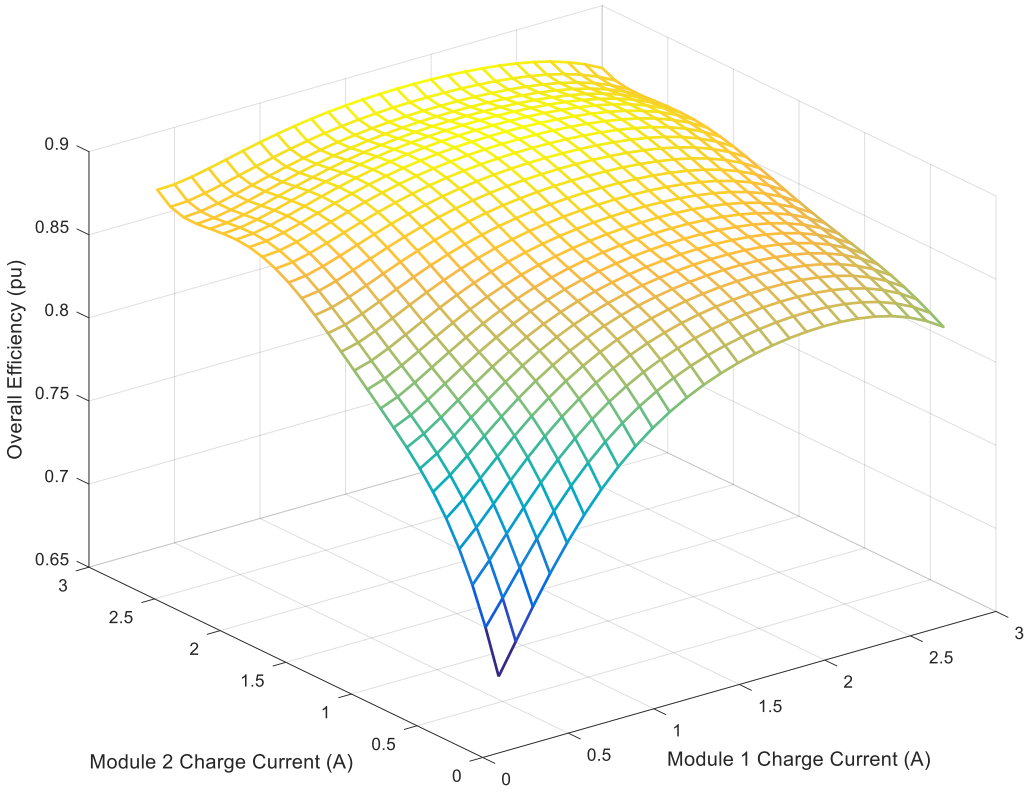

Figure 5.20. Surface function of the modular hardware system in G2V mode

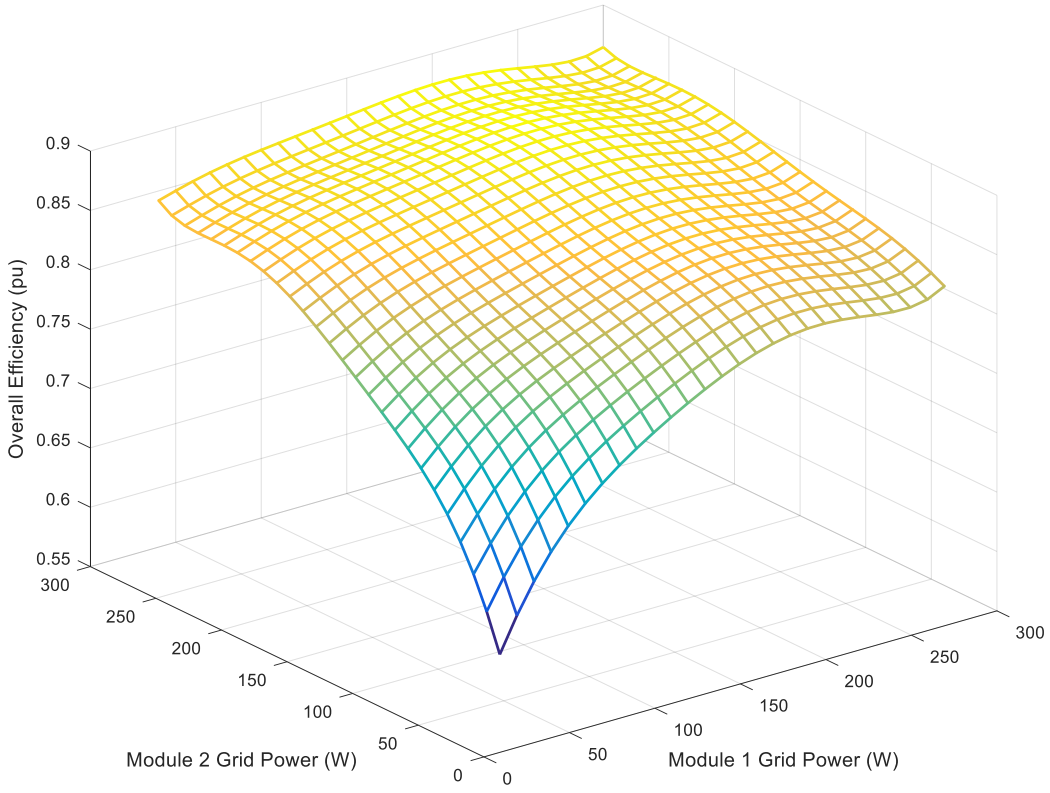

Figure 5.21. Surface function of the modular hardware system in V2G mode

Experiment scenarios for the verification of the proposed idea is depicted in Table 5.9. The demands are changed at the specified times. In equal sharing mode, the modules are operated at the same individual references to provide the total charge current or grid power given at that time. In optimized sharing mode, individual references of the modules are determined by the optimization algorithm based on the available load/efficiency curves shared before. This way two curves are obtained for both G2V and V2G modes. It is expected that the benefits and drawbacks of the optimization algorithm can be seen by comparing the efficiency curves.

Table 5.9. Experiment scenarios

Time (s)	Charge Current Demand (A)		Grid Power Demand (W)	
	Equal Sharing	Optimized Sharing	Equal Sharing	Optimized Sharing
10	1	1	100	100
20	2	2	200	200
30	3	3	300	300
40	4	4	400	400
50	5	5	500	500
60	6	6	600	600

The experiments are conducted according to Table 5.9. Obtained efficiency curves for G2V mode is depicted in Figure 5.22. This figure resembles to that obtained from the computer simulations. Efficiency improvement from no load to approximately 66% load is apparent from the figure. After that the modules almost share the power equally to provide the necessary power and the two efficiency curves almost overlap. At light loads the efficiency improvement up to 13% is noted.

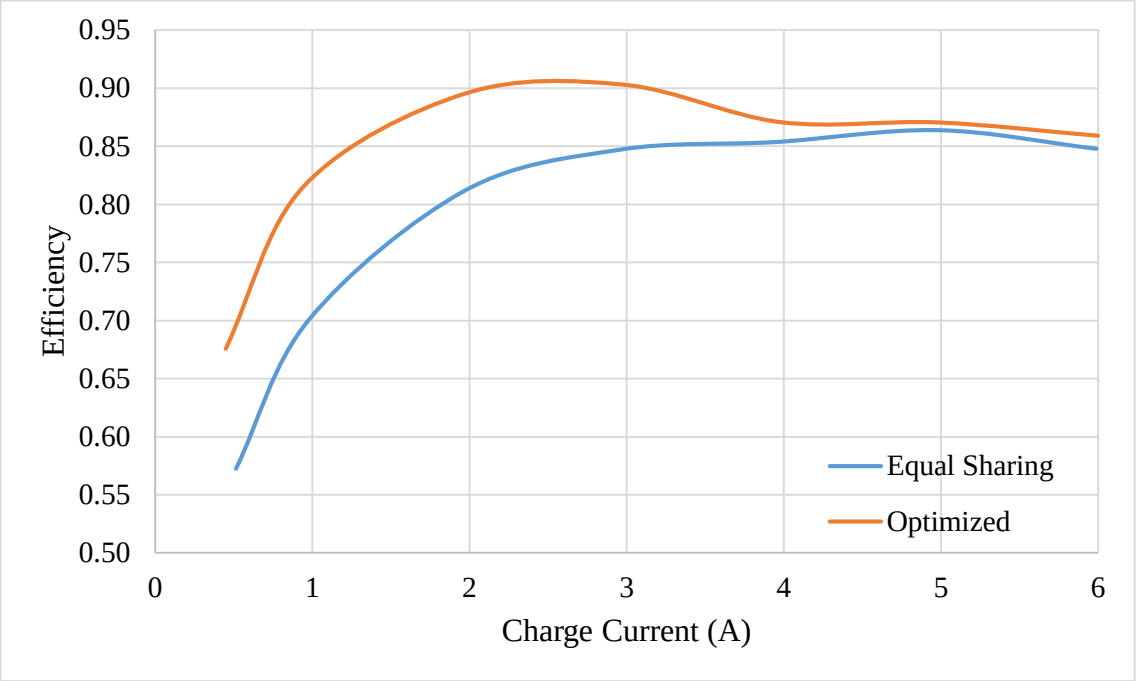

Figure 5.22. Comparison of equal sharing and optimized sharing in G2V mode

The same experiment is conducted for V2G mode as well and the resulting efficiency curves are given in Figure 5.23. Again in this mode, the efficiency improvement of up to 10% is visible until 66% of full power.

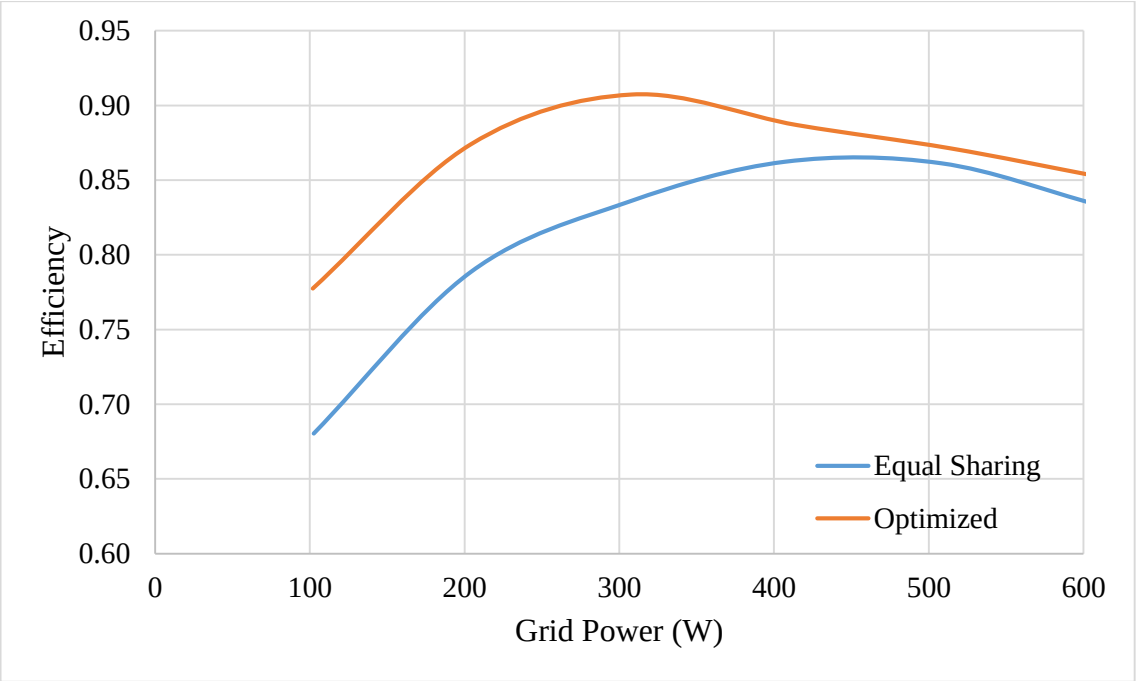

Figure 5.23.Comparison of equal sharing and optimized sharing in V2G mode

6. CONCLUSION and DISCUSSION

The motivation for this study is to increase the efficiency of the charger structure for EVs. This study proposed a new modular, bidirectional smart charger design for EV and PHEV applications that uses an optimization algorithm to increase the efficiency of the overall system throughout the load range. Most power electronic system exhibits lower efficiency from light to middle load conditions. In this study, an optimization control algorithm was designed and implemented, that once the load/efficiency data of the modules are obtained, optimization algorithm works to determine the operating points of the individual charger modules to keep the overall efficiency of the charger system high at all charging powers. As given previously through the detailed analyses, any small improvement in charging efficiency might well have a huge impact on the long term when the rising popularity of the EVs are concerned. Another prominent feature of the charger is that it is capable of bidirectional operation which makes the charger V2G-ready and it is possible to supply grid when the grid demand is high.V2G technology opens up new possibilities when the widespread adoption of EVs are concerned.

This study was formed as follows. First, a broad background information on the history of EVs was given. The battery technologies utilized in EVs were detailed. It was followed with SoC determination methods, battery management technologies and the impact of EVs on the grid infrastructure. The chapter was finalized with the motivation that lead to the proposal of the study and the possible benefits of the designed system. Then, a literature survey on the power electronic systems that are utilized in the battery chargers of EVs was given. This chapter also focused on the existing implementations of modular applications. It was followed by the system design and the statement of the generalized optimization problem that was solved in order to verify the validity of the proposed idea. Then, the topology to be utilized in the study was presented and the detailed analyses of the topology were shared. Following chapter elaborated the computer simulation results from ground up. First, the selected topology was simulated and its operation was verified. Then, the modular system was designed in the computer simulation medium, and the optimization algorithm was constructed and its operation was verified. Last, designed hardware system was shared. The necessary calculations for designing the passive elements, the workings of the digital controller and the closed loop control diagram were detailed. The experimental work in single module operation remarked the performance of the charger modules. Modular operation experiments comparing the equal sharing and the proposed optimized sharing were

conducted, and the results provided us with clear results that verified the validity of the idea presented in this study.

Power electronic converters are widely studied in the literature. Generally, two-stage approach is employed in the design of the AC/DC converters [43]. Both unidirectional and bidirectional PFC converters, which are the first stage of the AC/DC converters are discussed and compared in detail [45]-[49]. DC/DC converters, which provides well regulated DC charging power are presented in [50]-[55]. DC/DC converters also have unidirectional and bidirectional types. A relatively newer design approach is the single-stage power conversion topologies, and as the name suggests it converts AC power to DC power in one stage. These converters are covered in [27], [56], [57]. In literature and industry, modular approach finds its use in many electrical applications where their advantages overwhelm their disadvantages. Its advantages can be listed as flexibility, ease of maintenance and increased reparability. Possible disadvantages of modular systems may include the increased cost of production, lower power and/or energy density and increased cost of maintenance. Generally, the production cost of a single higher power rated module is lower than multiple modules to achieve the same power. Regardless, they are used in power supplies [58], power factor correction applications [59] and especially grid connected photovoltaic (PV) systems [60]-[62].

The proposed modular system design in this study brings efficiency improvement throughout the load range method for a battery charger to be utilized in an electric vehicle. This was verified through computer simulations first. At the beginning, the simulation studies were conducted to observe the inner working and to gain insight about the intricacies of the single-stage power conversion topology. Proposed improvements for the general operation of the topology was verified. Then, modular system idea was verified with two modules in the simulation medium. The optimization algorithm was constructed based on the analyses and literature research. The simulation studies with just two modules showed a clear increase in the light to moderate load efficiency of the overall system when compared to a system that does not make use of an optimization algorithm. This opened up the way to verify the idea through real world hardware implementation. Next, the modular design was realized using two hardware prototype modules. The modules were operated in parallel and two load/efficiency plots for G2V and V2G modes which depict equal sharing and optimized sharing cases were obtained. The resulting load/efficiency curves of the equal sharing and

optimized sharing cases were compared and efficiency increases in light to middle loads are vividly depicted for both G2V and V2G modes.

As stated previously, the modular designs reported in [58]-[62], generally employ this method in order to increase the power level of the system. Only the works reported in [59] and [60] proposes efficiency increase in light load by adjusting the number of operating modules according to power demand. However, none of the modular designs presented in the literature makes use of an optimization algorithm to provide efficiency increase to improve system performance. Also, the single-stage power electronic converter topology reported in [27], which forms the basis of the topology used in this work, achieves 89.96% peak efficiency, whereas Module 2 of the charger system achieves 91.03% peak efficiency albeit at a different power level.

Findings of this work signify the importance of the proposed flexible modular design strategy and the advantages it brings. The efficiency increase for the light loads and the possibility to increase the power level of the chargers while keeping the overall efficiency of the system are tempting for this design to be used in the next generation of electric vehicles. This study would have a much more profound impact for Turkey if the world averages on electric vehicle use could have been met in Turkey. However, it is important in the sense that it might initiate the discussion on electrification of vehicles and accelerate the transition from internal combustion to pure, or at least hybrid electric drivetrains. Companies in power electronics sector that would like to design and produce EV battery chargers might benefit from the work conducted in this study to gain insight about the chargers and recent trends in the EV industry.

This study has the following contributions to the academic literature. First, the modular design idea that is being used in several fields was improved significantly by using the efficiency data to increase overall efficiency of a system via optimization method. Second, this idea was applied to a battery charger that can be utilized in an electric vehicle, to propose a method to increase energy savings in charging operation whose benefits are shown for the next 10 years. Moreover, modular system design with optimization idea has the capability to be extended to other power electronic applications. Third, designed battery charger has bidirectional power transfer capability, and it was shown that the optimization method works for both G2V and V2G modes. V2G technologies are expected to be more common in the next 10 years to gain more benefit from the electric vehicles which can act as distributed energy sources for the grid. Fourth, the single-stage topology utilized in the study was

improved by making several adjustments in the topology and it was shown that the adjustments bring improvements in the operation of the circuit.

Future work on this study can be conducted to increase the number of modules and to extend the domain of the optimization algorithm to bring more flexibility in the system design. Increasing the number of modules will exponentially increase the complexity of the optimization algorithm used in the study. Also the power and voltage levels may be increased to better adapt to existing charger technologies.

A preliminary simulation work of the operation of three charger modules in optimized sharing configuration and also in three-phase configuration with balanced sharing was conducted. The results are given in Appendix - 1 and they provide evidence for the feasibility of the proposed idea with three modules and the flexibility of the modular configuration.

REFERENCES

[1] C. Mi, M. A. Masrur, and D. W. Gao, "Introduction," *Hybrid Electric Vehicles: Principles and Applications with Practical Perspectives*, 1st Ed., Sussex, UK: John Wiley & Sons, **2011**, ch. 1, sec. 2, pp. 8-9.

[2] T. Markel, "Plug-in electric vehicle infrastructure: A foundation for electrified transportation," presented at the *MIT Energy Initiative Transp. Electrification Symposium.*, Cambridge, MA, 2010 [Online]. Available: http://www.nrel.gov/docs/fy10osti/47951.pdf, National Renewable Energy Laboratory Conf. Paper 540-47951.

[3] M. Ehsani, Y. Gao, and A. Emadi, "Environmental impact and history of modern transportation," *Modern Electric, Hybrid Electric, and Fuel Cell Vehicles: Fundamentals, Theory, and Design*, 2nd Ed., Boca Raton, FL: CRC Press, **2010**, ch. 1, sec. 6, pp. 12-13.

[4] X. Han, M. Ouyang, L. Lu, and J. Li, "Cycle life of commercial lithium-ion batteries with lithium titanium oxide anodes in electric vehicles," *Energies*, vol. 7, no. 8, pp. 4895-4909, Aug. **2014.**

[5] Anonymous, Lithium-ion battery life [Online], Available: http://www.saftbatteries.com/system/files_force/li_ion_battery_life__TechnicalSheet_en_0514_Protected.pdf (May, **2017**)

[6] Anonymous, Battery Life (and Death) [Online], Available: http://www.mpoweruk.com/life.htm (May, **2017**)

[7] S. Saxena, C.L. Floch, J. MacDonald, and S. Moura, "Quantifying EV battery end-of-life through analysis of travel needs with vehicle powertrain models," *Journal of Power Sources*, vol. 282, pp. 265-276, May **2015**.

[8] C. Liu, K.T. Chau, D. Wu, and S. Gao, "Opportunities and challenges of vehicle-to-home, vehicle-to-vehicle, and vehicle-to-grid technologies," *Proceedings of the IEEE*, vol. 101, no. 11, pp. 2409-2427, Nov. **2013**.

[9] M. C. Kisacikoglu, *Vehicle-to-grid (V2G) reactive power operation analysis of the EV/PHEV bidirectional battery charger*, Ph.D. dissertation, Department of Electrical Engineering, The University of Tennessee, Knoxville, TN, **2013**.

[10] P. Miller, "Automotive Li-ion batteries," *Johnson Matthey Technology. Rev.*, vol. 59, no. 1, pp. 4–13, Jan. **2015**.

[11] W.-Y. Chang, "The state of charge estimating methods for battery: A review," *ISRN Applied Mathematics*, vol. 2013, Article ID 953792, 7 pages, **2013**.

[12] V. Pop, H. J. Bergveld, P. H. L. Notten, J. H. G. Op het Veld, and P. P. L. Regtien, "Accuracy analysis of the state-of-charge and remaining run-time determination for lithium-ion batteries," *Measurement*, vol. 42, no. 8, pp. 1131–1138, **2009**.

[13] L.-R. Chen, S.-L. Wu, D.-T. Shieh, and T.-R. Chen, "Sinusoidal-ripple-current charging strategy and optimal charging frequency study for Li-ion batteries," *IEEE Transactions on Industrial Electronics*, vol. 60, no. 1, pp. 88–97, Jan. **2013**.

[14] Y. Lee and S. Park, "Electrochemical state based sinusoidal ripple current charging control," *IEEE Transactions on Power Electronics*, vol. 30, no. 8, pp. 4232 4243, Aug. **2015**.

[15] F. Lacressonniere, B. Cassoret and J. -F. Brudny, “Influence of a charging current with a sinusoidal perturbation on the performance of a lead-acid battery,” *IEE Proceedings - Electric Power Applications*, vol. 152, no. 5, pp. 1365-1370, Sep. **2005**.

[16] S. D. Breucker, *Impact of DC-DC converters on Li-ion batteries*, Ph.D. dissertation, Department of Electrical Enginering, Katholieke Universiteit Leuven, Leuven, Belgium, **2012**.

[17] Anonymous, BU-409: Charging Lithium-ion [Online]. Available: http://batteryuniversity.com/learn/article/charging_lithium_ion_batteries (March, **2015**).

[18] Anonymous, BU-410: Charging at High and Low Temperatures [Online]. Available: http://batteryuniversity.com/learn/article/charging_at_high_and_low_ temperatures (March, **2015**).

[19] B. P. Divakar, K. W. E. Cheng, H. J. Wu, J. Xu, H. B. Ma, W. Ting, K. Ding, W. F. Choi, B. F. Huang, and C. H. Leung, “Battery management system and control strategy for hybrid and electric vehicle,” in *3rd International Conference on Power Electronics Systems and Applications, 2009. PESA 2009*, 2009, pp. 1–6.

[20] Anonymous, How it works [Online]. Available: http://www.orionbms.com/general/ how-it-works (March, **2015**).

[21] M. Yilmaz and P. T. Krein, “Review of battery charger topologies, charging power levels, and infrastructure for plug-in electric and hybrid vehicles,” *IEEE Transactions on Power Electronics*, vol. 28, no. 5, pp. 2151-2169, May **2013**.

[22] *Number of households by size and type, 2014-2015* [Online]. Available: http://www.tuik.gov.tr/PreIstatistikTablo.do?istab_id=2430 (February, **2017**).

[23] *Distribution of net electricity consumption by sectors* [Online]. Available: http://www.tuik.gov.tr/PreIstatistikTablo.do?istab_id=1579 (February, **2017**).

[24] *Number of road motor vehicles by aim of use* [Online]. Available: http://www.tuik.gov.tr/PreIstatistikTablo.do?istab_id=355 (February, **2017**).

[25] *Freight and passenger transportation and the circulation on the state roads, provincial roads and motorways* [Online]. Available: http://www.tuik.gov.tr/PreIstatistikTablo.do?istab_id=354 (February, **2017**).

[26] B. Ozpineci, “Oak Ridge National Laboratory Annual Progress Report for the Power Electronics and Electric Motors Program,” Available: https://info.ornl.gov/sites/publications/Files/Pub52422.pdf (May, **2017**)

[27] N. D. Weise, G. Castelino, K. Basu, and N. Mohan, “A single-stage dual-active-bridge-based soft switched AC-DC converter with open-loop power factor correction and other advanced features,” *IEEE Transactions on Power Electronics*, vol. 29, no. 8, pp. 4007 4016, Aug. **2014**.

[28] Online: https://ytbs.teias.gov.tr/ytbs/frm_login.jsf (May, **2017**)

[29] Anonymous, Turkey to stay on summer time all year round [Online], Available: https://www.theguardian.com/world/2016/sep/08/turkey-to-stay-on-summer-time-all-year-round (May, **2017**)

[30] O. Sundström and C. Binding, "Flexible charging optimization for electric vehicles considering distribution grid constraints," *IEEE Transactions on Smart Grid*, vol. 3, no. 1, pp. 26–37, Mar. **2012**.

[31] P. S. Moses, M. A. S. Masoum, and S. Hajforoosh, "Overloading of distribution transformers in smart grid due to uncoordinated charging of plug-in electric vehicles," in *Proc. Rec. IEEE Power Energy Systems Innovative Smart Grid Technologies Conference*, Jan. **2012**.

[32] D. P. Tuttle and R. Baldick, "The evolution of plug-in electric vehicle-grid interactions," *IEEE Transactions on Smart Grid*, vol. 3, no. 1, pp. 500-505, Mar. **2012**.

[33] Z. Wang and S. Wang, "Grid power peak shaving and valley filling using vehicle-to-grid systems," *IEEE Transactions on Power Delivery*, vol. 28, no. 3, pp. 1822-1829, Jul. **2013**.

[34] M. Yilmaz and P. T. Krein, "Review of the impact of vehicle-to-grid technologies on distribution systems and utility interfaces," *IEEE Transactions on Power Electronics*, vol. 28, no. 12, pp. 5673-5689, Dec. **2013**.

[35] M. Brenna, F. Foiadelli, and M. Longo, "The exploitation of vehicle-to-grid function for power quality improvement in a smart grid," *IEEE Transactions on Intelligent Transportation Systems*, vol. 15, no. 5, pp. 2169-2177, Oct. **2014**.

[36] J. Lassila, J. Haakana, V. Tikka, and J. Partanen, "Methodology to analyze the economic effects of electric cars as energy storages," *IEEE Transactions on Smart Grid*, vol. 3, no.1, pp. 506-516, Mar. **2012**.

[37] U. C. Chukwu and S. M. Mahajan, "Real-time management of power systems with V2G facility for smart-grid applications," *IEEE Transactions on Sustainable Energy*, vol. 5, no. 2, pp. 558-566, Apr. **2014**.

[38] A. Schuller, B. Dietz, C. M. Flath, and C. Weinhardt, "Charging strategies for battery electric vehicles: economic benchmark and V2G potential," *IEEE Transactions on Power Systems*, vol. 29, no. 5, pp. 2014-2022, Sep. **2014**.

[39] M. Falahi, H. Chou, M. Ehsani, L. Xie, and K. L. Butler-Purry, "Potential power quality benefits of electric vehicles," *IEEE Transactions on Sustainable Energy*, vol. 4, no. 4, pp. 1016-1023, Oct. **2013**.

[40] Anonymous, Yıllar İtibariyle Elektrikli Araç Satışı, [Online], Available: http://www.enerjiatlasi.com/haber/turkiye-deki-elektrikli-otomobil-sayisi (February, **2017**).

[41] Number of road motor vehicles registered to the traffic during the year by Classification of Statistical Region Units Level 1 [Online]. Available: http://www.tuik.gov.tr/PreIstatistikTablo.do?istab_id=359 (March, **2017**).

[42] *Distribution of net electricity consumption by sectors* [Online]. Available: http://www.tuik.gov.tr/PreIstatistikTablo.do?istab_id=1579 (March, **2017**).

[43] A. Khaligh and S. Dusmez, "Comprehensive topological analysis of conductive and inductive charging solutions for plug-in electric vehicles," *IEEE Transactions on Vehicular Technology*, vol. 61, no. 8, pp. 3475-3489, Oct. **2012**.

[44] S. S. Williamson, A. K. Rathore, and F. Musavi, "Industrial electronics for electric transportation: current state-of-the-art and future challenges," *IEEE Transactions on Industrial Electronics*, vol. 62, no. 5, pp. 3021-3032, May **2015**.

[45] F. Musavi, M. Edington, W. Eberle, and W. G. Dunford, "Evaluation and efficiency comparison of front end AC-DC plug-in hybrid charger topologies," *IEEE Transactions on Smart Grid*, vol. 3, no. 1, pp. 413-421, Mar. **2012**.

[46] Y.-S. Kim, W.-Y. Sung, and B.-K. Lee, "Comparative performance analysis of high density and efficiency PFC topologies," *IEEE Transactions on Power Electronics*, vol. 29, no. 6, pp. 2666-2679, Jun. **2014**.

[47] T. Israeli, I. Levin, D. Shmilovitz, and S. Singer, "AC-DC converters with bi-directional power flow and some possible applications," in *Proceedings of IEEE International Symposium on Circuits Systems*, May **2006**.

[48] M. Jordan, "Design and testing of a bidirectional smart charger prototype," M.S. thesis, Dept. Elect. and Comp. Eng., Univ. Waterloo, Waterloo, Canada, **2015**.

[49] D. C. Erb, O. C. Onar, and A. Khaligh, "Bi-directional charging topologies for plug-in hybrid electric vehicles," in *Proceedings IEEE Applied Power Electronics Conference Expo*, Feb. **2010**, pp. 2066–2072.

[50] D. S. Gautam, F. Musavi, M. Edington, W. Eberle, and W. G. Dunford, "An automotive onboard 3.3-kW battery charger for PHEV application," *IEEE Transactions on Vehicular Technology*, vol. 61, no. 8, pp. 3466-3474, Oct. **2012**.

[51] B. Whitaker, A. Barkley, Z. Cole, B. Passmore, D. Martin, T. R. McNutt, A. B. Lostetter, J. S. Lee, and K. Shiozaki, "A high-density, high-efficiency, isolated on-board vehicle battery charger utilizing silicon carbide power devices," *IEEE Transactions on Power Electronics*, vol. 29, no. 5, pp. 2606-2617, May **2014**.

[52] J. Deng, S. Li, C. C. Mi, and R. Ma, "Design methodology of LLC resonant converters for electric vehicle battery chargers," *IEEE Transactions on Vehicular Technology*, vol. 63, no. 4, pp. 1581 1592, May **2014**.

[53] J. Y. Lee and H. J. Chae, "6.6-kW onboard charger design using DCM PFC converter with harmonic modulation technique and two-stage DC/DC converter," *IEEE Transactions on Industrial Electronics*, vol. 61, no. 3, pp. 1243 1252, Mar. **2014**.

[54] T. Jiang, J. Zhang, X. Wu, K. Sheng, and Y. Wang, "A bidirectional LLC resonant converter with automatic forward and backward mode transition," *IEEE Transactions on Power Electronics*, vol. 30, no. 2, pp. 757-770, Feb. **2015**.

[55] H.-S. Kim, M. –H. Ryu, J.-W. Baek, and J.-H. Jung, "High-efficiency isolated bidirectional AC-DC converter for a DC distribution system," *IEEE Transactions on Power Electronics*, vol. 28, no. 4, pp. 1642-1654, Apr. **2015**.

[56] S. Li, J. Deng, and C. C. Mi, "Single-stage resonant battery charger with inherent power factor correction for electric vehicles," *IEEE Transactions on Vehicular Technology*, vol. 62, no. 9, pp. 4336-4344, Sep. **2013**.

[57] J. Everts, F. Krismer, J. V. D. Keybus, J. Driesen, S. Member, and J. W. Kolar, "Optimal ZVS modulation of single-phase single-stage bidirectional DAB AC-DC converters," *IEEE Transactions on Power Electronics*, vol. 29, no. 8, pp. 3954 3970, Aug. **2014**.

[58] T. Thandapani and R. Arumugan, “Modular power supply for telecom application (54V/100A),” in *IEEE ISIE 2006*, Montréal, Jul. 9-12 **2006**, pp. 1334-1340.

[59] C. Wang, M. Xu, F. C. Lee, and Z. Luo, “Light load efficiency improvement for multi-channel PFC,” in *Proceedings of IEEE Power Electronics Specialist Conference (PESC)*, **2008**, pp. 4080–4085.

[60] L. Zhang, K. Sun, Y. Xing, L. Feng, and H. Ge, “A modular grid-connected photovoltaic generation system based on DC bus,” *IEEE Trans Power Electronics*, vol. 26, no. 2, pp. 523-531, Feb. **2011**.

[61] J. Mei, B. Xiao, K. Shen, L. M. Tolbert, and J. Y. Zheng, “Modular multilevel inverter with new modulation method and its application to photovoltaic grid-connected generator,” *IEEE Transactions on Power Electronics*, vol. 28, no. 11, pp. 5063-5073, Nov. **2013**.

[62] B. Xiao, L. Hang, J. Mei, C. Riley, L. M. Tolbert, and B. Ozpineci, “Modular cascaded H-bridge multilevel PV inverter with distributed MPPT for grid-connected applications,” *IEEE Transactions of Industrial Applications*, vol. 51, no. 2, pp. 1722-1731, Mar./Apr. **2015**.

[63] “IEEE Standard for Interconnecting Distributed Resources with Electric Power Systems,” *IEEE Std 1547-2003*, pp. 1–28, Jul. **2003**.

[64] Anonymous, Global Plug-in Sales for 2016, [Online] Available: http://www.ev-volumes.com/country/total-world-plug-in-vehicle-volumes/ (March, **2017**).

[65] Anonymous, PSO Tutorial, [Online] Available: http://www.swarmintelligence.org/tutorials.php (June, **2017**).

[66] D. Karaboga, “Artificial bee colony algorithm,” *Scholarpedia*, 5(3):6915, **2010**.

APPENDICES

APPENDIX - 1: FUTURE WORK

Due to time and financial restrictions the proposed idea can only be verified with two hardware modules. However, increasing the number of modules while keeping the benefits of the system should be feasible for further scalability. Also system flexibility is increased if the number of modules is increased. For example, three modules can be utilized in a three-phase charging system where the power drawn from the utility is balanced. That is why a preliminary work to verify the operation of the optimization algorithm in a system with three modules and balanced operation of three modules in a three-phase system is conducted in computer simulation medium.

Modular System Simulation

Modular system simulation is verified with three individual modules where one of them is in master configuration and the other two are slaves.

Simulation Setup and Optimization Algorithm

Simulation system setup is built as depicted in Figure 6.1. Switches S1 and S2 can be used to switch between single-phase and three-phase operating modes. Simulations should depict the benefits of the optimization method is feasible with three modules as well. The simulations dataset is to three modules by adding another load/efficiency curve for a third module. The load/efficiency curves of the three modules are depicted in Figure 6.2 and Figure 6.3.

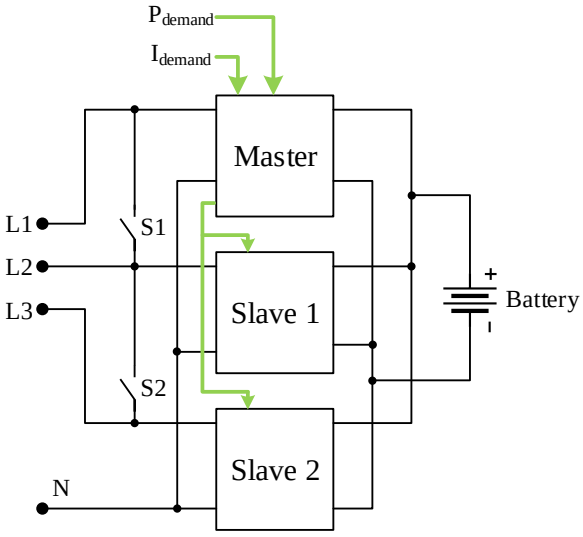

Figure 6.1. Modular system simulation setup

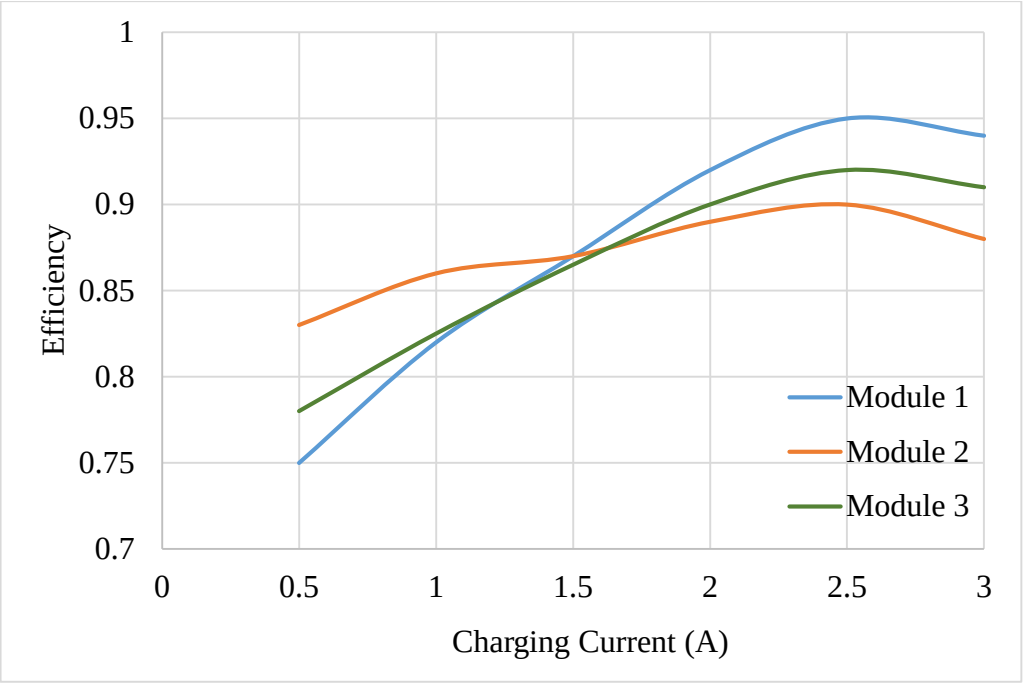

Figure 6.2. Charging current vs efficiency curves of simulation models

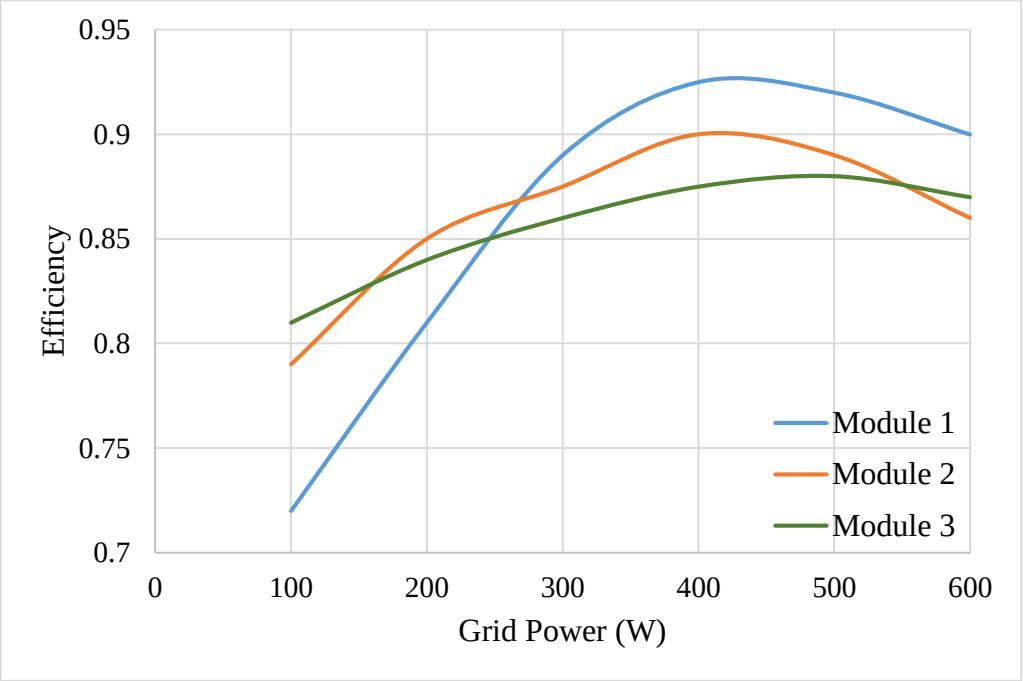

Figure 6.3. Grid power vs efficiency curves of simulation models

These curves are fitted to polynomials using MATLAB. Line search method for optimization is extended to solve an optimization problem in three dimension. To visualize the algorithm, a flowchart is built and it is given in Figure 6.4.

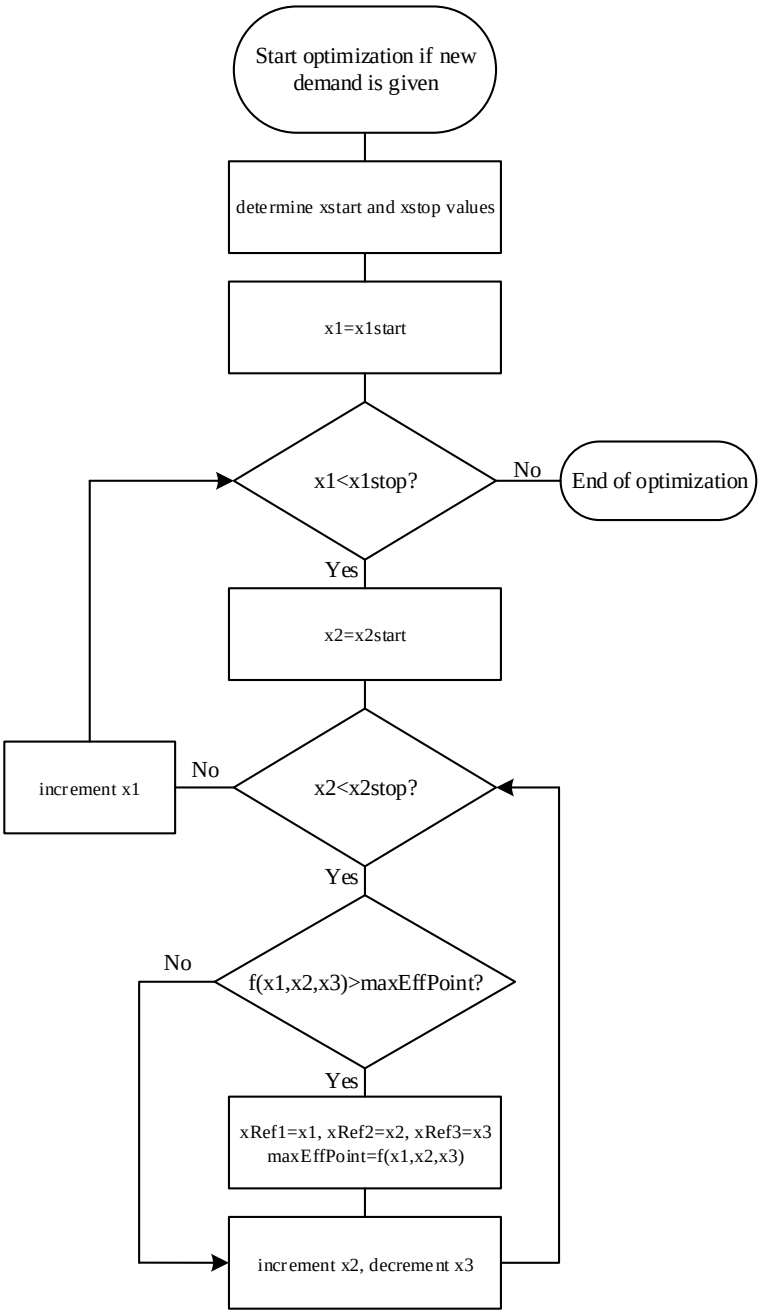

Figure 6.4. Flowchart of optimization algorithm

Optimized Sharing Simulation Results

Simulation results are gathered for both V2G and G2V operating modes at first for equal current sharing and then for optimized current sharing. Circuit elements of the simulation model are built nearly ideal and thus it is hard to determine the exact overall efficiency from the simulation. That is why the overall efficiency of the system is derived from the surface function of the overall efficiency for each discrete reference grid power of charge current.

There are four simulation scenarios in total; equal current sharing in V2G mode and G2V mode, and optimized current sharing in V2G mode and G2V mode. Reference values with corresponding time steps are given in Table 6.1.

Table 6.1. Modular system simulation references

Time Step (s)	Charge Current Demand (A)	Grid Power Demand (W)
0.5	1	200
1	2	400
1.5	3	600
2	4	800
2.5	5	1000
3	6	1200
3.5	7	1400
4	8	1600
4.5	9	1800

In equal current sharing mode, the modules will be operated at the same power for all demands. In optimized current sharing mode, when the demands are changed at given times, the master controller will run optimization algorithm and determine the new charge current or grid power command values for each individual module. Figure 6.5 shows the charge current commands for each module when the system is operated in G2V optimized current sharing mode. The dynamic current sharing for each module while keeping the total current equal to the demanded charge current can be easily seen from the graph.

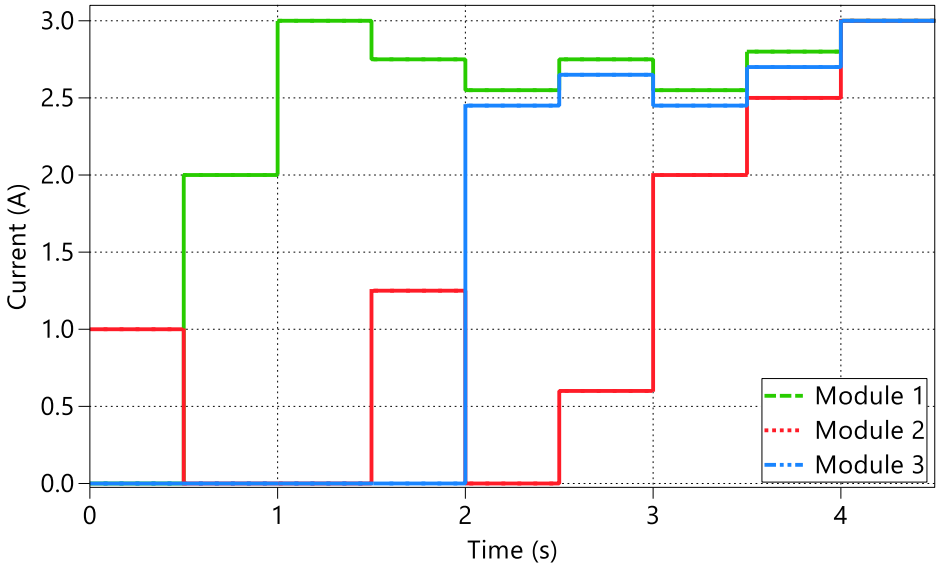

Figure 6.5. G2V mode optimized current sharing

The overall system efficiency for each demanded current is calculated from overall efficiency surface function by inserting the operating currents of the individual modules for each time section. Comparison of equal sharing and optimized sharing modes is depicted in Figure 6.6. Efficiency increase from light loads to middle loads is again apparent from the figure and consistent with the results obtained for two modules.

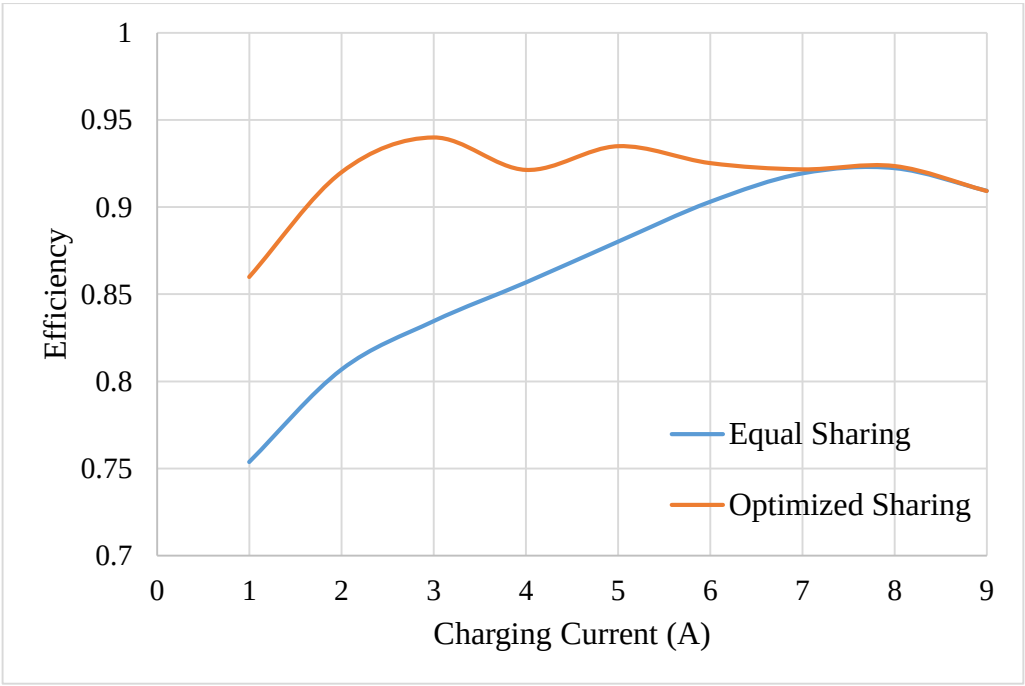

Figure 6.6. Efficiency comparison of equal and optimized current sharing methods in G2V mode

The same approach is also applied for V2G mode. The master controller gets grid power demand as given in Table 6.1 and the resulting power sharing is depicted in Figure 6.7.

Comparison of equal sharing and optimized sharing is given in Figure 6.8. Again the benefits of the proposed system can easily be seen at light to middle loads.

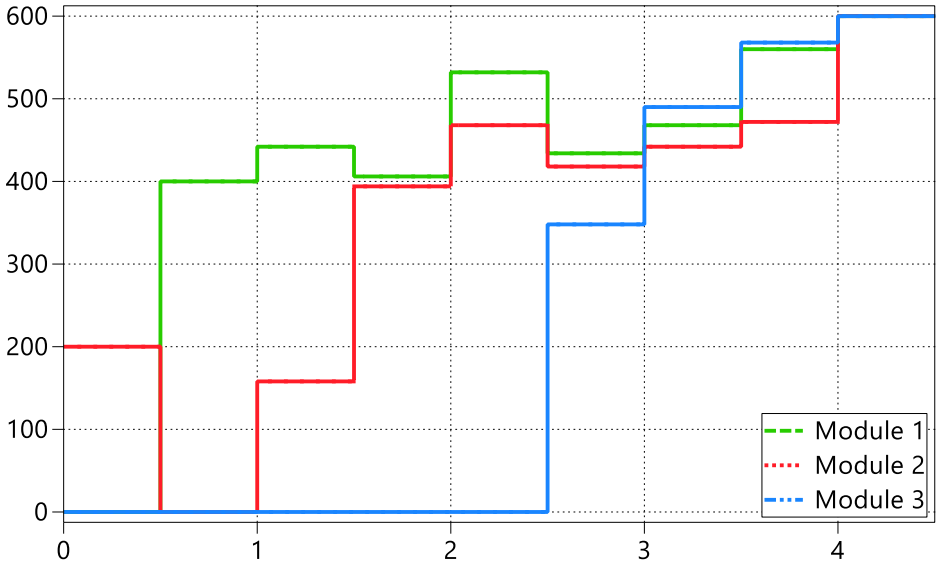

Figure 6.7. V2G mode optimized current sharing

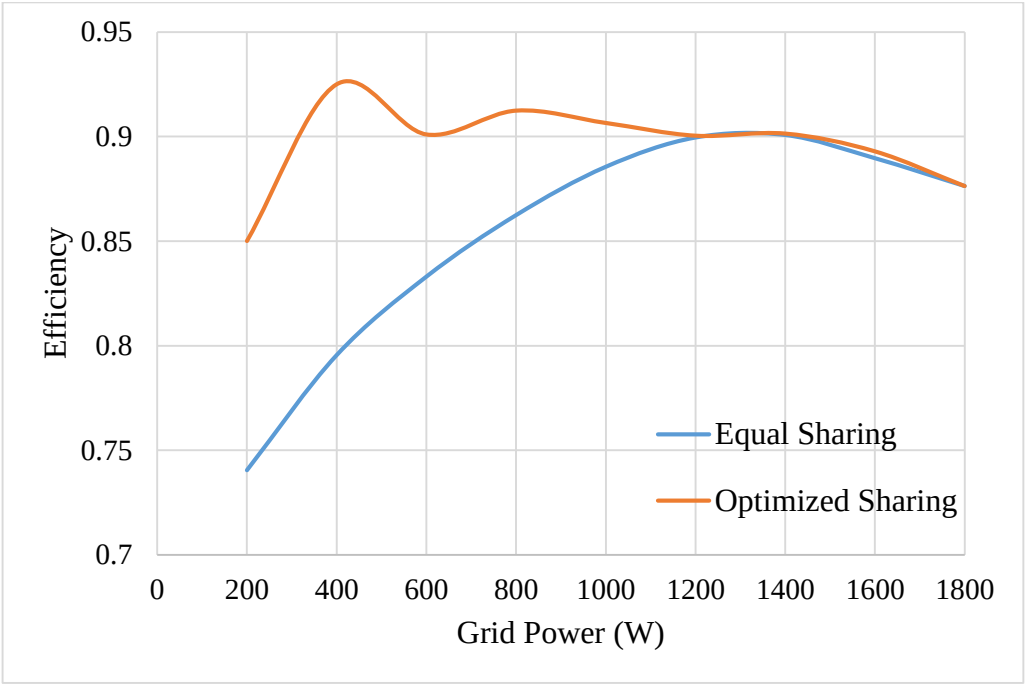

Figure 6.8. Efficiency comparison of equal and optimized current sharing methods in V2G mode

Three-phase Simulation Results

Balanced operation for three-phase configuration is also verified in simulations. When the chargers are operated in three-phase at balanced power the sinusoidal ripple from each charger is almost canceled out at the battery DC bus and batteries are charged with almost

ripple-free current. The same principle also applies for V2G mode and when in V2G mode, the grid is supplied with almost constant power.

The simulation results for G2V mode when the modular system is in three-phase is given in Figure 6.9. The ripple is reduced to at least 5.5% of its previous value at the light loads. At higher loads the reduction in ripple is much more significant. Grid power waveform when the modules are operated in three-phase in V2G mode can also be seen in Figure 6.10.

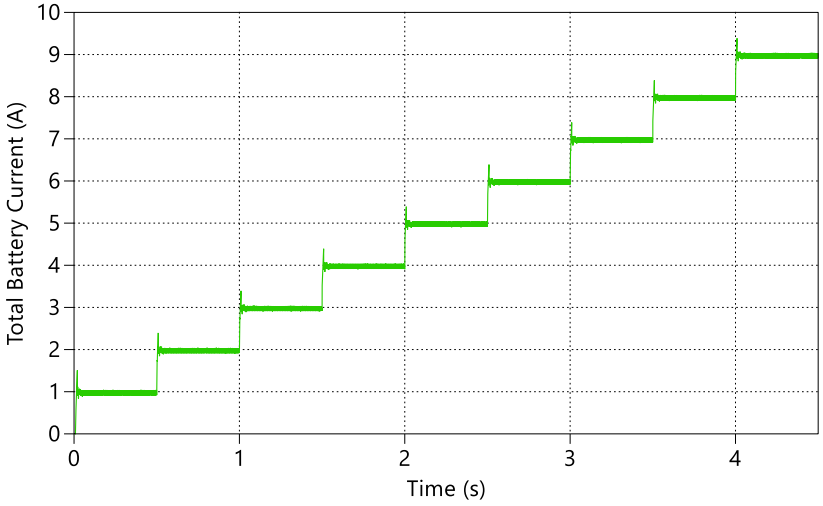

Figure 6.9. Three-phase equal current sharing G2V mode results

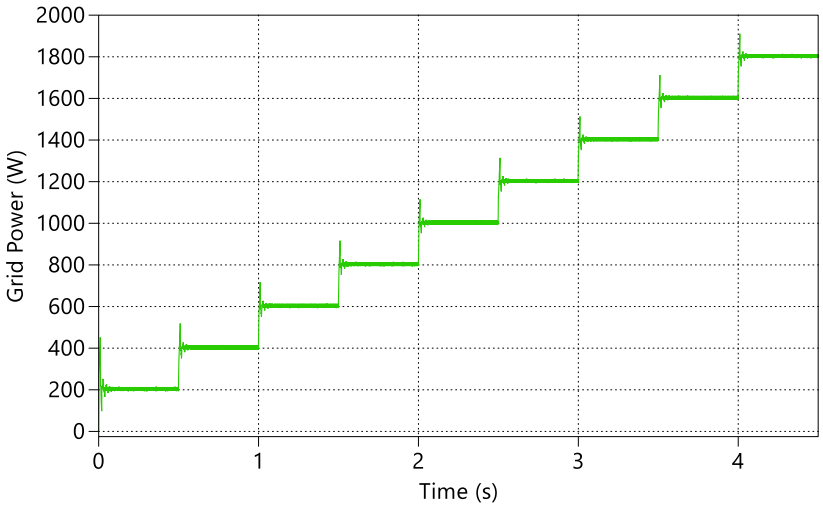

Figure 6.10. Grid power waveform when system is in three-phase V2G mode

CURRICULUM VITAE

Credentials

Name Surname	: Faik Elvan
Place of Birth	: Keçiören
Marital Status	: Married
E-mail	: faik.elvn@gmail.com
Address	: Yenimahalle, Ankara

Education

MSc.	: Hacettepe University Dpt. of Electrical and Electronics Engineering, Ankara (2013-2017)
BSc.	: Middle East Technical University Dpt. of Electrical and Electronics Engineering, Ankara (2007-2013)

Foreign Languages

English	: Advanced

Work Experience

Sep. 2013 - …	: R&D Engineer, ELSİS A.Ş., Ankara
Mar. 2013 – Aug. 2013	: System Engineer, Promod R&D Software, Ankara

Areas of Expertise

Switch mode power supplies, analog and digital control of power electronic systems, battery chargers.

Projects and Budgets

Publications

Oral and Poster Presentations

HACETTEPE UNIVERSITY
GRADUATE SCHOOL OF SCIENCE AND ENGINEERING
THESIS/DISSERTATION ORIGINALITY REPORT

HACETTEPE UNIVERSITY
GRADUATE SCHOOL OF SCIENCE AND ENGINEERING
TO THE DEPARTMENT OF ELECTRICAL and ELECTRONICS ENGINEERING

Date: 11/07/2017

Thesis Title / Topic: DESIGN OF A SMART GRID COMPATIBLE, BIDIRECTIONAL MODULAR BATTERY CHARGER FOR PLUG-IN ELECTRIC VEHICLES

According to the originality report obtained by myself/my thesis advisor by using the *Turnitin* plagiarism detection software and by applying the filtering options stated below on 07/07/2017 for the total of 82 pages including the a) Title Page, b) Introduction, c) Main Chapters, d) Conclusion sections of my thesis entitled as above, the similarity index of my thesis is 5 %.

Filtering options applied:

1. Bibliography/Works Cited excluded
2. Quotes excluded / ~~included~~
3. Match size up to 5 words excluded

I declare that I have carefully read Hacettepe University Graduate School of Sciene and Engineering Guidelines for Obtaining and Using Thesis Originality Reports; that according to the maximum similarity index values specified in the Guidelines, my thesis does not include any form of plagiarism; that in any future detection of possible infringement of the regulations I accept all legal responsibility; and that all the information I have provided is correct to the best of my knowledge.

I respectfully submit this for approval.

Date and Signature
11/07/2017

Name Surname: Faik ELVAN
Student No: N13120298
Department: Electrical and Electronics Engineering
Program:
Status: ☒ Masters ☐ Ph.D. ☐ Integrated Ph.D.

ADVISOR APPROVAL

APPROVED.
Prof. Dr. Uğur BAYSAL
(Title, Name Surname, Signature)